A ^{119}Sn and ^{155}Gd Mössbauer spectroscopy and neutron diffraction study of $R_3T_4X_4$ (R=rare-earth,T=Cu,Ag, X=Sn,Ge) compounds

Christian Voyer
Department of Physics
McGill University
Montreal, Québec
CANADA

April, 2011

A thesis submitted to
McGill University
in partial fulfillment of the requirements
for the degree of Doctor of Philosophy

Abstract

The isostructural $R_3T_4X_4$ (R: rare earth, T:Mn,Pd,Cu,Ag, X:Si,Ge,Sn) family of compounds have been extensively studied recently due to the rich variety of magnetic behaviour exhibited: the two rare earth sublattices often order with quite different moment values and distinct magnetic structures. In some cases the rare earth sites will also have quite different ordering temperatures. Several of the series, $R_3Cu_4Sn_4$, $R_3Ag_4Sn_4$ and $R_3Cu_4Ge_4$, appear not to follow the expected de Gennes scaling law of transition temperatures despite the structural uniformity of the system. Moreover, the system suffers from a common problem in rare earth intermetallic systems: an important lack of data and understanding of the Sm and Gd members.

Capitalizing on the presence of Sn in many of these compounds, we have used ^{119}Sn Mössbauer spectroscopy as a probe of local magnetism at the Sn sites in the structure. Although Sn carries no magnetic moment, a transferred field from the rare earth neighbours is observed, as both Sn sites in the structure have nearest neighbours from both rare earth sublattices. We also performed ^{155}Gd Mössbauer spectroscopy on three Gd compounds, probing the local magnetism at the ^{155}Gd nuclei directly. Using the newly developed flat plate mounting for highly absorbing samples, we performed neutron diffraction on several Sm and Gd compounds to probe the long range spatial symmetry of the rare earth magnetic moments. The Mössbauer spectroscopy and neutron scattering results were then combined as verification of consistency, but more importantly as complementary sources of magnetic information allowing us to draw conclusions that otherwise could not be drawn with either of the experimental techniques alone.

We find that a simple isotropic hyperfine field transfer model successfully describes the ^{119}Sn Mössbauer spectra of several $R_3T_4Sn_4$ (T:Cu,Ag) compounds. ^{119}Sn Mössbauer spectroscopy also reveals important magnetic interactions previously missed: $Nd_3Cu_4Sn_4$ data exhibits a clear magnetic contribution at temperatures at which neutron diffraction data did not, while $Ho_3Cu_4Sn_4$ exhibited magnetic interactions above the ordering temperature determined by neutron diffraction. The $Sm_3Ag_4Sn_4$ and $Sm_3Cu_4Sn_4$ compounds proved to behave entirely differently than previously thought: the former undergoes magnetic ordering at 26 K rather than 9 K, and shows evidence of anisotropic field transfer, while $Sm_3Cu_4Sn_4$ fails to order and instead exhibits slow moment dynamics. The Gd compounds also yield surprising results as $Gd_3Cu_4Ge_4$ and $Gd_3Ag_4Sn_4$ order at far higher temperature than previously thought, while $Gd_3Cu_4Sn_4$ exhibits the most complex ^{119}Sn Mössbauer spectrum due only to the moments at the Gd-2d site.

The $R_3T_4X_4$ system remains highly magnetically complex and diverse, however the magnetic landscape has been significantly altered. The flat plate mounting technique for neutron diffraction, especially when combined with Mössbauer spectroscopy data, allows for the determination of the magnetic structures of $Sm_3Ag_4Sn_4$ as well as $Gd_3Ag_4Sn_4$ and partially of $Gd_3Cu_4Sn_4$, showing great promise as an important new experimental tool.

Résumé

La famille de composés $R_3T_4X_4$ (R: terre rare, T: Mn, Pd, Cu, Ag, X: Si, Ge, Sn) adopte uniformément la structure orthorhombique de type $Gd_3Cu_4Ge_4$ (groupe d'espace Immm, # 71). Ces composés ont été étudiés récemment en raison de la riche variété de comportements magnétiques observés: chaque sous-réseau de terre rare s'ordonne avec des valeurs de moment magnétique très différentes et adoptent des structures magnétiques distinctes. Dans certains cas, les deux sites de terres rares auront également des températures d'ordre magnétique très différentes. Plusieurs membres de la série, $R_3Cu_4Sn_4$, $R_3Ag_4Sn_4$ et $R_3Cu_4Ge_4$, ne semblent pas suivre la loi d'échelle de de Gennes des températures de transition magnétique, malgré l'uniformité structurelle du système. De plus, le système souffre d'un problème commun parmi les systèmes intermétalliques de terre rare: un manque important de mesures et compréhension des membres Sm et Gd du système.

Capitalisant sur la présence de Sn dans plusieurs de ces composés, nous avons effectué des mesures de spectroscopie Mössbauer ^{119}Sn comme une sonde locale du magnétisme aux sites Sn dans la structure. Bien que le Sn ne comporte pas de moment magnétique, un champ transféré des terres rares voisines est observé, vu que les deux sites Sn dans la structure ont des voisins proches des deux sous-réseaux de terres rares. Nous avons également effectué des mesures de spectroscopie Mössbauer ^{155}Gd sur trois composés de Gd, pour sonder le magnétisme local aux noyaux ^{155}Gd directement. En utilisant la plaque de montage nouvellement mise au point pour des échantillons hautement absorbants, nous avons procédé à la diffusion neutronique sur plusieurs composés de Sm et Gd pour sonder la symétrie spatiale à longue portée des moments magnétiques des terres rares. La spectroscopie Mössbauer et les résultats de diffusion neutronique ont ensuite été combinés premièrement pour une vérification de cohérence, mais avant tout comme des sources complémentaires d'information magnétique qui nous permettent de tirer des conclusions qui ne pourraient autrement pas être établies avec l'une ou l'autre de ces techniques à elles seule.

Nous constatons qu'un simple modèle de transfer isotropique de champ magnétique hyperfin décrit avec succès les spectres Mössbauer ^{119}Sn de plusieurs composés $R_3T_4Sn_4$ (T: Cu, Ag). La spectroscopie Mössbauer ^{119}Sn révèle aussi d'importantes interactions magnétiques inconnues auparavant: la présence d'une contribution magnétique claire de $Nd_3Cu_4Sn_4$ à des températures auxquelles la diffusion neutronique n'en detecte aucune, tandis que $Ho_3Cu_4Sn_4$ exhibe des interactions magnétiques au dessus de la température d'ordre magnétique déterminée par diffusion neutronique. Il s'avère que les composés $Sm_3Ag_4Sn_4$ et $Sm_3Cu_4Sn_4$ ont un comportement très différent de ce qui était cru auparavant: le premier subit un ordonnement magnétique à 26 K au lieu de 9 K, et montre des signes de transfert de champ magnétique hyperfin anisotrope, alors que le deuxième ne parvient pas à l'ordre magnétique mais exhibe une dynamique de moment magnétique lente. Les composés de Gd révèlent aussi des résultats surprenants alors que $Gd_3Cu_4Ge_4$ et $Gd_3Ag_4Sn_4$ ont une température d'ordonnement magnétique beaucoup plus élevée qu'on ne le pensait, et que $Gd_3Cu_4Sn_4$ exhibe les spectres Mössbauer ^{119}Sn les plus complexes du uniquement aux moments magnétiques du site Gd-2d.

Le système $R_3T_4X_4$ reste très complexe et diversifié d'un point de vue magnétique, mais le paysage magnétique a été significativement modifié. La technique de plaque de montage pour la diffusion neutronique, en particulier lorsqu'elle est combiné avec les données de spectroscopie Mössbauer, permet la détermination des structures magnétiques des composés $Sm_3Ag_4Sn_4$ et $Gd_3Ag_4Sn_4$, et partiellement du composé $Gd_3Cu_4Sn_4$, et reste prometteuse comme un nouvel outil expérimental important.

Acknowledgments

I would first and foremost like to thank my supervisor Prof. Dominic Ryan. We have been working together for many, many years now, and we have gone through many, many projects. Three successive times I have consciously chosen to work with Prof. Ryan, and I've richly benefitted each time. The patience and guidance I was awarded have been invaluable. I would also like to thank Sean Cadogan, an essential collaborator who has brought a wealth of experience and help in completing this work, and Johan Van Lierop for his help and advice with the Mössbauer dynamics code. I would like to thank the group in Genoa: M. Napoletano, P. Riani and F. Canepa, who made wonderful samples that got me started on this project. Ian Swainson at Chalk River was of great help. I am greatly saddened that I was not able to thank Lachlan Cranswick one more time before he passed. His immense skill and dedication is a great loss to the scientific community, and he will sorely be missed.

I have received excellent support from the McGill physics department faculty. I would like to specifically thank Prof. Zaven Altounian, Prof. Mark Sutton and Prof. Michael Hilke for useful discussions about solid state physics, Prof. Aashish Clerk and Prof. Charles Gale for help with Quantum Mechanics. I would also like to thank Prof. Andrew Wills at University College London for help with Irreducible Representations in neutron diffraction.

In my capacities as President of the graduate student society, I had the pleasure of working with two exceptionally skilled department chairs, Prof. Charles Gale and Prof. Martin Grant. I was privileged to receive funding via the Chalk-Rowles Fellowship, the Principal's Graduate Fellowship, and the Dow-Hickson Fellowship.

Robert Gagnon, John Smeros, Richard Talbot, and Leo Nikkinen, the exceptional team of technicians at the McGill physics department who not only help but provide insightful advice and ideas. Thank you also to my sys admin Juan Gallego. My work was made infinitely easier thanks to these gentlemen. I am also greatly indebted to the wonderful support staff in the McGill physics department: Diane, Louise, Sonia, as well as former members of the support staff Paula, and Elizabeth.

I would likewise like to thank my group mates Nally and Tatiana for helpful discussions and good times, and for patiently reading the first drafts of this work and providing important feedback. Xubo Liu who has always been forthcoming with help and advice. Though they moved on toward the beginning of this project, Laura and Alex were colleagues of an exceptional quality, and still were able to leave their mark.

There are too many wonderful people who made living in the physics department these last years an enjoyable experience. But Will, Aleks, Mehdi, David, Till, Tobin, Anne-Sophie, Josianne, Mark, Carolyn, Steve and Liz, I saw you guys the most, and that's not a bad thing :)

I would like to thank my parents for their never ending support allowing me to pursue this little dream of mine, and my sister, whom I miss dearly, for long-distance support.

Zajeło to długo czasu, i zdaję sobię sprawe że było trudno dla nas obu. A ty nigdy się nie wachałas. Jest to tylko jeden z powódow dlaczego kocham cię tak bardzo.

Contents

List of Figures

List of Tables

Chapter 1

Introduction

“Rare by name, though not by nature, 17 elements in the periodic table [...] are among the most sought-after materials in modern manufacturing” wrote The Economist (Rare earths and China - Dirty Business) on 2 October, 2010, lamenting an alleged protectionist limit of rare earth exports by China. The interest in rare earths come from their magnetic and phosphorescent properties, and they have proved not only valuable for manufacturing, but have generated much interest within the scientific community in the last half century.

The magnetism in the rare earths comes from the $4f$ electronic shell which lies deep inside the atom (having a radius of about 0.3 Å [1]), beneath the filled $5s$ and $5p$ electronic shells, partly shielding them from the crystal electric field and reducing the energy level splitting from a typical 1 eV observed in transition metals to the order of 10 meV [2]. The magnetic moments thus follows Hund’s rules much more closely than those of the $3d$ magnetic materials such as Fe, Co and Ni where the orbital angular momentum is quenched by the crystal electric field [3]. Another useful trend is the regular contraction of the rare earth metallic radius with increasing Z which leads to the property that exchanging rare earths in many compounds either maintains the crystal structure or alters it only slightly. Rare earths have been linked to many extreme behaviours such as the giant magnetocaloric effect exhibited by several R_5T_4

(R=rare earth, T=Si,Ge,Sn) compounds.

The orthorhombic $R_3T_4X_4$ family (R=rare earth, T=Cu,Ag, X=Si,Ge,Sn) represents an extensive series of isostructural compounds with lattice parameters that follow a smooth trend, and where the only magnetic species are the rare earths. These compounds crystallize in an orthorhombic $Gd_3Cu_4Ge_4$-type structure (the crystal structure will be discussed in more detail in Chapter 2). The rare earth atoms occupy two crystallographically distinct sites (4e and 2d), with the transition metal (T) on the 8n site and the X atoms filling two sites (4h and 4f). The systems' structural consistency makes them ideal to study rare earth magnetic ordering mechanisms. The variation of magnetic ordering temperature and magnetic structure is not driven by changes in local symmetry, but by the choice of rare earth and interatomic distances alone.

Despite the apparent simplicity of the system, it exhibits a wealth of varied magnetic behaviour. The $Er_3Cu_4X_4$ (X=Si, Ge, Sn) [4] compounds are prime examples. Each rare earth has nearest neighbours from both rare earth sublattices at comparable distances, and yet the sublattices order independently with the Er-2d sublattice ordering at much higher temperature in all three compounds. Additionally, in all three compounds the moment values for the Er-2d and Er-4e sublattices are quite different. This particular series of compounds highlights quite dramatically how the choice of X has a strong impact on magnetic behaviour. The Er-2d sublattice ordering temperature changes from 5.8 K to 7.9 K to 13.8 K for X=Si, Ge and Sn respectively, while the ordering temperature for the Er-4e sublattice is almost unchanged (3.6 K, 3.2 K and 3.3 K for X=Si, Ge and Sn respectively). A subsequent low temperature survey (down to below 1 K) of the $Er_3Cu_4Ge_4$ compound [5] revealed that the Er-4e order changes at 1.4 K.

Changing the rare earth atoms in the structure leads to equally important changes in the magnetic behaviour. Unlike all the Er members of the compound family, $Tb_3Cu_4Sn_4$ for example, exhibits a single ordering temperature for both rare earth sublattices. The $Tb_3Ag_4Sn_4$ compound undergoes a magneto-structural transition at 28 K and a subsequent moment reorientation at 13 K [6]. As such relatively minor changes in composition can lead to radical changes in magnetic behaviour, the magnetic rare earths in this system sit at the intersection of strong, finely balanced magnetic interactions. These interesting properties, as well as the availability of a large number of members, has made this system the subject of intense study.

As systematic data on the $R_3T_4X_4$ systems have accumulated, several puzzles have emerged. These materials form an intimately related isostructural series for a given choice of T and X, and yet several workers have noted the failure of the observed transition temperatures to follow the expected scaling with the de Gennes factor in the $R_3Cu_4Sn_4$, $R_3Ag_4Sn_4$ and $R_3Cu_4Ge_4$ compound series. It is even unclear which ordering temperature, if the sublattices order separately, should be used to verify the scaling.

So far, most compounds exhibit either simultaneous ordering of both rare earth sublattices, or the 2d sublattice orders at a higher temperature than the 4e sublattice, and only a few systems have been found that have 4e sublattice ordering without magnetic order of the 2d sublattice ($Pr_3Mn_4Sn_4$, $Nd_3Mn_4Sn_4$ [7] and $Nd_3Cu_4Ge_4$ [8]). In metals, the exchange interaction strength between the rare earth moments is inversely proportional to the third power of the interatomic distance and is mediated by conduction electrons via the RRKY interaction. This ordering sequence is thus surprising given that the R-2d atoms would appear to be the more isolated from the other R-2d atoms whereas the R-4e atoms are more closely coordinated. Moreover, the interatomic distances between R-2d and R-4e atoms are not significantly different and so there is no clear reason why the sublattices can order at separate temperatures at all.

Another complication in the $R_3T_4X_4$ family derives from the difficulty in unambiguously determining the ordering temperature from simple bulk magnetic measurements such as magnetization and susceptibility. In some cases, the signal from the initial ordering is weak or absent. The magnetic susceptibility data for $Er_3Cu_4Sn_4$ and $Er_3Cu_4Ge_4$ clearly exhibit a sharp peak at the Er-2d and Er-4e ordering temperatures, and yet only an extremely weak signature was seen for the Er-2d ordering in $Er_3Cu_4Si_4$ [4]. A subsequent magnetic reorientation then provides a more definitive marker which leads to the misidentification of the ordering temperature. This could obviously be the cause of the problem addressed above, where de Gennes scaling is thought to be violated due to an incorrectly determined transition temperature.

Where neutron diffraction data are available, this error can be corrected. For Gd and Sm-based compounds however, the high absorption cross section of natural Gd and Sm makes neutron-based methods challenging and they are rarely attempted. This leaves an unfortunate gap in studies of rare earth compounds as Gd often orders at the highest temperature and is used to set the transition temperature scaling for the rest of the series.

Magnetic properties, while they can be described rather simply, can be quite difficult to measure unambiguously. Each magnetic characterization technique, while offering valuable information, invariably suffers from limitations and explores only specific aspects of magnetic order. Mössbauer spectroscopy provides local information on magnetic environments through both the hyperfine field and the electric field gradient. Neutron scattering on the other hand, yields values for ordered moments and a description of the long-range magnetic order.

Each technique has strengths and weaknesses. While neutron diffraction remains the method of choice for investigating magnetic order in rare earth intermetallics, its blanket sensitivity to all structural and magnetic changes occurring in the sample can make interpretation of the data quite challenging. This is especially true when two or more magnetic species are present, or when structure factor effects lead to weak or highly distributed magnetic scattering. By contrast, Mössbauer spectroscopy cannot be used directly to determine the nature of the long-ranged ordered state as it is a local probe technique, but this limitation brings many advantages as it remains exquisitely sensitive to the presence of magnetic order. Both methods are phase quantitative and provide phase specific data, which is crucial when impurity effects may be present.

I will demonstrate that in the case of the $R_3X_4T_4$ compounds the highly effective combination of Mössbauer spectroscopy and neutron diffraction add a wealth of knowledge to this puzzling system, in some cases resolving outstanding issues and in others adding to the diversity of magnetic behaviour.

Chapter 2

Theoretical Concepts & Background

A number of important concepts must be briefly outlined in order to understand and contextualize the results presented in this thesis. These include the nature of magnetic order in the rare earth compounds, and a more thorough background on the structural and magnetic properties of certain members of the $R_3T_4X_4$ family of compounds.

2.1 Magnetic Order In Rare Earth Compounds

2.1.1 Dipole Interactions and Direct Exchange

The first interaction which might be expected to play a role in the ordering of magnetic moments is the magnetic dipole interaction. Two magnetic dipoles $\vec{\mu}_1$ and $\vec{\mu}_2$ separated by a distance $\mathbf{r}$ have an energy equal to

$$E = \frac{\mu_\circ}{4\pi r^3}\left[\vec{\mu}_1 \cdot \vec{\mu}_2 - \frac{3}{r^2}(\vec{\mu}_1 \cdot \mathbf{r})(\vec{\mu}_2 \cdot \mathbf{r})\right] \tag{2.1}$$

and an order of magnitude calculation yields an energy on the order of 10^{-23} J, equivalent to 1 K, too weak to a be a dominant interaction in this system and be the source of magnetic order [9].

Electrostatic interactions arising from the cost of energy from like charges being close to each other lead to an interaction energy J, called the exchange interaction, between neighbouring spins $\mathbf{S}_1$ and $\mathbf{S}_2$. The effective Hamiltonian can be written as [9]

$$\mathcal{H} = -\mathrm{J}\mathbf{S}_1 \cdot \mathbf{S}_2. \tag{2.2}$$

If the electrons on neighbouring magnetic atoms interact via an exchange interaction, the interaction is called direct exchange. In rare earth intermetallic compounds however, the distance between magnetic moment carrying $4f$ shells of neighbouring rare earth atoms is too large for direct exchange to lead to magnetic order, and a different mechanism needs to be invoked to explain how the moments can interact to yield order.

2.1.2 The RKKY interaction

Conduction electrons in metals can mediate an indirect exchange between magnetic ions, bridging the rather large spatial gap between rare earth $4f$ shells. Ruderman and Kittel [10], in the context of nuclear spin interactions, proposed a mechanism by which conduction electrons interact with the nuclear spin via hyperfine interactions (discussed below) which in turn interacts with the neighbouring nuclear spin. This mechanism was then expanded by Kasuya and Yosida to include indirect exchange of localized inner electron spins [11, 12], and is now commonly referred to as the RKKY interaction. The interaction strength $\mathrm{J}_{\mathrm{RKKY}}$, for an inter-moment distance r and assuming a spherical Fermi surface with a Fermi wave vector k_F, is given by

$$\mathrm{J}_{\mathrm{RKKY}} \propto \frac{-X\cos X + sinX}{X^4} \tag{2.3}$$

where,

$$X = 2k_F r. \tag{2.4}$$

Equation 2.3 leads to an oscillatory exchange interaction, plotted in Figure 2.1, meaning that the coupling between rare earth moments can be either ferromagnetic (FM) or antiferromagnetic (AFM) depending on the interatomic distance and the Fermi wave vector [13].

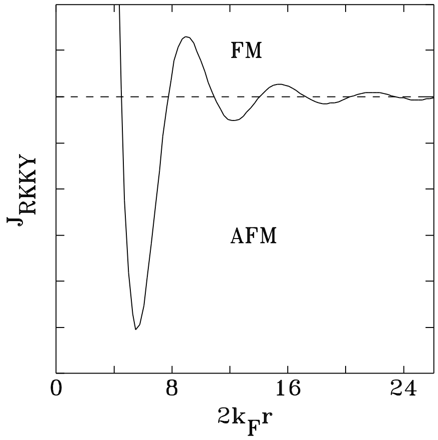

Figure 2.1: Oscillatory behaviour of the RKKY interaction strength J_{RKKY}. If J_{RKKY} is positive, the interaction is ferromagnetic (FM), if J_{RKKY} is negative, the interaction if antiferromagnetic (AFM).

A calculation of the Fermi wave vector for $Tb_3Cu_4Si_4$ yielded 1.672 $Å^{-1}$ [14], which puts J_{RKKY} in the second AFM region in Figure 2.1. This result is substantiated by the fact that most $R_3T_4X_4$ are antiferromagnetic at low temperatures.

2.1.3 Ordered Moment Temperature Dependence and de Gennes Scaling

As stated earlier, the magnetic moment of the rare earths comes from the $4f$ shell lying deep inside the atom, shielding it from orbital quenching. Consequently, the total angular moment J is a good quantum number, and we expect then that the magnetic properties of rare earth compounds to be closely related to the J values.

It is a well known result that for a paramagnet in an applied field B at a temperature T, the magnetization is [15]

$$M = Ng_J J\mu_B B_J(y) \tag{2.5}$$

where N is the number of moments, g_J is the Landé g-factor $g_J = \frac{3}{2} + \frac{S(S+1)-L(L+1)}{2J(J+1)}$, μ_B is the Bohr magneton, $y = gJ\mu_B B/k_B T$ and $B_J(x)$ is the Brillouin function defined as

$$B_J(y) = \frac{2J+1}{2J}\coth\left(\frac{(2J+1)y}{2J}\right) - \frac{1}{2J}\coth\left(\frac{y}{2J}\right). \tag{2.6}$$

Equation 2.5 leads to a saturation magnetization (all moments pointing in the same direction) $M_s = Ng_J J\mu_B$, and the ordered moment is $g_J\mu_B J$. A more detailed derivation is provided in Appendix B.

In order to model the magnetization temperature dependence without an applied field, it is assumed that each moment experiences a field proportional to the magnetization in the material $\mathbf{B} = \lambda\mathbf{M}$, coming from neighbouring moments. If λ is positive, the interaction is ferromagnetic; if λ is negative, the interaction is antiferromagnetic. Using this assumption, known as the mean field theory approximation, and combining it with equation 2.5, the magnetization with respect to temperature can be obtained. Although an analytic solution does not exist, the problem can be solved graphically or, in our case, numerically.

The form of the magnetization with respect to temperature is plotted in Figure 2.2 for $J = \frac{1}{2}$ and $\frac{7}{2}$ as well as the limit as $J \to \infty$, i.e. the classical limit where the Brillouin function becomes a Langevin function [16]. For an antiferromagnet, if the moments are considered as a sum of two sublattices, one with moments pointing ‘up’ and the other with moments pointing ‘down’, Figure 2.2 represents the magnetization of each sublattice in its particular direction. The solution of Equation 2.5 also indicates that the spontaneous magnetization is a second-order phase transition. A second order phase transition has a discontinuity in the second derivative of the free energy and thus the system has a discontinuity in quantities like compressibility or the heat capacity [17].

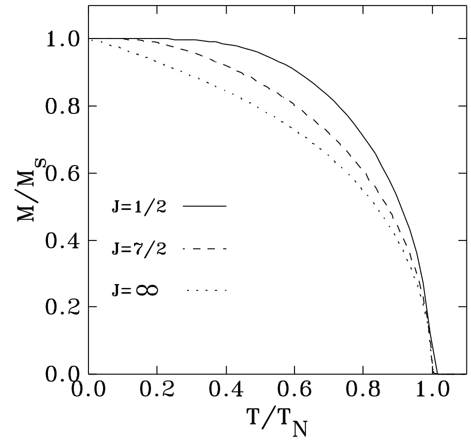

Figure 2.2: The form of the normalized magnetization versus normalized temperature for $J = \frac{1}{2}$ (solid line),$\frac{7}{2}$ (dashed line) and the $J = \infty$ limit (dotted line).

The transition temperature (Curie temperature $\mathrm{T_C}$ for a ferromagnet, Néel temperature $\mathrm{T_N}$ for an antiferromagnet) that results from this calculation is

$$\mathrm{T_{C,N}} \propto g_J \mu_B (J+1) \lambda M_s / 3k_B \tag{2.7}$$

where M_s is the saturation magnetization. If we describe the system in terms of an RKKY exchange interaction parameter $\mathrm{J_{RKKY}}$ and if J is considered to be the good quantum number (as it is with the rare earths), it can be shown that the transition temperature is [18]

$$\mathrm{T_{C,N}} \propto \mathrm{J_{RKKY}} \times (g_J - 1)^2 J(J+1). \tag{2.8}$$

The dependence of $\mathrm{T_{C,N}}$ with J is called de Gennes scaling and $(g_J - 1)^2 J(J+1)$ is called the de Gennes factor. The relevant quantum numbers as well as the de Gennes scaling factor for the trivalent rare earths are listed in Table 2.1. The scaling has been shown to be quite successful mostly for the heavy rare earths, Gd through Yb [19]. The Gd compounds should have the highest transition temperature ($\mathrm{Gd^{3+}}$ having a de Gennes factor of 15.75) and the Yb compounds should have the lowest transition temperature ($\mathrm{Yb^{3+}}$ having a de Gennes factor of 0.32).

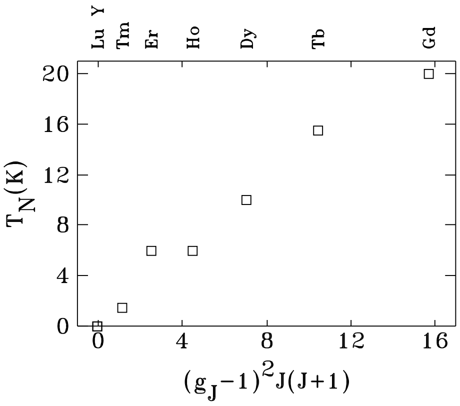

Figure 2.3: Example of de Gennes scaling for the magnetic transition temperature in the RNi_2B_2C compound series. Taken from Cho *et al.* [20] and references therein.

The RNi_2B_2C system provides an illustrative example of de Gennes scaling for the magnetic transition temperature. A plot of the de Gennes factor dependence of T_N is shown in Figure 2.3 (taken from Cho *et al.* [20]).

ion	shell	S	L	J	g_J	$(g_J-1)^2J(J+1)$	Metallic Radius (Å) [21]
Ce^{3+}	$4f^1$	$\frac{1}{2}$	3	$\frac{5}{2}$	$\frac{6}{7}$	0.18	1.825
Pr^{3+}	$4f^2$	1	5	4	$\frac{4}{5}$	0.80	1.828
Nd^{3+}	$4f^3$	$\frac{3}{2}$	6	$\frac{9}{2}$	$\frac{72}{99}$	1.84	1.821
Pm^{3+}	$4f^4$	2	6	4	$\frac{3}{5}$	3.20	1.810
Sm^{3+}	$4f^5$	$\frac{5}{2}$	5	$\frac{5}{2}$	$\frac{2}{7}$	4.46	1.802
Eu^{3+}	$4f^6$	3	3	0	–	–	1.799
Eu^{2+}	$4f^7$	$\frac{7}{2}$	0	$\frac{7}{2}$	2	15.75	2.042
Gd^{3+}	$4f^7$	$\frac{7}{2}$	0	$\frac{7}{2}$	2	15.75	1.802
Tb^{3+}	$4f^8$	3	3	6	$\frac{3}{2}$	10.50	1.782
Dy^{3+}	$4f^9$	$\frac{5}{2}$	5	$\frac{15}{2}$	$\frac{4}{3}$	7.08	1.773
Ho^{3+}	$4f^{10}$	2	6	8	$\frac{5}{4}$	4.50	1.766
Er^{3+}	$4f^{11}$	$\frac{3}{2}$	6	$\frac{15}{2}$	$\frac{6}{5}$	2.55	1.757
Tm^{3+}	$4f^{12}$	1	5	6	$\frac{7}{6}$	1.17	1.746
Yb^{3+}	$4f^{13}$	$\frac{1}{2}$	3	$\frac{7}{2}$	$\frac{8}{7}$	0.32	1.740
Yb^{2+}	$4f^{14}$	0	0	0	–	–	1.940
Lu^{3+}	$4f^{14}$	0	0	0	–	–	1.734

Table 2.1: Relevant free-ion quantum numbers and de Gennes scaling factors for the rare earths.

2.2 The $Gd_3Cu_4Ge_4$-type Crystal Structure

All members of the $R_3T_4X_4$ family of compounds crystallize in the orthorhombic ($a \neq b \neq c$, $\alpha = \beta = \gamma = 90°$) $Gd_3Cu_4Ge_4$-type structure which adopts the $Immm$ (#71) space group [22]. An overview of the $Immm$ space group is provided in Appendix D. The sites occupied by the rare earth (R), transition metal (T) and the main group element (X) along with the site symmetries are listed in Table 2.2. The structure is best described as two planes of atoms parallel to the ab-plane, alternating along the c-axis. The full unit cell is shown in Figure 2.4(a), and the planes are shown in Figures 2.4(b) and 2.4(c). Typical interatomic distances and lattice parameters are listed in Appendix A.

The fractional coordinates do not vary significantly from compound to compound and are typically: x_R=0.13, x_T=0.3, y_T=0.2, x_X=0.2 and y_X=0.2. Some workers use the rare earth 2d site as the origin for the crystal structure, however throughout this thesis the sites will be labeled using the convention laid out in Table 2.2.

The rare earth neighbours of the rare earth 2d site (R-2d) are shown on the left of Figure 2.5 and the rare earth neighbours of the rare earth 4e site (R-4e) are shown on the right of Figure 2.5. The R-2d neighbours of the R-2d site, along the c-axis, are farther than the R-4e neighbours which lie in the same ab-plane as the central R-2d. For the R-4e atom, the situation is almost reversed. The nearest rare earth is an R-4e but the two R-2d neighbours are closer than the remaining two R-4e neighbours. Neither the local symmetry of the rare earths, nor the interatomic distances, leads to an isolated R-2d or R-4e sublattice. Even if the difference in the nearest neighbour coordination does have a significant impact on the ordering temperature, the R-4e sublattice is more likely to order at higher temperatures than the R-2d sublattice. The observation that the R-2d site most often orders at higher temperatures is thus surprising. For the sake of clarity the T and X atoms are omitted from Figure 2.5, but it is worth noting that out of all the nearest neighbours, the rare earths are the farthest, with T and X atoms being closer.

Element Type	Site	Symmetry	Coordinates			Atoms
			x	y	z	
R	2d	mmm	$\frac{1}{2}$	0	$\frac{1}{2}$	$(\frac{1}{2}, 0, \frac{1}{2})$, $(0, \frac{1}{2}, 0)$
R	4e	$2mm$	x_R	0	0	$(x_R, 0, 0)$, $(1 - x_R, 0, 0)$, $(x_R + \frac{1}{2}, \frac{1}{2}, \frac{1}{2})$, $(\frac{1}{2} - x_R, \frac{1}{2}, \frac{1}{2})$
T	8n	$\cdot\cdot m$	x_T	y_T	0	$(x_T, y_T, 0)$, $(x_T, 1 - y_T, 0)$, $(1 - x_T, y_T, 0)$, $(1 - x_T, 1 - y_T, 0)$, $(x_T + \frac{1}{2}, y_T + \frac{1}{2}, \frac{1}{2})$, $(x_T + \frac{1}{2}, \frac{1}{2} - y_T, \frac{1}{2})$, $(\frac{1}{2} - x_T, y_T + \frac{1}{2}, \frac{1}{2})$, $(\frac{1}{2} - x_T, \frac{1}{2} - y_T, \frac{1}{2})$
X	4f	$2mm$	x_X	$\frac{1}{2}$	0	$(x_X, \frac{1}{2}, 0)$, $(1 - x_X, \frac{1}{2}, 0)$ $(x_X + \frac{1}{2}, 0, \frac{1}{2})$, $(\frac{1}{2} - x_X, 0, \frac{1}{2})$
X	4h	$m2m$	0	y_X	$\frac{1}{2}$	$(0, y_X, \frac{1}{2})$, $(0, 1 - y_X, \frac{1}{2})$, $(\frac{1}{2}, y_X + \frac{1}{2}, 0)$, $(\frac{1}{2}, \frac{1}{2} - y_X, 0)$

Table 2.2: Crystallographic sites (with the element type occupying that site), point symmetries, fractional coordinates, and atomic positions of the $Gd_3Cu_4Ge_4$-type structure. The fractional coordinates do not vary significantly from compound to compound and are typically: x_R=0.13, x_T=0.3, y_T=0.2, x_X=0.2 and y_X=0.2

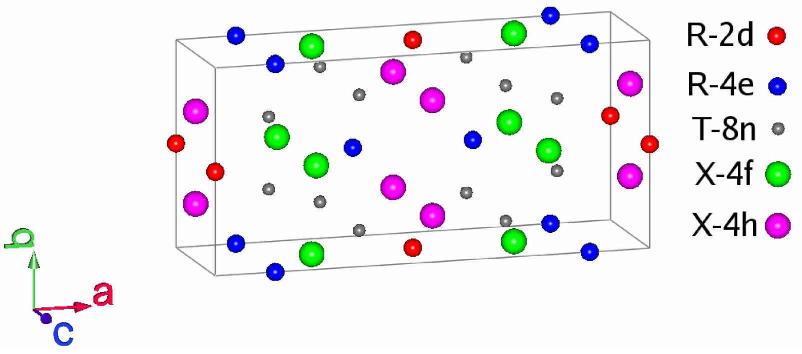

(a) The $Gd_3Cu_4Ge_4$-type structure unit cell.

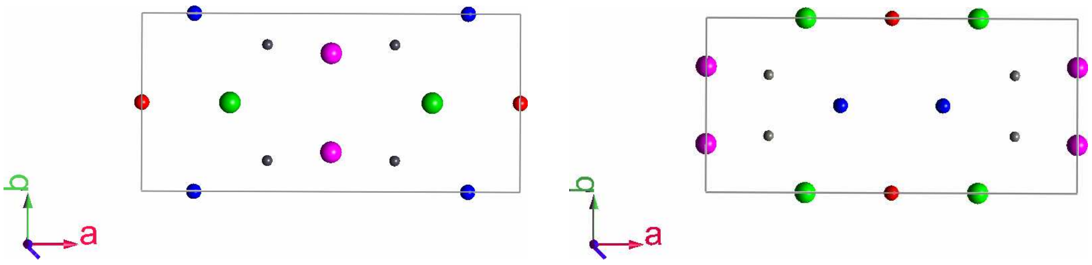

(b) Atoms lying in the *ab*-plane in the unit cell of the $Gd_3Cu_4Ge_4$-type structure

(c) Atoms lying in the *ab*-plane halfway along the *c*-axis in the unit cell of the $Gd_3Cu_4Ge_4$-type structure

Figure 2.4: View of the $Gd_3Cu_4Ge_4$-type structure layers.

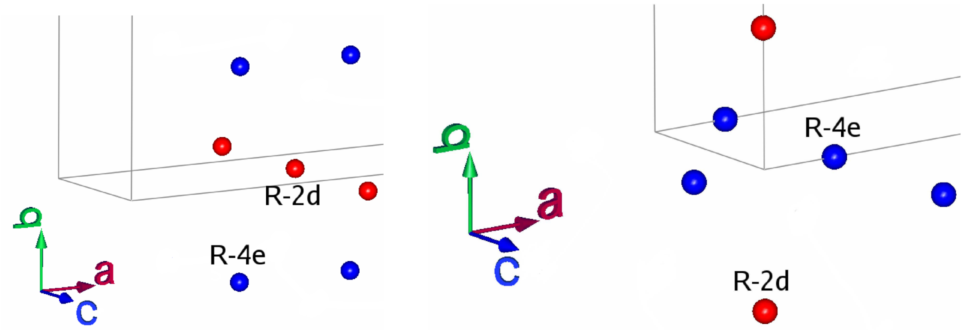

Figure 2.5: Left: R-2d site rare earth neighbours in the $Gd_3Cu_4Ge_4$-type structure. Right: R-4e site and its rare earth neighbours in the $Gd_3Cu_4Ge_4$-type structure.

The Sn atoms in the structure, while they are non-magnetic, are used to probe the magnetism in the $R_3T_4Sn_4$ compounds due to the transferred hyperfine field at the ^{119}Sn nuclei from neighbouring moment carrying rare earths (discussed in more detail below). The rare earth nearest neighbours to the Sn-4f site are shown on the left of Figure 2.6, and the rare earth nearest neighbours to the Sn-4h site are shown on the right of Figure 2.6. As both Sn sites in the $Gd_3Cu_4Ge_4$-type structure have first neighbours from each of the two rare earth sublattices, the transferred hyperfine field observed at each Sn site should be sensitive to the magnetic ordering on both rare earth sites in the compound. Although the R-4e moments could be antiferromagnetically arranged and cancel at each Sn site, and the R-2d moments could do the same at the Sn-4h site, the Sn-4f site has a single R-2d neighbour and should be sensitive to ordering of the R-2d sublattice regardless of the magnetic structure adopted.

2.3 Describing Magnetic Structures

Even above the magnetic ordering temperature the rare earth atoms carry a moment but it is only below the ordering temperature that they are spatially organized in some regular fashion. The direction of the magnetic moments with respect to the crystal

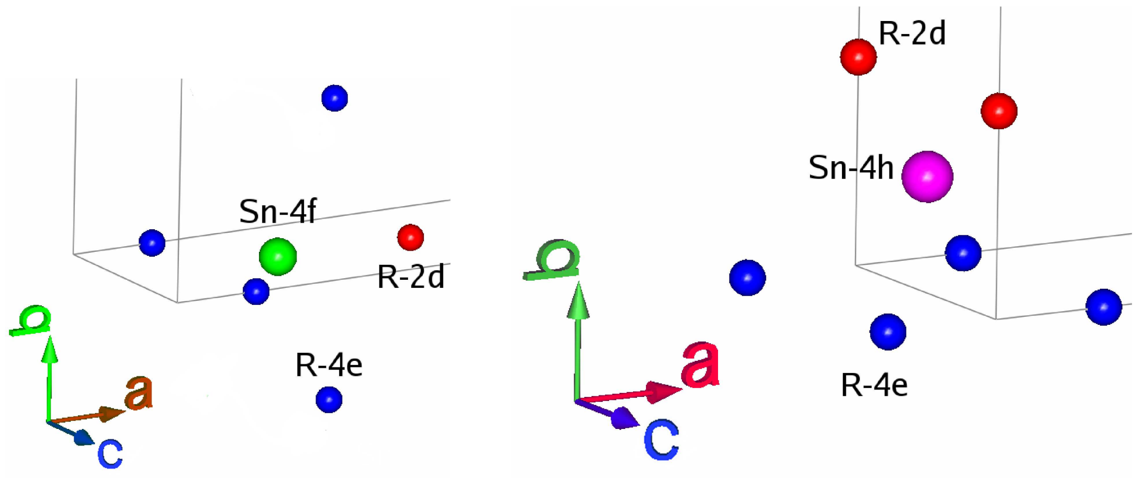

Figure 2.6: Left: Sn-4f site rare earth neighbours in the $Gd_3Cu_4Ge_4$-type structure. Right: Sn-4h site rare earth neighbours in the $Gd_3Cu_4Ge_4$-type structure.

lattice and each other in a material is called the magnetic structure. In a crystalline solid in which the rare earth magnetic moments are responsible for the magnetic properties of the material, the magnetic moments are localized on the rare earth atomic sites. It is thus natural to use group theory as it applies to crystallography to describe magnetic order.

The mathematics of crystallographic groups and magnetic groups is well established and a thorough and detailed discussion can be found elsewhere [23, 24]. The focus of this section will be the key results necessary to describe a magnetic structure completely. These results will also be necessary to analyze the magnetic neutron diffraction data and to interpret the results.

2.3.1 The magnetic propagation vector k

We begin by considering the magnetic propagation vector **k** of magnetic moment modulation. The propagation of the magnetic structure through the crystal is described using plane waves or *Bloch* waves, much like the treatment of phonons, or band structure. **k** is the wave vector corresponding to a frequency in terms of unit cells. If the components of $\mathbf{k}$ are rational fractions of the reciprocal lattice vectors, the magnetic lattice can be simply expressed as an integer number of crystallographic lattices in a given direction. For example a propagation vector $\mathbf{k} = (\frac{1}{2}, 0)$ (limiting ourselves to two dimensions for simplicity) means that the magnetic unit cell is twice as large in the a direction as the crystallographic unit cell, and has the same size in the b direction (the zero component of the wave number leads to an infinite frequency which corresponds to no modulation at all: the moments are simply parallel all through the crystal in that direction). Figure 2.7 is an illustration of the $\mathbf{k} = (\frac{1}{2}, 0)$ case with a moment pointing along the b-axis in a simple rectangular lattice which exhibits cell doubling in the a direction, while the b magnetic and crystal parameters remain the same.

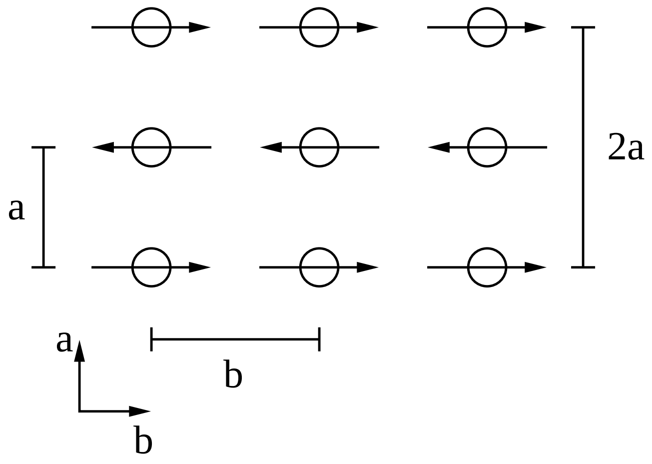

Figure 2.7: Illustrative example of the magnetic structure described by the propagation vector $\mathbf{k} = (\frac{1}{2}, 0)$ on a simple rectangular lattice with a moment pointing along b.

A magnetic structure will be termed commensurate if the propagation vector $\mathbf{k}$ leads to a simple relation between the sizes of the crystal and magnetic lattices. For instance, in the example with $\mathbf{k} = (\frac{1}{2}, 0)$, the magnetic structure would be commensurate since the magnetic lattice is a factor of two larger in the a direction and a factor of one in the b direction. A magnetic structure will be termed incommensurate if no such simple relation exists. In essence if the $\mathbf{k}$ components are rational fractions, the structure is commensurate, if not, it is incommensurate.

2.3.2 Describing the magnetic moment

The Bloch waves that describe the i^{th} magnetic moment in the j^{th} cell in the crystal are written as

$$\mathbf{m}_{ij} = \boldsymbol{\Psi}_i \mathrm{e}^{-2\pi i \mathbf{k}\cdot\mathbf{t}_j} \tag{2.9}$$

where the vector $\boldsymbol{\Psi}_i$ is defined as the moment in the zeroth cell, $\mathbf{k}$ is the propagation vector, and $\mathbf{t}_j$ is the translation vector in terms of the unit cell from the zeroth cell to the j^{th} cell. $\boldsymbol{\Psi}_i$ is expressed as a sum of its ν non-zero components:

$$\boldsymbol{\Psi}_i = \sum_{\nu} C_{\nu}^{i} \psi_{\nu} \tag{2.10}$$

where ψ_ν are unit vectors in each crystallographic direction and C_ν is the magnetic moment along each crystallographic direction.

The lattice translation vector will depend on the Bravais lattice that is being considered. An illustrative example with $\mathbf{k} = (\frac{1}{2}, 0)$ is shown in Figure 2.8. The lattice translation vectors considered in this case are $\mathbf{t}_1 = (2, 4)$ and thus the a component of the moments point in the same direction, and $\mathbf{t}_2 = (3, 1)$ which leads to the a component of the moment pointing in the opposite direction. In this manner, every moment in the structure is uniquely determined. For primitive lattices, the $\mathbf{t}_j$ vector has only integer components. Body centered lattices however have a $\mathbf{t}_j$ of the form

$$\mathbf{t}_j = (n_a, n_b, n_c) + n_I \left(\frac{1}{2}, \frac{1}{2}, \frac{1}{2}\right) \tag{2.11}$$

where n_a, n_b, n_c and n_I are integers. An important consequence of Equation 2.11 is that a description of the magnetic structure of a body-centered lattice will not explicitly include a reference to the body-centered moment, since Equation 2.9 is used to generate it. Thus, although there are two rare earth 2d moments in the unit cell of the $Gd_3Cu_4Ge_4$ type structure, only one will be specified. Likewise, although there are four rare earth 4e moments, only two will be specified.

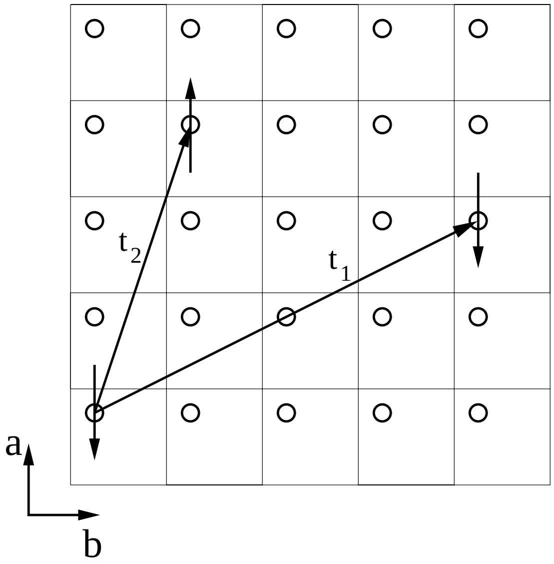

Figure 2.8: Illustrative example of how the propagation vector $\mathbf{k}$, basis vector, and lattice translation vector $\mathbf{t}_j$ uniquely determine the direction of all the moments in the crystal.

A magnetic moment is a real entity and yet clearly equation 2.9 could lead to a complex moment. To solve this problem the moment needs to be described with contributions from two propagation vectors: $\mathbf{k}$ and $-\mathbf{k}$. In this case the moment is expressed as a sum of the $\mathbf{k}$ and $-\mathbf{k}$ contributions

$$\mathbf{m}_{ij} = \frac{1}{2}\left(\mathbf{\Psi}_i^{\mathbf{k}} e^{-2\pi i \mathbf{k}\cdot\mathbf{t}_j} + \mathbf{\Psi}_i^{-\mathbf{k}} e^{2\pi i \mathbf{k}\cdot\mathbf{t}_j}\right) \tag{2.12}$$

where $\mathbf{\Psi}_i^{-\mathbf{k}} = \mathbf{\Psi}_i^{\mathbf{k}*}$. Since there are no complex basis vectors needed in this study, the moment for this case can be defined as

$$\mathbf{m}_{ij} = \mathbf{\Psi}_i^{\mathbf{k}} \cos(-2\pi \mathbf{k}\cdot\mathbf{t}_j). \tag{2.13}$$

2.3.3 Computing the basis vectors with Irreducible Representations

The mathematical theory developed to find the symmetry allowed basis vectors ψ_ν given a crystallographic space group, atomic positions and a magnetic propagation vector $\mathbf{k}$, is called the theory of Irreducible Representations.

A representation of a group is a set of matrices which obey the multiplication table of that group. If there exists a unitary transformation that transforms all of the matrices into the same block diagonal form the representation is called reducible. If there exists no such transformation, the representation is called irreducible. The irreducible representations are of particular significance since they are the smallest unique blocks out of which all other representations are made.

With a $\mathbf{k}$ vector determined, the symmetry operations of the crystallographic group $G_\circ$ that leave the $\mathbf{k}$ vector invariant form what is called the little group $G_{\mathbf{k}}$, and the irreducible representations of $G_{\mathbf{k}}$ are found. The magnetic representation, Γ_{mag}, describes the result of the symmetry operations on both the atomic positions and the orientation of the magnetic moments. Γ_{mag} can be decomposed into the irreducible representations of $G_{\mathbf{k}}$:

$$\Gamma_{mag} = \sum_i n_i \Gamma_i \tag{2.14}$$

where n_i is the number of times the representation Γ_i appears in the Γ_{mag} representation. n_i is also the number of basis vectors allowed by symmetry for each Γ_i: if $n_i = 1$ the magnetic moment can only be along one of the crystallographic axes, if $n_i = 2$ the magnetic moment has two non-zero components, and if $n_i = 3$ the moment can point in any direction.

For each irreducible representation Γ_i the basis vectors of Equation 2.10 are obtained using unit vectors in each crystallographic direction and projecting from them the part that transforms according to the Γ_i representation. Thus, we obtain for each Γ_i a magnetic moment configuration related by symmetry.

IR	Basis Vectors	Atom	Basis Vector components					
			Re(a)	Re(b)	Re(c)	Im(a)	Im(b)	Im(c)
Γ_3	ψ_1	$(\frac{1}{2}, 0, \frac{1}{2})$	1	0	0	0	0	0
Γ_5	ψ_2	$(\frac{1}{2}, 0, \frac{1}{2})$	0	1	0	0	0	0
Γ_7	ψ_3	$(\frac{1}{2}, 0, \frac{1}{2})$	0	0	1	0	0	0

Table 2.3: Basis vectors for the space group $Immm$ with $\mathbf{k} = (0, 0, 0)$ for the 2e site.

The calculations described above are quite complex and cumbersome. Thankfully a number of computer programs exist that compute the basis vectors given a propagation vector $\mathbf{k}$, a space group and the crystallographic sites under consideration. In this study the program SARAh [25] was used to compute the needed IRs and their basis vectors.

As an example, we can consider the 2d site (atoms at $(\frac{1}{2}, 0, \frac{1}{2})$ and $(0, \frac{1}{2}, 0)$) in the $Immm$ space group with a propagation vector $\mathbf{k} = (0, 0, 0)$. The results of the basis vector calculation performed by SARAh are shown in Table 2.3. There will be one basis vector for each allowed ordering direction, and components will be specified for each atom in the unit cell. The basis vectors of Table 2.3 can then be combined with equations 2.10 and 2.9 to obtain the symmetry allowed magnetic structures: Γ_3 allows order along the a-axis, Γ_5 allows order along the b-axis and Γ_7 allows order along the c-axis. Since $\mathbf{k} \cdot \mathbf{t}_j$ will always be zero, all three structures are ferromagnetic. The value of the moment will be determined by the C_ν coefficients of equation 2.10 obtained from a fit to experimental data.

It is important to note that unlike crystallography, magnetic group theory does not have a universal nomenclature. The designations of the IRs can change depending on the software used to perform the calculation. The basis vectors thus must be quoted and the names given to the IRs are only internal references.

The results of Table 2.3 require slightly more interpretation for body centered lattices. As was mentioned in the previous sections, the body centering operation that generates the $(0, \frac{1}{2}, 0)$ atom can be combined with the appropriate lattice translation vector $\mathbf{t}_j$ and the propagation vector to obtain the moment direction directly from Equation 2.9. The same issue will be encountered for the 4e site where only two sets of components for each basis vector, for the atoms $(x_R, 0, 0)$, $(1 - x_R, 0, 0)$, will be quoted and the remaining two, for $(\frac{1}{2}, y_X + \frac{1}{2}, \frac{1}{2})$ and $(\frac{1}{2}, \frac{1}{2} - y_X, \frac{1}{2})$, can be generated using Equation 2.9.

2.3.4 Landau Theory

It is useful to consider irreducible representations in the context of the thermodynamics of phase transitions via what is known as Landau Theory. As discussed above, magnetic order is a second order phase transition, in which spatially disordered moments begin to follow a specific and static arrangement below a transition temperature. As the temperature is decreases and passes the magnetic transition temperature the symmetry of the system is lowered. In Landau theory, we define a function ρ which characterizes the symmetry of the magnetic moments in the crystal [26],

$$\rho = \sum_n \sum_i c_i^n \psi_i^n \tag{2.15}$$

where ψ_n^i are the basis functions of the irreducible representations of the crystal. Above the transition temperature, ρ is invariant under all operations of $G_\circ$ and below it is invariant under all operations of some different group G_1 of lower symmetry.

Landau considered an expansion of the free energy Φ near the transition temperature

$$\Phi = \Phi_\circ + \sum_n A^n \sum_i (c_i^n)^2 \tag{2.16}$$

where the A^n coefficients are functions of pressure and temperature. Landau argued that at the transition temperature itself, the equilibrium values of c_i^n must be zero, and above the transition temperature all A^n must be positive. The sign of one A^n changes at the transition temperature and leads to the appearance of non zero c_i^n

corresponding to the i^{th} irreducible representation [27].

Landau theory thus yields the result that in a second order magnetic phase transition we expect the symmetry of the magnetic phase to involve a single irreducible representation. It should be noted however that if two irreducible representations are very close or equal in energy, a degenerate state could arise and the symmetry is a mixing of the two.

2.4 Properties of some $R_3T_4X_4$ Compounds

The lattice parameters for the $R_3(Cu, Ag)_4Sn_4$ compounds are shown in Figure 2.9 [8, 28, 29, 30, 31, 32, 33, 34]. The expected contraction trend stemming from the steadily decreasing metallic radii of the rare earths is clearly observed.

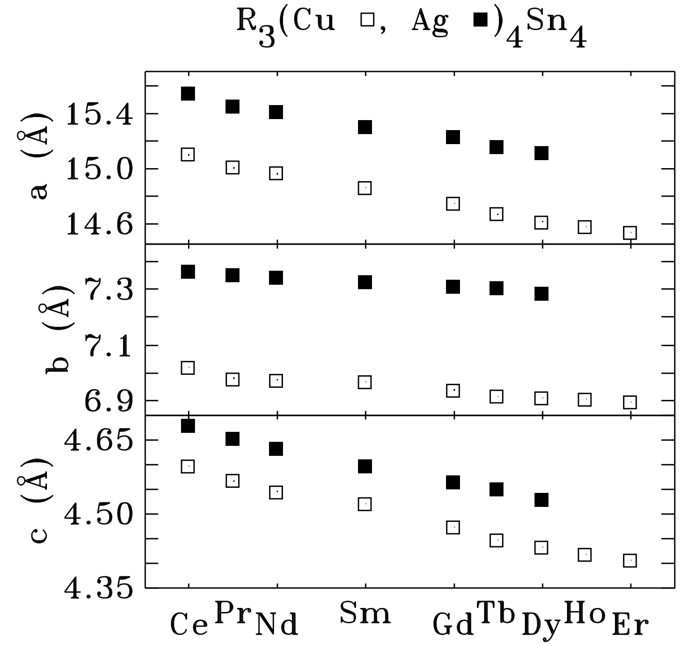

Figure 2.9: Lattice parameters for the $R_3Cu_4Sn_4$ (□) and $R_3Ag_4Sn_4$ (■) compounds [8, 28, 29, 30, 31, 32, 33, 34].

The magnetic properties of the $R_3(Cu, Ag)_4Sn_4$ compounds are however quite var-

Compound	T_N 2d (K)	T_N 4e (K)	Reorientation Temperature (K)	Magnetic Structure Type	Ref.
$Ce_3Cu_4Sn_4$	10.3(n)		7.8(n) - 2.6(n)	incom.+com.	[35]
$Pr_3Cu_4Sn_4$	11(n)			com.	[28]
$Nd_3Cu_4Sn_4$	1.8(m-h)- $<$ 1.5(n)				[29, 28]
$Sm_3Cu_4Sn_4$	8.79(m)		7.79(m) - 5.36(m)		[29]
$Gd_3Cu_4Sn_4$	13(m)		8.4(m)		[34]
$Tb_3Cu_4Sn_4$	17.5(n)			incom.	[30]
$Dy_3Cu_4Sn_4$	15(n)			incom.	[30]
$Ho_3Cu_4Sn_4$	7.6 (h)	3.3(h)	2.3(h) - 4.4(h) - 5.5(h)	incom.+com.	[36]
$Er_3Cu_4Sn_4$	5.9(n)	2(n)	5.6(n)	incom.	[4, 37]

Table 2.4: Magnetic transition temperatures and lower temperature magnetic transitions of the $R_3Cu_4Sn_4$ compounds, as measured by heat capacity (h), neutron diffraction (n), Mössbauer spectroscopy (Moss) and bulk magnetization (m). The magnetic structure type, commensurate (com.) or incommensurate (incom.) is also listed.

ied and complex. A summary of the magnetic properties of the $R_3Cu_4Sn_4$ compounds is given in Table 2.4 and for the $R_3Ag_4Sn_4$ compounds in Table 2.5. The transition temperatures are labeled by the experimental technique used to obtain them: (h) is for a heat capacity measurement, (n) is for neutron diffraction, (Moss) is for Mössbauer spectroscopy, (m) is for bulk magnetization data. The magnetic structure type is referred to incom., meaning incommensurate, and com. meaning commensurate.

In the $R_3Cu_4Sn_4$ series, the $Pr_3Cu_4Sn_4$ system is by far the simplest, locking into an AFM commensurate structure with a common ordering temperature for both rare earth sublattices [28]. The magnetic structures of $Tb_3Cu_4Sn_4$ and $Dy_3Cu_4Sn_4$ are slightly more complicated with a single ordering temperature as well, but an incommensurate structure [30]. The $Ce_3Cu_4Sn_4$ system is yet more complex. While there is a single ordering temperature for both Ce sublattices, they adopt different incommensurate magnetic structures, and only at lower temperature do they adopt a common commensurate structure [35]. The $Er_3Cu_4Sn_4$ system, as mentioned in the introduction, has separate ordering temperatures and structures for each sublattice [4, 37]. The $Ho_3Cu_4Sn_4$ system seems to present the greatest difficulty, even with neutron diffraction data available, as the first neutron diffraction results [30] were revised and several additional transitions were found [36]. It too has separate ordering temperatures for the rare earth sublattices. $Nd_3Cu_4Sn_4$ is a somewhat odd case. Although magnetization and heat capacity measurements indicated an ordering temperature of 1.8 K [29], neutron diffraction measurements showed no magnetic scattering down to 1.5 K [28]. Magnetization measurements on $Sm_3Cu_4Sn_4$ yielded three separate transitions temperatures [29], and two for $Gd_3Cu_4Sn_4$ [34]. The understanding of the magnetism in the Sm and Gd based compounds suffers from the major limitation of a lack of neutron diffraction as the experimental difficulties involved (discussed in Chapter 3) often discourage workers from performing the measurements, and leave a rather large gap in the understanding of rare earth compound series as will be shown later.

The magnetic behaviour of the $R_3Ag_4Sn_4$ series of compounds is somewhat simpler than the Cu series. There are no examples of separate ordering temperatures for each rare earth sublattice and fewer of the compounds undergo magnetic transitions below the initial ordering temperature. It is important to note, however, that the Ho and Er compounds which show such complexity in the Cu series, have yet to be successfully prepared in the Ag series. The $Ce_3Ag_4Sn_4$ compound presents a puzzling absence of magnetic signal in the neutron diffraction data at 1.5 K [32], well below the ordering temperature of 9 K measured by magnetic susceptibility [31], much like the $Nd_3Cu_4Sn_4$ compound discussed above. Another outlier in the Ag series is the magneto-structural transition in $Tb_3Ag_4Sn_4$, found by ^{119}Sn Mössbauer spectroscopy,

Compound	T_N 2d (K)	T_N 4e (K)	Reorientation Temperature (K)	Magnetic Structure Type	Ref.
$Ce_3Ag_4Sn_4$	9(m)-<1.5(n)				[31, 32]
$Pr_3Ag_4Sn_4$	12(n)		9	incom. + com.	[8]
$Nd_3Ag_4Sn_4$	5(n)			com.	[8]
$Sm_3Ag_4Sn_4$	9(m)				[33]
$Gd_3Ag_4Sn_4$	8(m)				[33]
$Tb_3Ag_4Sn_4$	28(n-Moss)		13(Moss)		[6]
$Dy_3Ag_4Sn_4$	16(n)		14(n)	com. + incom.	[38]
$Ho_3Ag_4Sn_4$	NA				
$Er_3Ag_4Sn_4$	NA				

Table 2.5: Magnetic transition temperatures and lower temperature magnetic transitions of the $R_3Ag_4Sn_4$ compounds, as measured by neutron diffraction (n), Mössbauer spectroscopy (Moss) and bulk magnetization (m). The magnetic structure type, commensurate (com.) or incommensurate (incom.) is also listed.

observed in no other $R_3T_4X_4$ compound [6]. Finally, as stated earlier, there is the complete absence of neutron diffraction data on the Sm and Gd compounds.

The data currently available on the $R_3T_4X_4$ system, especially the compounds listed in Tables 2.4 and 2.5, lead to a rather puzzling problem. Despite the fact that these materials form intimately related isostructural series for a given choice of T and X, the expected transition temperature scaling with the de Gennes factor fails. It is tempting to invoke an exotic mechanism to explain this scaling failure, especially in light of the complex and even independent ordering of the two rare earth sublattices. However, such an approach may miss the real cause of the failure and could also lead to the wrong series members being identified as the anomalous elements.

As Gd alloys typically have the highest ordering temperatures of an isostructural rare earth series, by virtue of Gd's maximal de Gennes factor, it is common practice to establish the expected scaling behaviour by joining the Gd point to the origin. The apparent scaling failure may have at its origin a simple but flawed choice of the Gd compounds as reference points. Figure 2.10 illustrates the scaling behaviour observed if one ignores the two Gd compounds entirely. Overall, de Gennes scaling works quite well, with the Ce and Pr compounds as obvious outliers. As was stated earlier, the light rare earths often fail to follow the same scaling as the heavy rare earths [19], and specific heat measurements on $Ce_3Cu_4Sn_4$ [34] and $Pr_3Cu_4Sn_4$ [29] show evidence for complex ordering (Ce) and significant contributions from nearby crystal field split levels (Pr) that likely play a role in the scaling failure. The $Tb_3Ag_4Sn_4$ magneto-structural transition, precludes it from being considered as likely to follow the same scaling. With the five outliers removed from consideration, it is the two Gd compounds that emerge as clear anomalies. Two possible explanations for the Gd anomaly are possible: (1) the reported transition temperatures are incorrect, or (2) the two Gd compounds are indeed different.

The Gd compound poses the same problem in the $R_3Cu_4Ge_4$ series of compounds [8, 35, 39, 40, 41] as can readily seen from Figure 2.11. Again, the use

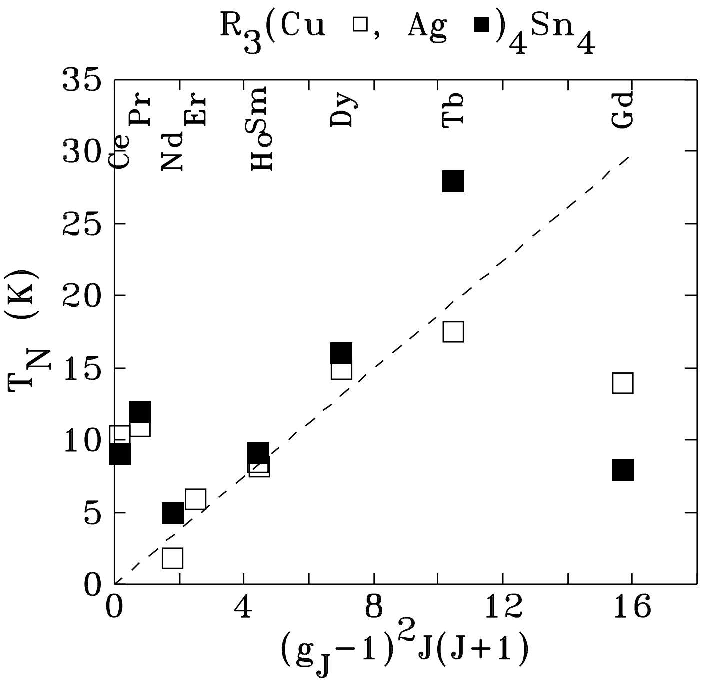

Figure 2.10: The highest magnetic transition temperatures in the $R_3Cu_4Sn_4$ (□) and $R_3Ag_4Sn_4$ (■) compounds versus the de Gennes factor $(g_J-1)^2J(J+1)$ [4, 6, 8, 28, 29, 30, 31, 32, 33, 34, 35, 36, 37, 38].

of the Gd compound to set the scaling leads to a severe breakdown, whether the value obtained from heat capacity (8.5 K [40]), magnetic susceptibility (11 K [42]) or magnetization (12 K [43]) is used. However, if the Gd compound is omitted from consideration, the scaling works quite well, with again the exception of the Pr compound.

Ordinarily the determination of the ordering temperature would not be an issue as, for most systems, reliable values are readily obtained by susceptibility, magnetization or neutron diffraction. However as can be seen in Tables 2.4 and 2.5 there are internal contradictions depending on the experimental technique. Magnetic susceptibility is a bulk measurement that is weakened by indistinguishability between primary phase and impurity phase effects, a problem exacerbated by the sometimes

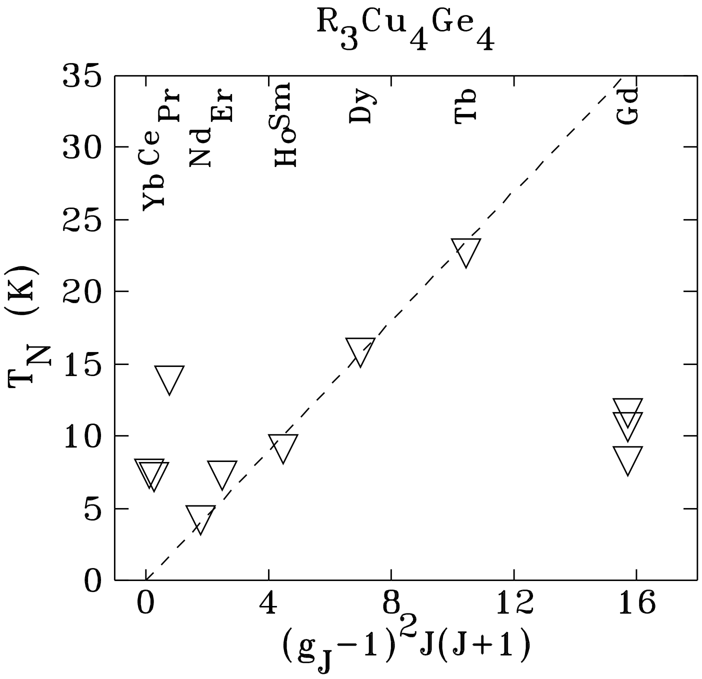

Figure 2.11: The highest magnetic transition temperatures in the $R_3Cu_4Ge_4$ (▽) compounds plotted versus the de Gennes factor $(g_J - 1)^2 J(J + 1)$ [8, 35, 39, 40, 41].

subtle features interpreted as magnetic transition temperatures ($Sm_3Cu_4Sn_4$ being a prime example [29]). Such a problem casts doubt on the values where neutron diffraction data are either unavailable (the Sm and Gd compounds) or where no magnetic signal is observed at all ($Nd_3Cu_4Sn_4$ and $Ce_3Ag_4Sn_4$).

In the results that follow, it will be shown how data from ^{119}Sn Mössbauer spectroscopy, ^{155}Gd Mössbauer spectroscopy, and neutron scattering have been used to develop a much clearer understanding of the magnetic ordering in the $R_3T_4X_4$ system. It will also be demonstrated that neutron diffraction should not be used in isolation, and that by bringing more than one technique to bear on a problem, a much clearer and less ambiguous picture emerges.

Chapter 3

Experimental Methods

In order to improve the understanding of the nature of the magnetic order in the $R_3T_4X_4$ compounds, the use of experimental methods which have the most unambiguous signatures of magnetic order are essential. This is especially true when there are apparent contradictions between experimental techniques. Experimental techniques that yield a magnetic contribution only with ordered moments remove ambiguities in the interpretation, especially if the magnetic contributions are phase quantitative.

3.1 Mössbauer Spectroscopy

We begin with Mössbauer spectroscopy, the most widely used experimental technique in this work.

3.1.1 The Mössbauer Effect

When a free atom emits a photon in a nuclear decay, the nucleus recoils to conserve the total momentum of the system. If we define E_e as the excited state energy, and E_g as the ground state energy, $E = E_e - E_g$ is the energy lost by the nucleus during the emission. If the nucleus is initially at rest, the velocity change it experiences after the emission is v, its mass is M, and the energy of the emitted photon is E_γ. Using energy conservation we get

$$E = \frac{1}{2}Mv^2 + E_\gamma \tag{3.1}$$

thus the difference in energy between E and E_γ is

$$E - E_\gamma = \frac{1}{2}Mv^2. \tag{3.2}$$

$\frac{1}{2}Mv^2$ is the recoil kinetic energy E_R. Using momentum conservation (the recoil momentum of the atom must be equal and opposite to that of the outgoing photon), $p_\gamma = \frac{E_\gamma}{c}$, and E_R can be much more usefully written as

$$E_R = \frac{1}{2}Mv^2 = \frac{(Mv)^2}{2M} = \frac{p_\gamma^2}{2M} = \frac{E_\gamma^2}{2Mc^2} \tag{3.3}$$

and thus the recoil energy of the nucleus depends intimately on the energy of the γ emitted.

Chemical binding and lattice energies in solids are considerably greater than recoil energies. If the emitting nucleus is bound in a solid, the emission deposits the recoil energy by increasing the vibrational energy of the crystal which can only change by discrete amounts by means of phonons. Thus if the recoil has a lower energy than the lowest available phonon, we have what is called a zero-phonon event. If no energy is lost to recoil of the emitting nucleus, or phonon creation, then, the energy of the emitted γ has the same value as the energy difference between the emitting nucleus' excited and ground states. An emission without phonon excitation or recoil is called a recoilless emission. The same process occurs, in reverse, for a recoilless absorption, also called resonant absorption. The recoilless emission and absorption of a photon is called the Mössbauer effect.

To determine what fraction of events will be recoilless emissions, we define the recoil-free fraction f as the proportion of events that are recoillessly absorbed with respect to the total number of γ emissions. The recoil-free fraction will depend on three factors: the free-atom recoil energy (itself proportional to the energy of the emitted γ), the properties of the solid lattice, and the ambient temperature.

Quantitatively, the forces acting on the nuclear decay are extremely short ranged and thus can be considered independent of the lattice vibration state and vice-versa [44]. The nuclear part of the interactions will depend on the individual nucleus. The recoil free fraction can be reduced to [44]

$$f = \exp\left(-\frac{E_\gamma^2 \langle x^2 \rangle}{(\hbar c)^2}\right). \tag{3.4}$$

where $\langle x^2 \rangle$ represents the mean squared vibrational amplitude.

Using the Debye model, which abandons the idea of a single vibrational frequency and assumes a continuum of oscillator frequencies with a maximum ω_D and follows the distribution formula $N(\omega) = \text{const} \times \omega^2$, we may define a characteristic temperature θ_D, called Debye temperature, as $\hbar\omega_D = k_B\theta_D$ [45]. The average frequency becomes

$$\hbar\overline{\omega} = \frac{3}{4}\hbar\omega_D. \tag{3.5}$$

The upshot of this definition is that it leads to a useful expression for the recoil free fraction:

$$f = \exp\left[-\frac{6E_R}{k_B\theta_D}\left\{\frac{1}{4} + \left(\frac{T}{\theta_D}\right)^2 \int_0^{\theta_D/T} \frac{x\mathrm{d}x}{e^x - 1}\right\}\right]. \tag{3.6}$$

This expression is often written as $f = e^{-2W}$, where W is referred to as the Lamb-Mössbauer factor [46].

First, we remark that a rise in temperature will greatly reduce the recoil free fraction f. Second, a high E_γ also decreases f. Practical Mössbauer transitions are typically in the low keV range. If the energy is any lower than a few keV, sample thickness blocks the transmission. If the energy climbs above ≈100 keV the recoil-free fraction is too low. Thus, a Mössbauer transition with a relatively high E_γ, such as the ^{155}Gd transition used in this study (83.3 keV), requires the emitter material (called "source"), the be cooled to liquid He temperatures in order to increase f, thereby increasing the signal to noise ratio in the acquired data.

3.1.2 Line Shape and Line Width

There is an uncertainty on the energy of the emitted photon which originates from the Heisenberg uncertainty principle

$$\Delta E \Delta t \geq \hbar. \tag{3.7}$$

Since the ground state has an essentially infinite lifetime, its energy uncertainty is zero, however the excited state of the emitter has a mean lifetime, and thus has an energy uncertainty. The energy distribution of the emitted, then absorbed γ has a Lorentzian line shape and the intensity is given by

$$I(\nu) = I_\circ \left[\frac{\Gamma^2}{\Gamma^2 + (\nu - \nu_\circ)^2} \right] \tag{3.8}$$

where $I(\nu)$ is the intensity at some energy value ν, the average energy of the γ is $\nu_\circ$ and Γ is the called the linewidth (not to be confused with the irreducible representation described in Chapter 2).

For an electric dipole Mössbauer transition, such as ^{155}Gd, there is in principle an interference between the nuclear resonance absorption followed by internal conversion and photoelectric absorption. The interference process leads to what is called a dispersive factor in the linewidth, $\left[1 + \frac{2\xi(\nu - \nu_\circ)}{\Gamma}\right]$ that alters the line shape [47]. In ^{155}Gd it is small ($\xi = 0.05(1)$[47]), can be difficult to observe and consequently is often ignored. A demonstration of the difference in a ^{155}Gd Mössbauer spectrum between a line with and without the dispersive correction is shown in Figure 3.1.

The natural linewidth sets a lower bound on Γ, but it can still increase through sample size effects. The linewidth can also appear larger if the electromagnetic interactions are time dependent and change at a rate close to the Larmour frequency (discussed below).

3.1.3 Mössbauer Spectroscopy

Consider now an absorber with a nucleus of the same isotope as the ground state of the emitter (henceforth called "source"). If the absorber is in its ground state, it can

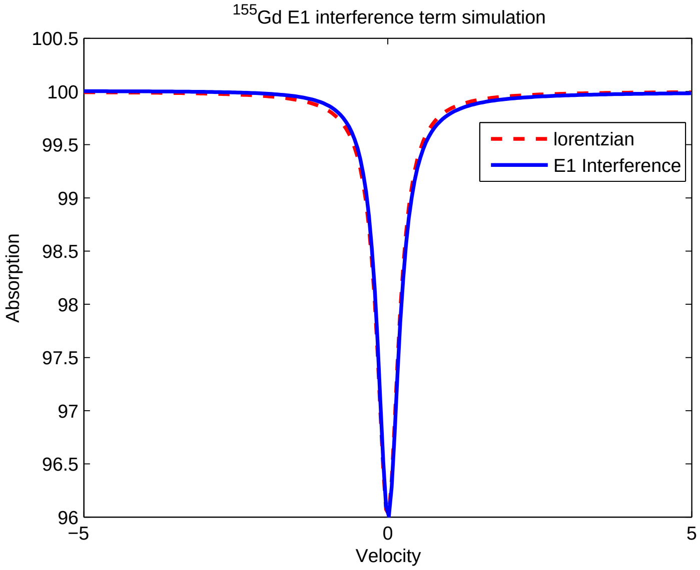

Figure 3.1: Comparison between an absorption line of ^{155}Gd Mössbauer with (blue solid line) and without (red dashed line) the interference correction factor.

then absorb the γ emitted by the source resonantly if the energy of the γ is equal to the separation between the absorber's ground and excited states (shown in part (a) of Figure 3.2). Energy shifts in the excited and ground state levels are intimately linked to the electromagnetic environment of the nucleus and can be directly measured using the Mössbauer effect. The energies involved are of the order of the natural linewidth and can often be smaller, yielding energies on the order of 10^{-8} eV. If there is such a shift in the energy level of the ground and excited states, absorption will not occur since the energy of the emitted γ no longer matches the energy difference between the ground and excited state of the absorber. Since the energy shifts are so small, it is experimentally possible to access these energies by applying a Doppler shift to the γ emitted from the source, compensating for the energy difference and yielding once again absorption as shown in part (b) of Figure 3.2.

The Doppler energy shift ΔE due to an applied velocity v on a γ of energy E_γ

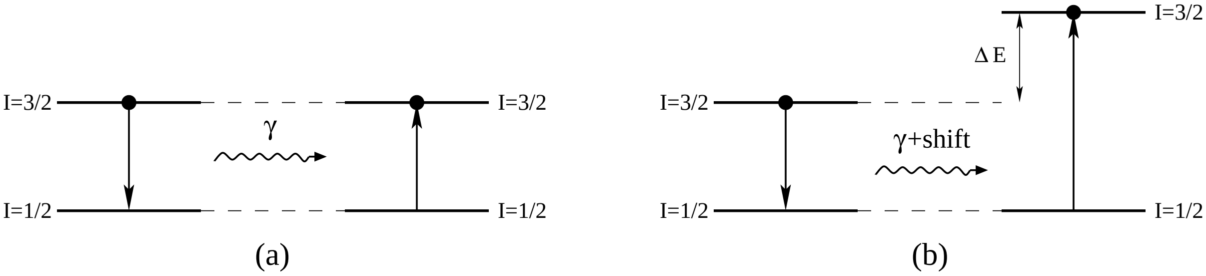

Figure 3.2: Schematic of the emission and absorption process. Part (a) represents the emission of an unshifted γ, and its absorption by a nucleus whose excited to ground state energy difference is identical to the γ energy, and part (b) represents the case when the unshifted γ would fail to be absorbed if not for the Doppler shift which allows for its absorption. Note that the energy is not scaled in these diagrams.

is [48]

$$\Delta E = \frac{v}{c} E_\gamma. \tag{3.9}$$

Consequently, by moving the source forward (to increase the energy of the source photon) and backward (to decrease the energy of the source photon) at different velocities, a range of energies is produced from the source. Each photon then travels through the sample with a probability of being absorbed (corresponding to the recoil-free fraction f) if its energy matches the energy difference between a nucleus' ground and excited states. A Mössbauer spectrum consists of a histogram of events (photons reaching a detector behind the sample, see Figure 3.3) versus source velocity (order of mm/s). A schematic setup is shown in Figure 3.3. This setup yields a Mössbauer spectrum that consists of peaks pointing downward since absorption is measured as a lack of transmission, and is called transmission mode.

The energy modulation required is produced by an electromechanical drive, consisting of a pair of rigidly coupled loudspeakers. The power section of the pair drives the motion while the pick-up section measures the instantaneous velocity which is used to generate the error in a servo loop to maintain velocity accuracy. The velocity

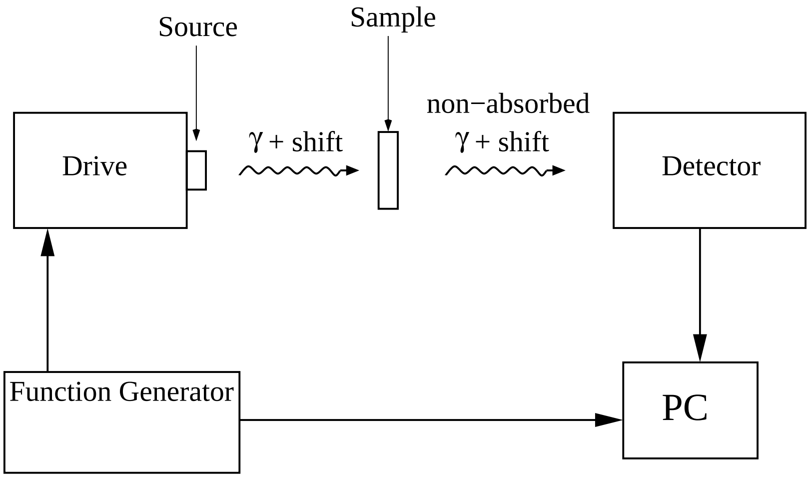

Figure 3.3: Sketch of a typical Mössbauer experiment.

is controlled by a digital function generator. Typically the velocity waveform is chosen to be triangular, meaning that the function generator sweeps linearly through the velocities back and forth. This choice establishes a constant velocity spacing between channels. Using this method leads to an infinite derivative in the velocity sweep when reaching maximum positive or maximum negative velocities, causing a large deviation from strict linearity. This occurs at the outer edges of the spectrum and consequently, does not generally impact the quality of the data. Another, less common, choice is to sweep across the velocities sinusoidally. This has the disadvantage that the drive spends most of its time at the end velocities, and thus distorts the visual aspect of the spectrum, but it spares the drive the large derivative when it changes direction (discussed below).

3.1.4 Hyperfine Interactions

Inside the atom, the nuclear moment can interact magnetically with the electronic moment. Two types of magnetic interaction are important. The first is a magnetic dipole interaction where the nuclear moment interacts with the electronic moment and vanishes for spherically symmetric orbitals. The second interaction vanishes for all but spherically symmetric orbitals. It consists of the energy cost of having an electron in the finite nuclear volume and is called the Fermi contact interaction. The dipole and Fermi contact interactions are quite weak and lead to very small nuclear energy level splitting. These are called hyperfine interactions.

Hyperfine interactions are responsible for connecting the nuclear energy levels to the properties of the electrons on the atom and hence the properties of the solid being studied. If moments in the solid order, a non-zero average field is observed at the probe nuclei and can be detected via Mössbauer spectroscopy.

The energy levels of the absorbing nucleus' ground and excited states depend on the interaction Hamiltonian [49],

$$\mathcal{H} = \mathcal{H}_C + \mathcal{H}_M + \mathcal{H}_Q + \ldots \tag{3.10}$$

$\mathcal{H}_C$ represents the Coulombic interactions between the nucleus and the electrons; $\mathcal{H}_M$ the magnetic dipole interactions; $\mathcal{H}_Q$ the electric quadrupole interactions. All higher order terms are ignored [49].

The $\mathcal{H}_C$ term, called isomer shift, is a measure of the difference in electron density and mean square radius of the charge distribution at the nucleus between the source and absorber. The effect is due to the finite size of the nucleus coupled with the non-zero probability density of s-electrons at the nucleus. The isomer shift is observed in a Mössbauer spectrum as a shift toward higher or lower velocity. It does not itself lift the energy level degeneracy in the excited or ground state, nor does it alter the energy level splitting within the excited and ground states caused by other terms.

The $\mathcal{H}_M$ and $\mathcal{H}_Q$ are the terms that can lift the energy level degeneracy of the excited and ground states. An example of the energy level degeneracy lifting and its effect on a ^{119}Sn Mössbauer spectrum is shown in Figure 3.4. The line position in the spectrum is the shift in energy between the excited state to ground state energy of the absorber nucleus with respect to the excited state to ground state energy of the emitter nucleus. The left of Figure 3.4 is the spectrum obtained if no shift of splitting occurs. The right of Figure 3.4 is the spectrum if both the excited and ground states are split due to a magnetic field but with no isomer shift. It is important to note that the excited state and the ground state have often different total spins and different nuclear quadrupole and magnetic dipole moments, and consequently the energy splittings will be different. It is also important to note that the hyperfine fields at the nucleus do not change between the ground and excited states.

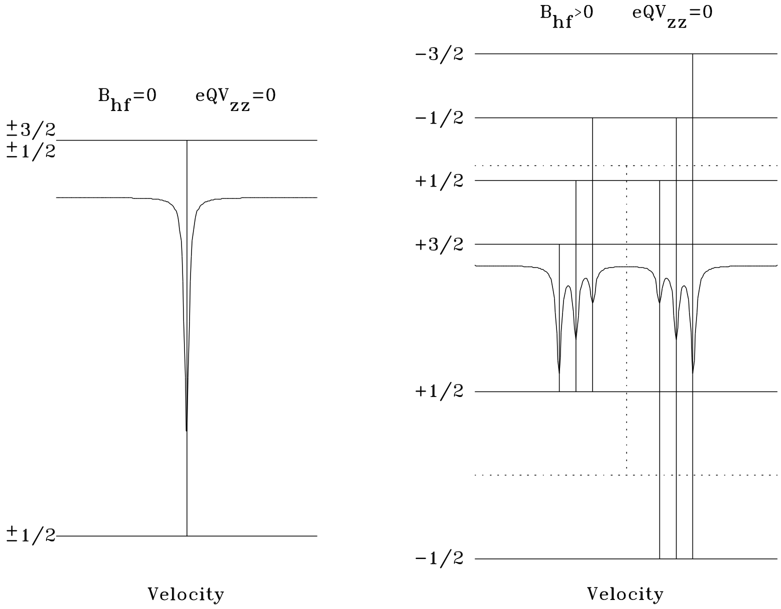

Figure 3.4: Example of the lifting of the energy level degeneracy due to a magnetic field B_{hf}. When the levels are degenerate, the ^{119}Sn Mössbauer spectrum consists of a single absorption line (left), and when the levels are split a multiline pattern is observed (right). The dotted lines on the right pattern indicate the zero velocity (vertical) and the reference energy of the unsplit levels (horizontal).

Typical velocities used for ^{119}Sn Mössbauer spectroscopy are between 10 and 15 mm/s (for ^{119}Sn, 1 mm/s $\sim 8 \times 10^{-8}$ eV) and the maximal fields observed are $\sim$8 T. For ^{155}Gd Mössbauer spectroscopy typical velocities are $\sim$5 mm/s (for ^{155}Gd, 1 mm/s $\sim 3 \times 10^{-7}$ eV) and the maximal fields observed are $\sim$30 T.

3.1.5 Magnetic Dipole Interactions

For a nucleus in a state with a gyromagnetic ratio g, and subject to a static hyperfine magnetic field $\mathbf{B}$, $\mathcal{H}_M$ can written as [50]:

$$\mathcal{H}_M = -g\mu_N \mathbf{B} \cdot \hat{\mathbf{I}} \tag{3.11}$$

where $\hat{\mathbf{I}}$ is the total spin operator and μ_N is the nuclear magneton. For simplicity, we can chose the z-axis to be the direction of the field and get

$$\mathcal{H}_M = -g\mu_N B\hat{I}_z \tag{3.12}$$

where B is the magnitude of the field and $\hat{I}_z$ is the z component of the angular momentum operator. For both the excited and ground states, the $|m\rangle$ states are eigenstates of this Hamiltonian and thus the eigenvalues can be found trivially,

$$E_M = -g\mu_N Bm \tag{3.13}$$

3.1.6 Electric Quadrupole Interactions

Electric quadrupole interactions arise from the electric field gradient, a 3×3 traceless tensor $V_{ij} = (\partial^2 V/\partial x_i \partial x_j)(x_i, x_j = x, y, z)$, which is a measure of the deviation from spherical symmetry of the electronic charge distribution around the nucleus. The coordinate system can always be chosen such that the tensor is diagonal and traditionally the z-axis is chosen to be along the largest component of V_{ij}. V_{zz} is called the principal axis of the electric field gradient. Since the tensor is traceless, $V_{xx} + V_{yy} + V_{zz} = 0$, and only two parameters are required to specify the tensor completely: the asymmetry parameter $\eta = \frac{V_{xx}-V_{yy}}{V_{zz}}$, and the principal axis value. Using the convention $|V_{zz}| \geq |V_{yy}| \geq |V_{xx}|$ ensures that $1 \geq \eta \geq 0$. For a nucleus with an electric quadrupole moment Q, spin I, subject to an electric field gradient whose principal axis value is V_{zz}, with an asymmetry η the Hamiltonian can be written as [51]:

$$\mathcal{H}_Q = \frac{eQV_{zz}}{4I(2I-1)}\left[3\hat{I}_z^2 - I(I+1) + \frac{\eta}{2}(\hat{I}_+^2 + \hat{I}_-^2)\right] \tag{3.14}$$

where e represents the charge of the proton and $\hat{I}_+$ and $\hat{I}_-$ are the standard spin raising and lowering operators. If $\eta = 0$ the $|m\rangle$ states are again energy eigenstates, and the problem is greatly simplified. We note also that $\mathcal{H}_Q$ will yield a degeneracy in its eigenvalues and only $|m|$ will change the energy.

3.1.7 Combined Interactions

The next natural step is to combine the magnetic-dipole and electric-quadrupole interactions. A priori there is no physical reason for which V_{zz} and B_{hf} should be parallel, and we are required to choose a non-trivial quantization axis. For simplicity we have chosen V_{zz} and the schematic setup is shown in Figure 3.5.

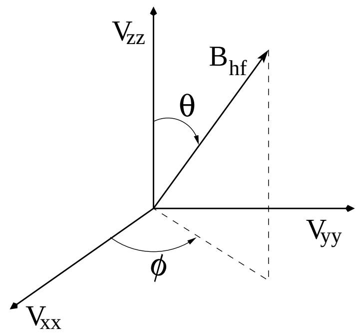

Figure 3.5: Schematic of the ϕ and θ angles, V_{zz} and B_{hf}.

The Hamiltonian operator for this system becomes [51]

$$\begin{aligned} \mathcal{H} &= \frac{eQV_{zz}}{4I(2I-1)}\left[3\hat{I}_z^2 - I(I+1) + \frac{\eta}{2}(\hat{I}_+^2 + \hat{I}_-^2)\right] && (3.15)\\ &- g\mu_N B_{hf}\left[\hat{I}_z\cos\theta + \frac{1}{2}(\hat{I}_+e^{-i\phi} + \hat{I}_-e^{i\phi})\sin\theta\right] && (3.16)\end{aligned}$$

where $\mathcal{H}_M$ needs to be rotated from the z-axis and is written following the convention of Figure 3.5.

As discussed above, the energy shift detected by Mössbauer spectroscopy is the difference between the energies of the excited state Hamiltonian E_{n_e} and the ground state Hamiltonian E_{n_g}, with the isomer shift added to the difference. Note that the original energy of the source γ does not directly factor into this calculation: we are measuring the difference in the *deviation* from that energy between the source and absorber. The result is completely general for all values of the hyperfine parameters. So for a given transition between the levels E_{n_g} of the ground state and E_{n_e} of the excited state, we obtain

$$E_n(e \rightarrow g) = E_{n_e} - E_{n_g} + IS \tag{3.17}$$

where IS is the isomer shift.

The intensity of the absorption will depend on the appropriate Clebsch-Gordan coefficients $\langle I_g \mathbf{L} m_g m | I_e m_e \rangle$, and the eigenvector matrix elements $\langle m_e | n_e \rangle$. In both Mössbauer isotopes used in this study, ^{119}Sn and ^{155}Gd Mössbauer, $\mathbf{L} = 1$. The line intensity for a transition from a ground state g to an excited state e in a polycrystalline material can be written as

$$I_{e \rightarrow g} = |a(\mathbf{L}, 1)|^2 + |a(\mathbf{L}, 0)|^2 + |a(\mathbf{L}, -1)|^2 \tag{3.18}$$

where

$$a(\mathbf{L}, m) = \sum_{m_e - m_g = m} \langle m_e | n_e \rangle \langle m_g | n_g \rangle^* \langle I_g \mathbf{L} m_g m | I_e m_e \rangle \tag{3.19}$$

where $\mathbf{L} = 1$ for the ^{119}Sn and ^{155}Gd transitions used in this study.

It is important to consider exactly to what Mössbauer spectroscopy is sensitive. First considering only electric quadrupole interactions, Figure 3.6 illustrates how ^{170}Yb Mössbauer (left) can determine unambiguously the sign of V_{zz} since the left and the right of the pattern are different, whereas ^{119}Sn Mössbauer cannot, since the pattern is symmetric. ^{155}Gd Mössbauer suffers from the same symmetry limitation since the ground state quadrupole moment is so much larger than the excited state quadrupole moment, yielding an essentially symmetric pattern as well. Moreover, for both ^{119}Sn and ^{155}Gd Mössbauer spectroscopy, the value of η cannot be determined from a non-magnetic pattern. Thus, for both Mössbauer isotopes used in this study, ^{119}Sn and ^{155}Gd, the determination of the sign of V_{zz} and the size of η will require data in the magnetic phase.

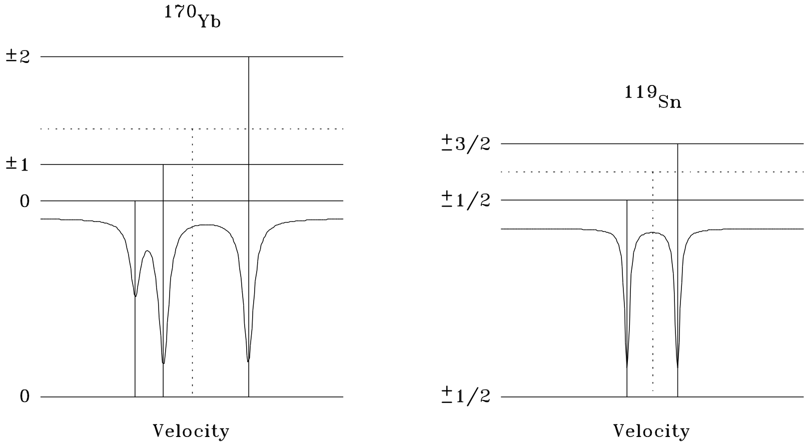

Figure 3.6: Simulated electric quadrupole spectra for ^{170}Yb Mössbauer (left) and ^{119}Sn Mössbauer (right). The energy splitting for the excited state (above the spectrum) and the ground state (below the spectrum) along with the m_z values for each state are also shown. The dotted lines indicate the zero velocity (vertical) and the reference energy of the unsplit levels (horizontal).

The presence of only a magnetic field in a ^{119}Sn Mössbauer spectrum, as the left of Figure 3.7 shows, also yields a symmetric pattern. If we have combined interactions however, as seen on the right of Figure 3.7, for a positive V_{zz} the pattern is no longer symmetric.

A subtle point needs to be made when it comes to the sign of the magnetic field. The left of Figure 3.8 is the spectrum obtained by setting the field to be negative while V_{zz} is positive. The pattern is identical to the right of Figure 3.7, even though the energy levels have changed, since the change is equivalent to a simple relabeling of the m_z states. A negative V_{zz} however, shown on the right of Figure 3.8 yields a pattern that is inverted from the positive V_{zz} case. The behaviour seen in Figures 3.7 and 3.8

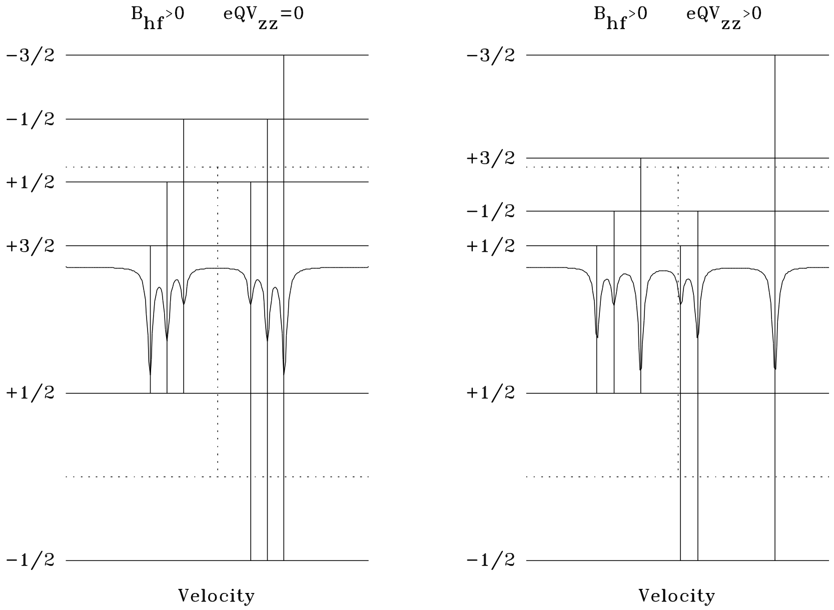

Figure 3.7: Left: Simulated magnetic ^{119}Sn Mössbauer spectrum. Right: Simulated combined magnetic and quadrupole interactions ^{119}Sn Mössbauer spectrum with positive field and V_{zz}. The energy splitting for the excited state (above the spectrum) and the ground state (below the spectrum) along with the m_z values for each state are also shown.

is seen even in the more complex cases when the m_z states are no longer eigenstates of the Hamiltonian, and the result that Mössbauer spectroscopy is insensitive to the sign of B_{hf} is completely general.

Finally, it is important to qualify what is meant by a static hyperfine field. Insofar as Mössbauer spectroscopy is concerned, if the field fluctuates much faster than the Larmor precession frequency, it is equivalent to a static field which has a time averaged value of the fluctuating field. Since magnon frequencies (THz) are far above typical Larmor precession frequencies (MHz), for cases of simple magnetic ordering we expect the hyperfine magnetic field to have a temperature dependence that follows the magnetization of the molecular field model described in Section 2.1.3 and shown in Figure 2.2.

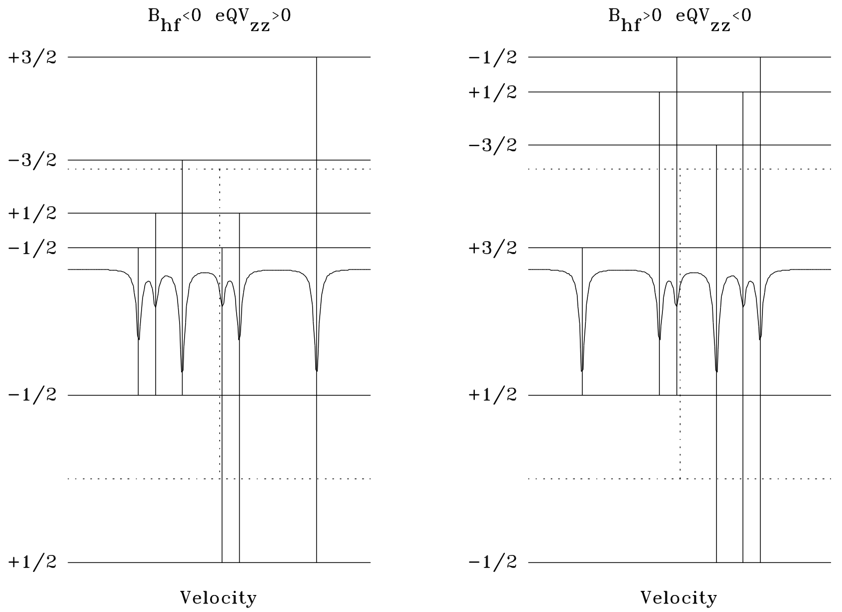

Figure 3.8: Left: Simulated combined magnetic and quadrupole interactions ^{119}Sn Mössbauer spectrum with negative field and positive V_{zz}. Right: Simulated combined magnetic and quadrupole interactions ^{119}Sn Mössbauer spectrum with positive field and negative V_{zz}. The energy splitting for the excited state (above the spectrum) and the ground state (below the spectrum) along with the m_z values for each state are also shown.

3.1.8 Slow Moment Relaxation

Thus far, the field at the nucleus of a Mössbauer isotope has been considered static. This assumption is valid as long as the field fluctuates at frequencies far above (or far below) the Larmor precession frequency, in which case the Mössbauer spectrum exhibits a single, time averaged field.

Mössbauer spectroscopy will also be sensitive to hyperfine magnetic fields which fluctuate at a frequency close to the Larmor precession frequency, but the spectra will exhibit different characteristics. Relaxation spectra are characterized by broadening of high and low velocity lines as the field goes from static to fluctuating. As the frequency grows, the outer lines continue to broaden and decrease in intensity, while a sharp center component grows in intensity. When the frequency far exceeds the Larmor frequency, the magnetic field essentially averages to zero and only the non-magnetic interactions (electric monopole and electric quadrupole) influence the spectrum.

The spectra in the dynamic regime are fitted using the Blume and Tjon up/down model, consisting of a static electric field gradient with a randomly fluctuating magnetic field which takes on values $+B_{hf}$ and $-B_{hf}$ along the electric field gradient axis [52]. The lineshape $W(v)$ can be written as [52]

$$W(v) = \frac{2}{\Gamma}\mathrm{Re}\sum_{m_g m_e}\frac{1}{4}|\left\langle I_g m_g\right| H \left|I_e m_e\right\rangle|^2 \sum_{ij} p_i \left\langle j\right| (p - \mathbf{W} - i\alpha\mathbf{F})^{-1} \left|i\right\rangle \tag{3.20}$$

where

$$p = -i\left(v - Q\left(3m_e^2 - \frac{15}{4}\right)\right) + \frac{1}{2}\Gamma \tag{3.21}$$

m_e and m_g are the excited and ground state z components of the spin, $\mathbf{W}$ is the matrix of transition probabilities, $\mathbf{F}$ is a diagonal matrix whose entries are the allowed values of the sign of the hyperfine magnetic field, $\alpha = (g_g m_g - g_e m_e)\mu_N B_{hf}$, p_i is the probability that the initial state occurs. The inverse of the $(p - \mathbf{W} - i\alpha\mathbf{F})$ matrix is computed numerically. $|\left\langle I_g m_g\right| H \left|I_e m_e\right\rangle|^2$ represents the intensity of each absorption line, which is identical to the intensities in the static case.

Both the static and relaxation models are valid for all Mössbauer isotopes, however since each has its own electric quadrupole and magnetic dipole moments, the character of the spectra obtained experimentally will depend intimately on which isotope is being used.

3.1.9 Spectral Areas and Subspectra

An important property of Mössbauer spectra is that they are phase quantitative. If half the absorber nuclei are in one environment, and the other half in another, the spectrum will consist of the sum of the individual spectra (called subspectra) with the subspectral areas weighted by the relative populations. Note that in certain cases, for example in $\mathrm{YbMn_2Si_{2-x}Ge_x}$ [53], a complication of this property occurs when the different sites in the structure have different Debye temperatures which may lead to a misinterpretation of the data, however this difficulty is not present in the materials studied here.

The phase quantitative nature of Mössbauer spectroscopy can allow for identification of the origin of the signal. Since there are twice as many Gd-4e sites as Gd-2d sites in $\mathrm{Gd_3Cu_4Ge_4}$ for example, we expect to observe either a single spectrum, if the environment around both sites is identical, or two subspectra with a 2:1 area ratio if the environments are different.

3.1.10 ^{155}Gd Mössbauer Spectroscopy

The decay scheme for ^{155}Eu is shown in Figure 3.9. The ^{155}Gd Mössbauer transition consists of the 86.3 keV γ from the $\frac{5}{2}$ level to the $\frac{3}{2}$ ground state. The half-life of the intermediate state leads to a minimal (called natural) linewidth of 0.257 mm/s [54].

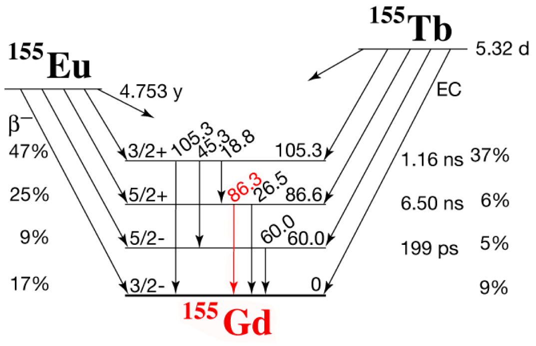

Figure 3.9: ^{155}Eu decay scheme with the 86.3 keV Mössbauer transition from the $\frac{5}{2}$ level to the $\frac{3}{2}$ ground state labeled in red.

Such a high energy requires the source to be cooled to liquid He temperatures in order to get an experimentally reasonable signal. Traditionally, a Mössbauer spectrometer is set up such that the drive operates on a horizontal axis. The environment of the sample needs only to be designed such that the source is close ($\sim$ 5 cm) to the sample and the detector as well. This experimental setup is used for the ^{119}Sn Mössbauer spectroscopy experiments. In the case of ^{155}Gd Mössbauer spectroscopy however, both the source and the sample need to be kept cold (1.5 to 50 K) and they are both inserted into the cryostat using a vertical setup, where they are subjected to the vapour of boiling liquid He and the temperature is controlled with a heater. The He gas is pumped on in order to reach temperatures below the boiling point of liquid He. A schematic of the experimental setup is shown in Figure 3.10.

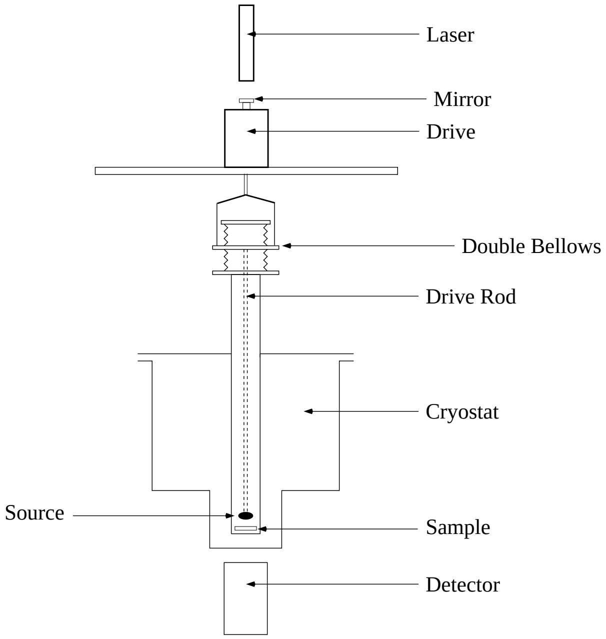

Figure 3.10: Schematic of the vertical mode transmission Mössbauer spectroscopy experimental setup. A more detailed schematic of the laser calibration setup can be found in [55].

The vertical spectrometer setup has been outfitted with a laser, and the calibration of the velocity is accomplished through interferometry. A laser points to a mirror attached to the back of the vertical drive and a beam splitter picks up the interference pattern, a strategy described in detail by Biscar *et al.* [55]. The size of the cryostat puts a limit on how close the drive can be to the cool sample space, and this limit is of the order of a meter. The drive must therefore be attached to a long rod that brings the source to the desired distance from the sample, introducing a lag in velocity that is non-negligible, but easily corrected for. The velocities were cross-checked against a ^{57}Co/α-Fe experiment at room temperature and it was determined that the velocity of the source is different by a factor of 0.95 than the drive velocity. Another side effect of a long drive rod is that mechanical stress becomes an issue when the triangular sweeping reaches maximum and minimum velocities goes through an infinite derivative. This is avoided by using a sinusoidal sweep in velocity.

The thermometer used for all ^{155}Gd Mössbauer spectroscopy experiments is a Cernox (ceramic nitride oxide) resistor produced and calibrated by Lakeshore Cryotronics from 0.3 to 100 K. The calibration sets the largest uncertainty in the measured temperature to be 1.73 mK.

To measure the transmitted radiation, a high-purity Ge detector, kept at liquid nitrogen temperature throughout the experiment, and subject to a bias voltage of 3.5 kV is used. The detector in this case is designed to have high energy resolution and high count-rate ($\sim 3 \times 10^4$ counts/sec) capabilities. The resolution necessity comes from the fact that most non-commercially available radioisotopes have the drawback that activation, even of isotopically separated materials, inevitably leads to the emission of unwanted radiation. The high energy of the γ in this case also causes fluorescence x-rays to be detected. The high energy resolution allows the correct γ to be isolated and the others can easily be tuned out.

The source was prepared by arc melting isotopically separated ^{154}Sm metal with Pd to form ^{154}SmPd$_3$. The powdered ^{154}SmPd$_3$ (488 mg) was mixed with Al powder (108 mg) for binding. The absorption of neutrons by the ^{154}Sm lead to ^{155}Sm which decays to ^{155}Eu.

The nuclear parameters used in the excited and ground state Hamiltonians are:

$$Q_g = -1.30(2)\text{ b} \qquad g_g = -0.2591(5)\ \mu_\mathrm{N}$$

$$Q_e = -0.111(7)\text{ b} \qquad g_e = -0.525(2)\ \mu_\mathrm{N}$$

where μ_N is the nuclear magneton. The values are taken from Raghavan [56] and reflect the latest accepted values.

The small size of Q_e with respect to Q_g leads to a quadrupole split spectrum that appears as a slightly broadened doublet, as can be seen in the $Gd_2Sn_2O_7$ spectrum in Figure 3.11. Authors often quote the splitting in mm/s between the two lines, Δ, however it is important to note that the Q_e value has an influence on the splitting. For ^{57}Fe or ^{119}Sn Mössbauer it is customary to quote Δ since in those cases it is strictly equal to $\frac{eQ_eV_{zz}}{2}\sqrt{\left(1+\frac{\eta^2}{3}\right)}$, however for ^{155}Gd Mössbauer using $\frac{eQ_eV_{zz}}{2}\sqrt{\left(1+\frac{\eta^2}{3}\right)}$ interchangeably with Δ leads to a slight but measurable discrepancy (about 4%).

The hyperfine magnetic field observed by ^{155}Gd Mössbauer spectroscopy can be written as [57]

$$B_{hf} = B_{4f} + B_{cp} + B_p + B_{nn}. \tag{3.22}$$

B_{4f} is the contribution to the field due to the incomplete $4f$ shell. B_{cp} is the core polarization field which comes from the deformation of the inner electronic shells by the $4f$ shell. The spin of the parent Gd^{3+} will lead to a conduction electron polarization field, B_p. Finally, a transferred field from the magnetic nearest neighbours, mediated by conduction electron polarization, B_{nn} also contributes to the observed hyperfine field. The $B_{4f} + B_{cp}$ contribution will be antiparallel to the parent Gd^{3+} moment, and the B_{nn} contribution is assumed to be a vector sum of the neighbouring moments. The net effect remains that the field observed at the ^{155}Gd nucleus follows the trend laid out at the end of Section 3.1.7: the field follows the same trend as the magnetization with respect to temperature, shown in Figure 2.2.

In order to verify the functionality of the source, $Gd_2Sn_2O_7$ was measured as a quadrupole standard and $GdFe_2$ as magnetic standard with sample areal density of ~ 1.7 mg/mm^2. We obtained a splitting between the two lines of 3.97(1) for $Gd_2Sn_2O_7$, quite close to the value of 3.93(1) mm/s obtained by Cashion *et al.* [58]. We obtain a value of 45.5(2) T in agreement with the 45.0(15) T value obtained by Cashion *et al.* [58]. The linewidth for both standards was 0.341(5) mm/s, larger than the natural linewidth but typical for an experimental measurement. A plot of the reference spectra is shown in Figure 3.11.

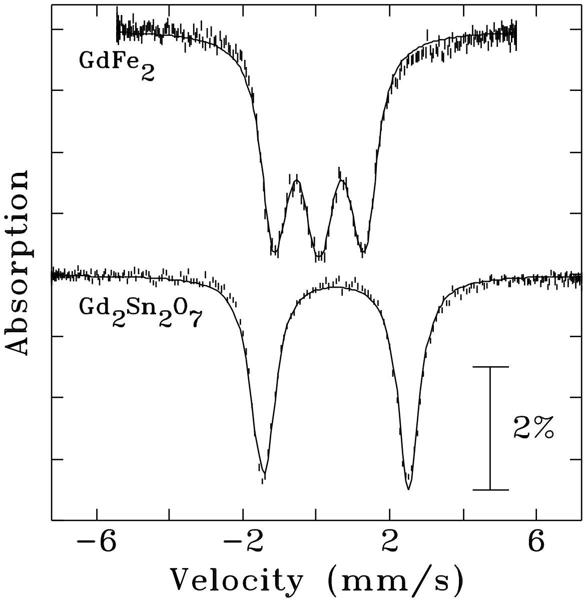

Figure 3.11: ^{155}Gd Mössbauer spectra for the $Gd_2Sn_2O_7$ and $GdFe_2$ reference samples acquired at 5 K.

3.1.11 ^{119}Sn Mössbauer Spectroscopy

The availability of a Mössbauer transition in Sn allows it to contribute to the study of the $R_3T_4Sn_4$ system. ^{119}Sn Mössbauer spectroscopy is particularly useful because it yields directly comparable data for different rare earths, and the relatively low γ energy (23.875 keV) [59] allows for measurements to be taken up to room temperature if necessary. The decay scheme for ^{119m}Sn is shown in Figure 3.12. The half-life of the intermediate state yields a natural linewidth of 0.313 mm/s [54]. The transmitted γ rays are measured with a NaI scintillation detector. Pd has a photoelectric absorption of 24.35 keV and a 25 μm Pd foil is used to absorb the Sn K_α x-rays (25.04 and 25.27 keV) [59] also emitted by the 0.4 GBq ^{119m}Sn $CaSnO_3$ source.

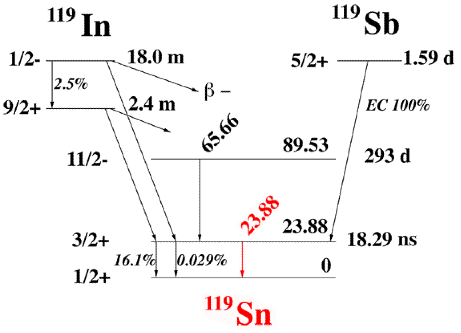

Figure 3.12: ^{119m}Sn decay scheme with the 23.88 keV Mössbauer transition from the $\frac{3}{2}$ level to the $\frac{1}{2}$+ ground state labeled in red.

The nuclear parameters for the ^{119}Sn Mössbauer transition are:

$$Q_g = 0 \text{ b} \qquad g_g = -0.2591(5)\ \mu_{\mathrm{N}}$$

$$Q_e = -0.111(7) \text{ b} \qquad g_e = -0.525(2)\ \mu_{\mathrm{N}}$$

where the zero ground state quadrupole moment leads to the quadrupole doublet for which the splitting is strictly equal to $\frac{eQ_eV_{zz}}{2}\sqrt{\left(1+\frac{\eta^2}{3}\right)}$, often quoted as Δ. The value of η can only be determined from magnetic spectra.

Although Sn is non-magnetic, a ^{119}Sn Mössbauer spectrum can still exhibit a magnetic splitting due to a transferred hyperfine field from neighbouring magnetic atoms. As described in section 2.2, each Sn site in the $Gd_3Cu_4Ge_4$-type structure has rare earth neighbours from both rare earth sublattices which lead to the observation of a magnetic field at the Sn nuclei when the rare earth moments order. There are two main contributions to the transferred hyperfine field observed at the Sn nuclei. First, the polarization of conduction electrons induces a spin imbalance of the 5 s

electrons at the Sn nucleus, which depends only on the magnitude and direction of neighbouring magnetic moments. This is termed the Fermi contact field [60, 61]. Second, the hybridization of the valence p electrons leads to a non-spherical spin density which in turn leads to a dipolar field. This dipolar field depends on both the magnitude of the neighbouring moments and the relative orientations of the moments and their connecting bonds [60, 61]. There is a third interaction arising spin-orbit coupling which leads to a polarization of the Sn p states, which in turn induces an polarization, creating an orbital field. This third interaction however, is considered small and will not be included here [60, 61].

The expression for the transferred field, first expressed in the case of $MnSn_2$ [62], from N nearest neighbours with moments $\vec{\mu_i}$ and unit vectors $\vec{u_i}$ directed along the Sn-rare earth bonds is [60]:

$$\mathbf{B}_{hf} = \left[A_p \sum_{i=1}^{N} \vec{u}_i \left(\vec{\mu_i} \cdot \vec{u}_i\right) - \frac{A_p}{3} \sum_{i=1}^{N} \vec{\mu_i} \right] + A_s \sum_{i=1}^{N} \vec{\mu_i} \tag{3.23}$$

where A_p and A_s are constants that represent the strengths of the dipolar field and Fermi contact field respectively. The first term in brackets of equation 3.23 is referred to as the anisotropic term since the relative location of the neighbouring moment has an influence on the transferred field. The second term is referred to as the isotropic term. It is a simple vector sum of the neighbouring moments: the transferred field does not depend on their location relative to the probe Sn atom. It was subsequently shown that there is an anisotropic contribution to the transferred hyperfine field from the rare earth nearest neighbours and its magnitude is similar to the Mn contribution [61].

^{119}Sn Mössbauer spectra are collected by mounting the sample in the same cryostat setup shown in Figure 3.10. The source however, does not require cooling and is not mounted with the sample. Instead, the source and drive are mounted outside the cryostat and the photon transmission occurs horizontally through windows on the cryostat around the sample space. Calibration of the velocity is achieved with a ^{57}Co

Mass	$1.674928(1)\times10^{-24}$ kg
Charge	0 C
Spin	$\frac{1}{2}$
Magnetic moment (μ_{N})	-1.9130427(5) μ_{N}

Table 3.1: Fundamental properties of the neutron [63].

source and a α-Fe calibration foil.

3.2 Neutron Diffraction

The usefulness of thermal neutrons in the study of crystalline and magnetic structure stems from the fundamental properties listed in Table 3.1 [63]. The mass of the neutron leads to a de Broglie wavelength for thermal neutrons (energy ∼0.025 eV) of the order of interatomic distances in crystals and consequently yields structural information. The magnetic moment of the neutron leads to interactions with the magnetic moment of the atom, and thus yields information about the magnetic structure of magnetic materials. Finally, the lack of charge means that the neutrons will be able to penetrate deeply into the material and closely approach the nucleus.

3.2.1 Nuclear Scattering

When a plane wave of neutrons $\Psi = e^{i\kappa z}$ is incident on a nucleus (where the wave vector is along the z-axis), the spherically symmetrical scattered wave function will have the form $\Psi = -\frac{b}{r}e^{i\kappa r}$ where b is a complex ($b = b' - ib''$), isotope specific quantity called the scattering length. The resultant neutron wave function will be given by [64]

$$\Psi = e^{i\kappa z} - \frac{b}{r}e^{i\kappa r} \tag{3.24}$$

If we have an assembly of nuclei, as in a crystal, the resultant wave function after scattering the assembly of atoms will be [64]

$$\Psi = e^{i\kappa z} - \sum_{\rho} \frac{b}{r} e^{i\kappa r} e^{i\vec{\rho}\cdot(\vec{\kappa}-\vec{\kappa'})} \tag{3.25}$$

where $\vec{\rho}$ is the vector from the origin to the nucleus and $\vec{\kappa}$ and $\vec{\kappa'}$ are the wave vectors of the neutrons before and after scattering. The $e^{i\vec{\rho}\cdot(\vec{\kappa}-\vec{\kappa'})}$ factor acquired results from phase difference introduced by the different nuclei in the crystal. $e^{i\vec{\rho}\cdot(\vec{\kappa}-\vec{\kappa'})}$ can be more usefully written as [64]

$$-\sum_{\rho} b_{\rho} \exp\left[2\pi i \left(h\frac{x}{a} + k\frac{y}{b} + l\frac{z}{c}\right)\right] \tag{3.26}$$

where x, y and z are the Cartesian coordinates of the nucleus, a, b and c are the dimensions of the crystallographic unit cell, and h, k and l are the Miller indices appropriate to the particular direction $\vec{\kappa} - \vec{\kappa'}$. The differential cross-section in this particular direction, $\frac{d\sigma}{d\Omega}$, will be [65]

$$\frac{d\sigma}{d\Omega} \propto \left| \sum_{\rho} b_{\rho} \exp\left[2\pi i \left(h\frac{x}{a} + k\frac{y}{b} + l\frac{z}{c}\right)\right] \right|^2 = |\mathcal{F}_{hkl}|^2 \tag{3.27}$$

$\mathcal{F}_{hkl}$, called structure factor, leads to a simple computation of allowed reflections and results for all crystallographic space groups have been tabulated. The intensity of the peaks will depend on the scattering length of each nucleus, b_{ρ}, contributing to a given reflection.

It is useful at this point to contrast neutron scattering and x-ray scattering since the processes are up to this point very similar. First, within a factor of 2 or 3, most atoms scatter neutrons equally well, and consequently light elements can be readily detected in the presence of heavier elements. Second, the scattering lengths do not depend on the atomic number, meaning that the difference in scattering between two periodic table neighbours can often be experimentally resolved, which is not possible with x-ray diffraction. Finally, since the dimensions of the nucleus are so much smaller than the wavelength, the angular dependence of the scattering, or ‘form factor', is constant, leading to very strong high-angle peaks, again very much unlike x-ray diffraction.

The neutron has a spin **s** and the nucleus has a spin **I** such that the scattering length will in general be spin dependent [66]:

$$b = b_c + \frac{2b_i}{\sqrt{I(I+1)}}\mathbf{s}\cdot\mathbf{I} \tag{3.28}$$

where b_c is the coherent scattering length and b_i the incoherent scattering length. In all measurements presented here the neutron beam is unpolarized, and thus the coherent and incoherent scattering cross sections are given by

$$\sigma_c = 4\pi|b_c|^2 \tag{3.29}$$

and,

$$\sigma_i = 4\pi|b_i|^2 \tag{3.30}$$

and the absorption cross section is given by [66]

$$\sigma_a = 2\lambda b''_c \tag{3.31}$$

where b''_c is the complex part of the coherent scattering length b_c, and λ is the wavelength of the incident neutron. For most nuclei, b''_c is negligible, however for natural Sm and Gd it is substantial and must be taken into account. The values relevant to the data presented in this work are given in Table 3.2. For samples containing Cu, Ag, Sn, Pr, Nd, Tb, Ho, and even Dy, a cylindrical sample holder is convenient and yields excellent results. Gd and Sm based compounds pose an important absorption problem and are discussed separately below.

3.2.2 Magnetic Neutron Diffraction

The principal use of neutron diffraction in the present work is to determine magnetic structures and confirm magnetic ordering temperatures. The situation is very similar

Element	b_c (fm)	b_i (fm)	σ_a (barn)
Cu	7.718(4)		3.78(2)
Ag	5.922(7)		63.3(4)
Sn	6.225(2)		0.626(9)
Pr	4.58(5)	-0.35(3)	11.5(3)
Nd	7.69(5)		50.5(1.2)
Sm	0.80(2)-1.65(2)i		5922.(56.)
Gd	6.5(5)-13.82(3)i		49700.(125.)
Tb	7.38(3)	7.38(3)	23.4(4)
Dy	16.9(2)-0.276(4)i		994.(13.)
Ho	8.01(8)	-1.70(8)	64.7(1.2)

Table 3.2: Neutron scattering parameters for elements Cu, Ag, Sn, Pr, Nd, Sm, Gd, Tb, Dy and Ho. Note that the absorption cross section is neutron wavelength dependent and the value presented here is for 1.8 Å. [66].

to nuclear scattering with the important difference that the scattering length for magnetic scattering is a vector $p\mathbf{q}$, where [67]

$$\mathbf{q} = \hat{\varepsilon}(\hat{\varepsilon} \cdot \mathbf{K}) - \mathbf{K} \tag{3.32}$$

where the unit vector $\hat{\varepsilon}$ is orthogonal to the effective reflecting plane, $\mathbf{K}$, which is along the atomic magnetic moment direction, and [68]

$$p = \frac{e^2\gamma}{2mc^2} g\mathbf{J}f \tag{3.33}$$

where m is the electron mass, e is the electron charge, c is the velocity of light, g is the Landé g-factor, $\mathbf{J}$ is the total angular momentum and f is the magnetic form factor (discussed below). A schematic of a magnetic scattering event is show in Figure 3.13.

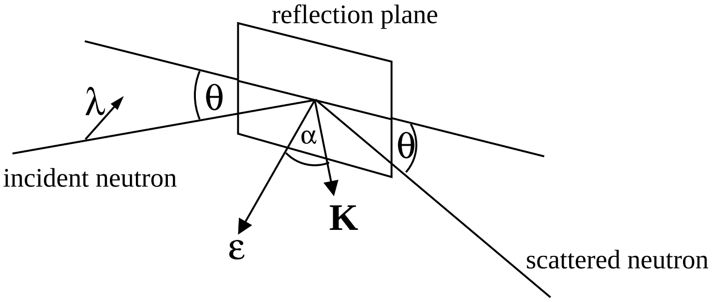

Figure 3.13: Magnetic scattering diagram identifying the vectors ε, λ and $\mathbf{K}$. Taken from Bacon [69].

When the magnetic moments in a structure are not randomly oriented, and instead are fixed to a specific crystallographic direction the differential cross-section can be written as [68]

$$\frac{d\sigma}{d\Omega} = b^2 + 2bp\lambda \cdot \mathbf{q} + p^2q^2 \tag{3.34}$$

where b is the aforementioned nuclear scattering length, and λ is the spin direction. Equations 3.32, 3.33 and 3.34 lead to important consequences observed in magnetic neutron diffraction patterns. First, for an unpolarized neutron beam, Equation 3.34

can be simplified to

$$\frac{d\sigma}{d\Omega} = b^2 + p^2 q^2 \tag{3.35}$$

and consequently there is no constructive interference between nuclear and magnetic scattering as the interference term averages to zero. Second, the intensity of magnetic reflections is proportional to the square of the ordered moment.

Combined Magnetic and Nuclear Structure Factor

The intensity of the diffraction in a specific direction when the magnetic moments are ordered is proportional to $|\mathcal{F}_{hkl}|^2$, which can be written as:

$$\begin{aligned} |\mathcal{F}_{hkl}|^2 &= \left|\sum_n b_n \exp\left[2\pi i \left(h\frac{x_n}{a} + k\frac{y_n}{b} + l\frac{z_n}{c}\right)\right]\right|^2 \\ &+ \left|\sum_n p_n \mathbf{q}_n \exp\left[2\pi i \left(h\frac{x_n}{a} + k\frac{y_n}{b} + l\frac{z_n}{c}\right)\right]\right|^2 . \end{aligned} \tag{3.36}$$

This separation of structure factors for the nuclear and magnetic scattering greatly simplifies the analysis of magnetic diffraction patterns in that the magnetic reflections below the magnetic transition temperature simply add to the nuclear reflections observed at all temperatures. A simple difference plot between patterns acquired above and below the transition temperature yields the purely magnetic contribution.

$p\mathbf{q}$ depends on the direction of the ordered moment. If all moments point in the same direction (ferromagnetism), all $p_n\mathbf{q}_n$ will be the same and the magnetic scattering is restricted to the same angular positions as the nuclear scattering. However, if moments point in different directions (anti-ferromagnetism for example), the magnetic contribution leads to new peaks at angular positions different from that of the nuclear scattering. A simple example of this effect is described in Appendix C. Moreover, if the location of magnetic peak can be indexed with crystallographic indices, since the magnetic moment needs to be in the reflection plane, it can directly imply the direction of the magnetic order. As we will see later in this work, in the case of

$Sm_3Ag_4Sn_4$, the presence of a (100) magnetic Bragg peak means that order cannot be along the *a*-axis.

Magnetic Form Factors

Magnetic scattering occurs when the magnetic moment of the neutron interacts with unpaired electrons in the atom. Consequently the scattering body for magnetic scattering is much larger than it is for nuclear scattering. As a result the form factor for magnetic scattering is a strong function of diffraction angle and the magnetic signal in a neutron diffraction pattern will be concentrated at low angles. For the rare earth atoms, the magnetic moment is accounted for by both spin and orbital angular moment contributions, and they will in turn each contribute to the magnetic scattering form factor [70].

3.2.3 Neutron Diffraction Instrumentation

Neutron diffraction experiments were carried out on the C2 powder diffractometer (DUALSPEC) at the NRU reactor, Canadian Neutron Beam Centre, Chalk River, Ontario. A review of neutron scattering facilities at Chalk River can be found in [71]. The reactor produces a neutron beam with a Maxwellian distribution of wavelengths with a peak at about 1.1 Å.

A simple diagram of the DUALSPEC powder diffractometer is shown in Figure 3.14. The beam then passes through a sapphire filter suppressing neutrons with a wavelength below 0.9 Å. A single-crystal Si monochromator allows for two main operational wavelengths: 1.329 Å (using the (531) reflection) and 2.370 Å(using the (331) reflection). The 1.329 Å wavelength probes a greater range of interplanar distances, however the magnetic signal is concentrated at low angles, as discussed above, and the 2.370 Å wavelength leads to a better resolution of the low angle peaks. For this reason, the magnetic neutron diffraction data in this study is acquired at a wavelength of 2.370 Å. The flat plate sample holder plane is normal to the beam line to maximize flux, and the diffracted neutrons go through an oscillating collimator of cadmium coated blades. The oscillation is to prevent an accidental blocking of neutrons in any specific direction. Finally, the neutrons are detected by a curved 800-wire BF_3 detector array with an interwire angle of 0.1° 2θ. The widths of the peaks in the observed diffraction pattern depend intimately upon the collimating system, the nature of the monochromator, the neutron spectral distribution, and the shape and crystalline perfection of the sample [72].

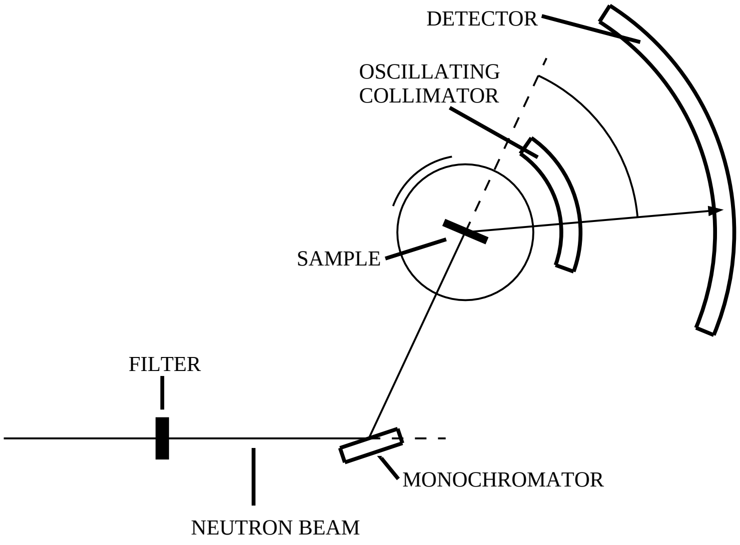

Figure 3.14: Schematic diagram of the DUALSPEC powder diffractometer.

3.2.4 Absorption and Flat-Plate geometry

For Sm and Gd the cylindrical geometry is rendered impractical by the large values of σ_a. Workers have exploited the wavelength dependence of σ_a, and used hot neutron sources yielding short wavelengths (below 0.6 Å) to reduce σ_a to a workable few hundred barn [73, 74]. This strategy not only requires access to a hot source, but has the added disadvantage of compressing useful scattering to low angles leading to line overlap and loss of resolution. Since we are mostly interested in magnetic scattering which is strongest at low angles, as discussed above, this strategy is not ideal. One can alternatively use the fact that in natural Gd almost all of the absorption comes for the ^{155}Gd and ^{157}Gd isotopes, and for natural Sm from the ^{149}Sm isotope, and prepare samples using separated isotopes, leaving out the highest absorbers, as starting materials. The extreme cost of separated isotopes combined with the high vapour pressure of Sm, makes sample preparation all the more difficult.

In order to perform the measurement at the 2.370 Å wavelength mentioned above, and not have too much material which would absorb the incoming neutrons, the powder sample is thinly laid on a flat plate sample holder with silicon single-crystal windows [75]. This allows a significant area of the incident beam to be used and compensates for the small thickness of the sample. A detailed characterization of the sample, including acquisition and analysis of some of the data in this work, confirmed its effectiveness [75]. Use of a flat geometry introduces broadening of low angle peaks, and an absorption driven decrease in the intensity of high angle peaks since the neutrons travel through more material. These effects are not significant in the present study since we limit our analysis to the lower angle region of the data and the line broadening can be accounted for in the peak profile used in the fit. The flat plate sample holder is shown in Figure 3.15.

Figure 3.15: Photograph of the flat-plate sample holder used for Gd and Sm neutron diffraction experiments.

3.3 Sample Preparation

The $Nd_3Cu_4Sn_4$, $Nd_3Ag_4Sn_4$, $Ho_3Cu_4Sn_4$ and $Gd_3Cu_4Sn_4$ samples were prepared in a tri-arc furnace with a base pressure of less than 6×10^{-7} mbar. Stoichiometric amounts of pure elements (99.9 wt% Ho, Nd, Cu, and 99.999 wt% Ag and Sn), with an excess of 10 wt% Ag which compensated for losses due to the high vapour pressure of Ag, were melted several times under pure (< 1 ppm impurity) argon to ensure homogeneity. The ingots were sealed in quartz tubes with a partial pressure of He, annealed at 800°C for one week and water quenched. To characterize the structure and phase purity of the samples, Cu K_α x-ray diffraction patterns were acquired and were fitted with GSAS[76] via the EXPGUI[77] user interface. The $Nd_3Cu_4Sn_4$ sample had less than 5 wt% $NdCu_2Sn_2$, and the $Nd_3Ag_4Sn_4$ had less than 2 wt% NdAgSn.

Many of the samples presented in this study were provided by the group of P. Riani in Genoa, Italy. The $Sm_3Cu_4Sn_4$, $Sm_3Ag_4Sn_4$, $Gd_3Ag_4Sn_4$ and $Gd_3Cu_4Ge_4$ were prepared with stoichiometric amounts of Sm, 99.9 wt% purity, Gd, 99.9 wt% purity, Ag, Sn and Ge, 99.999 wt% purity, were placed in a tantalum crucible which was sealed by arc welding under purified argon. They were then melted in an induction furnace, quenched in water and annealed at 600°C for 20 days. Electron microprobe analysis and Cu K_α x-ray diffraction confirmed that the majority phase was the orthorhombic $Gd_3Cu_4Ge_4$-type phase. The $Gd_3Ag_4Sn_4$ sample had less than 5% of the ζ-phase $Ag_{79}Sn_{21}$ present, whereas the $Sm_3Ag_4Sn_4$ had less than 6% of the ζ-phase $Ag_{79}Sn_{21}$ present.

Chapter 4

The simple cases of transfer

The ^{119}Sn Mössbauer spectroscopy data on many of the $R_3T_4Sn_4$ compounds can be described by the relatively simple isotropic field transfer model and achieves excellent agreement with the neutron diffraction, magnetization and susceptibility data. More importantly though, the ^{119}Sn Mössbauer spectroscopy data can yield additional information which cannot be obtained from neutron diffraction due to insensitivity or experimental difficulties. Some of the results presented in this section can also be found in print elsewhere [78, 79].

As stated in section 2.2, each Sn site in the $R_3T_4Sn_4$ materials has rare earth nearest neighbours. Ordering of each of the rare earth sublattices should lead to a transferred hyperfine field at one or both of the Sn sites in the structure, as long as the effects of the nearest neighbour moments do not cancel. Each of the Sn sites in the structure have four R-4e nearest neighbours and their effect will depend entirely on the magnetic structure of the R-4e sublattice. The Sn-4f site has a single R-2d neighbour while the Sn-4h site has two. Consequently any ordering of the R-2d sublattice contributes to a transferred field at the Sn-4f site. Moreover, if the R-4e magnetic structure leads to a cancellation at both Sn sites, or the R-4e sublattice is not ordered, ordering of the R-2d site often leads to a 2:1 field ratio between the two sites, the simplest scenario which leads to such a ratio.

Mössbauer spectroscopy is phase quantitative, as discussed in section 3.1.9. Since the crystallographic populations of the Sn sites in the crystal structure are equal, we expect to observe two equal area subspectra that compose the ^{119}Sn Mössbauer spectrum, or a simple subdivision of this ratio.

Finally, the point symmetry of the Sn-4f and Sn-4h sites ($2mm$ and $m2m$ respectively) in the $Gd_3Cu_4Ge_4$-type structure force the principal axis of the electric field gradient, V_{zz}, to point along one of the crystallographic axes (not necessarily the same one). The point symmetries still allow the possibility that the electric field is not axially symmetric, i.e. η can be non-zero. In order to verify this assertion a primitive point charge calculation for each site indicates that indeed the electric field gradient is restricted to be along the crystallographic axes and η would vary depending on the charges used. All ^{119}Sn Mössbauer spectra were fitted using a standard least squares refinement routine using the full Hamiltonian solution described in section 3.1.7.

4.1 $Nd_3Ag_4Sn_4$ and $Pr_3Cu_4Sn_4$

Neutron diffraction measurements on $Nd_3Ag_4Sn_4$ indicated that both the Nd-2d and Nd-4e sublattices order together at 5 K, adopting independent antiferromagnetic structures with quite different moments. The 1.3 μ_B Nd-2d moments order parallel to the *a*-axis, while the 2.3 μ_B Nd-4e moments lie in the *ab* plane making an angle of 144° with the *a*-axis [8].

The ^{119}Sn Mössbauer spectrum at 14 K shown in Figure 4.1(a), well above the ordering temperature, exhibits the typical non-magnetic quadrupole doublet, split by 0.783(5) mm/s, that is the trademark of the paramagnetic state in all $R_3T_4Sn_4$ ^{119}Sn Mössbauer spectroscopy data. Only a single doublet is observed, indicating that the electrostatic environments of the two Sn sites are quite similar and cannot be resolved. The ^{119}Sn Mössbauer spectrum at 1.6 K, shown in Figure 4.1(b), exhibits far greater splitting. The spectrum shows two equal area components, consistent

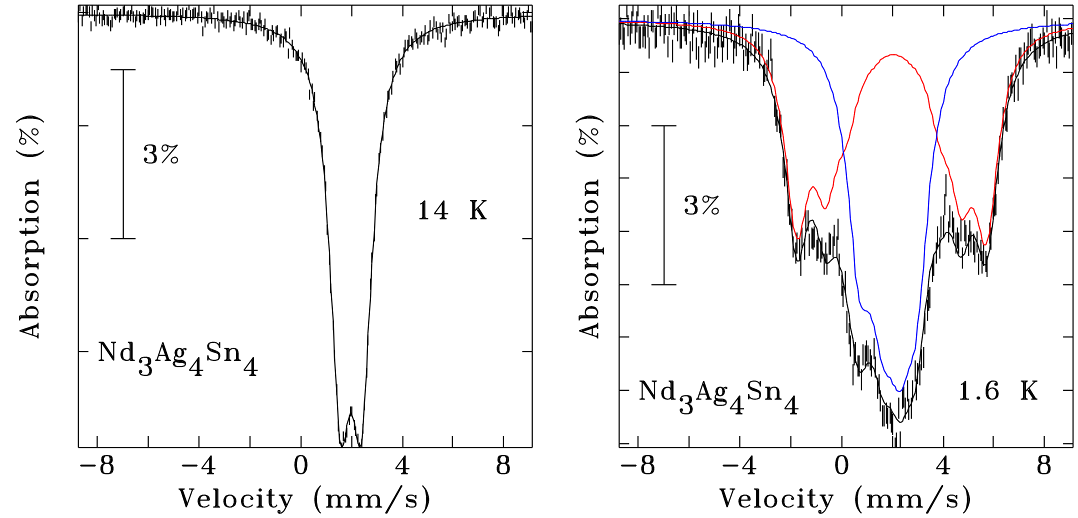

(a) ^{119}Sn Mössbauer spectrum of $Nd_3Ag_4Sn_4$ at 14 K, exhibiting the typical non-magnetic quadrupole split doublet.

(b) ^{119}Sn Mössbauer spectrum of $Nd_3Ag_4Sn_4$ at 1.6 K, exhibiting significant magnetic splitting. The Sn-4f (blue) and Sn-4h (red) components are also shown.

Figure 4.1: Non-magnetic (14 K) and magnetic (1.6 K) ^{119}Sn Mössbauer spectra of $Nd_3Ag_4Sn_4$. Solid black lines are fits obtained with a full Hamiltonian solution.

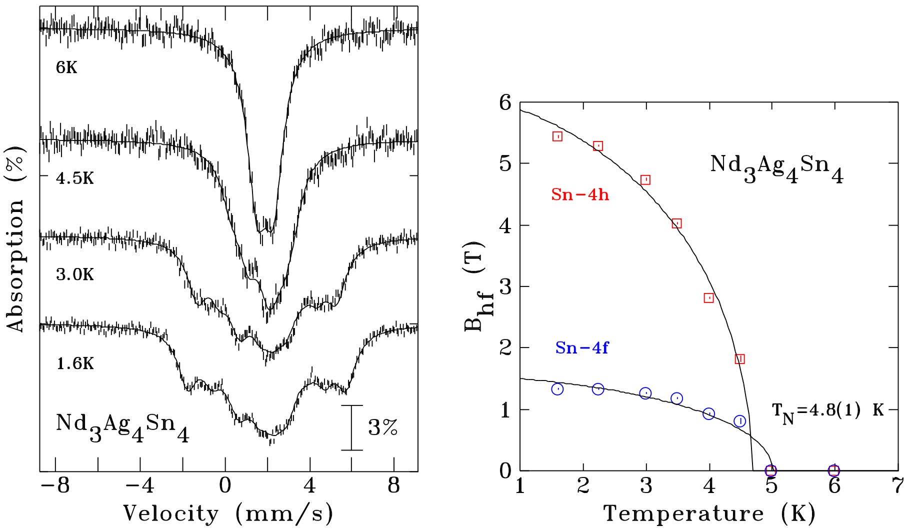

(a) ^{119}Sn Mössbauer spectra of $Nd_3Ag_4Sn_4$. Solid black lines are fits obtained with a full Hamiltonian solution.

(b) Temperature dependence of the hyperfine fields at the Sn-4h (□) and Sn-4f (○) sites in $Nd_3Ag_4Sn_4$ showing an average transition temperature of 4.8(1) K. Solid black lines are $J = \frac{9}{2}$ (the value for Nd^{3+}) Brillouin functions.

Figure 4.2: Temperature dependence of the ^{119}Sn Mössbauer spectra of $Nd_3Ag_4Sn_4$ and the fitted hyperfine magnetic field B_{hf}.

with the crystallographic populations of the two Sn sites. The fitted values of B_{hf} are 5.43(2) T and 1.32(2) T. The two subspectra are also shown in red and blue (the Sn site assignment will be achieved using the neutron diffraction results discussed below).

The temperature dependence of the ^{119}Sn Mössbauer spectra is shown in Figure 4.2(a). The lines collapse to the center with increasing temperature, and by 5 K only the paramagnetic doublet is observed. Tracking the temperature dependence of the two hyperfine fields (shown in Figure 4.2(b)) and fitting the components with $J = \frac{9}{2}$ (the value for Nd^{3+}) Brillouin functions, yields an average ordering temperature

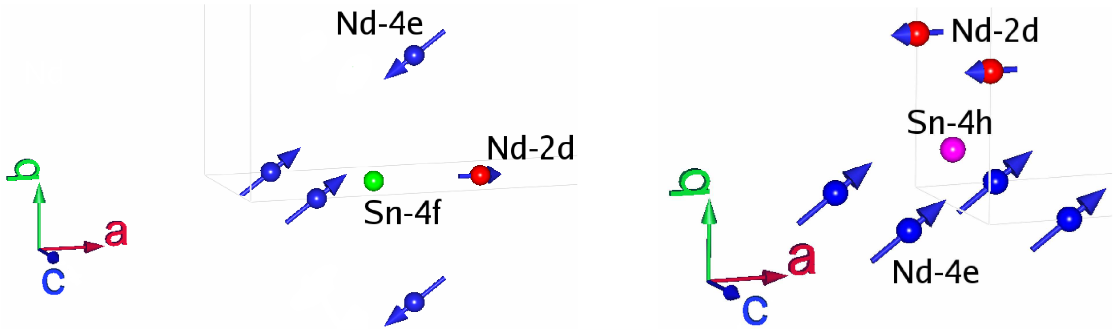

(a) Nd-2d (red) and Nd-4e (blue) neighbour moments to the Sn-4f (green) site.

(b) Nd-2d (red) and Nd-4e (blue) neighbour moments to the Sn-4h (pink) site.

Figure 4.3: Nearest neighbour moments to the Sn-4f and Sn-4h sites in $Nd_3Ag_4Sn_4$.

of 4.8(1) K consistent with the neutron diffraction results [8].

We can use the magnetic structure obtained from neutron diffraction measurements to estimate the expected transferred field ratio between the Sn-4h and Sn-4f sites. The Sn-4h site has two Nd-2d (1.3 μ_B) neighbours oriented parallel to the a-axis and four Nd-4e (2.3 μ_B) neighbours aligned in the ab plane (Figure 4.3(b)), making an angle of 54° with the a-axis. However, the four Nd-4e neighbours of the Sn-4f site occur as two anti-parallel pairs and their contribution should cancel, leaving only a single Nd-2d moment to affect the Sn-4f site (Figure 4.3(a)) [8]. If we assume purely isotropic field transfer, as discussed in section 3.1.11, the local field is simply a vector sum over the magnetic neighbours (including the different magnitudes of Nd moments), then we estimate a Sn-4h:Sn-4f field ratio of 5.6:1 which compares well with the observed ratio of 4.11(6):1 and allowing the assignment the higher field component to Sn atoms in the Sn-4h site.

We expect, due to point symmetry, that V_{zz} point along one of the crystallographic axes for each of the Sn sites. The angles ϑ between V_{zz} and B_{hf} for the Sn-4f and Sn-4h sites are 85(3)° and 56(1)° respectively. Again, if we assume isotropic transfer,

ϑ should be either 90° or 0° for the Sn-4f site, agreeing with our measurement. The Sn-4h site should have an angle of 41° or 49° still in reasonable agreement with our data. The asymmetry parameter η for both Sn sites refines to 0 within error.

Neutron diffraction measurements on $Pr_3Cu_4Sn_4$ indicated that both Pr sites order together at 11 K, adopting an antiferromagnetic structure with slightly different moments on each Pr sublattice. The 2.9 μ_B Pr-2d moments and the 2.3 μ_B Pr-4e moments order parallel to the *a*-axis with antiferromagnetic coupling along the *c*-axis. The magnetic structure thus consists of *ab* sheets of moments with alternating sign every half lattice in the *c* direction [28]. We note that the figure presented in [28] is not consistent with the described magnetic structure. We have performed a neutron diffraction experiment on the $Pr_3Cu_4Sn_4$ sample used in this study, and confirmed that the structure described in the text is correct.

The ^{119}Sn Mössbauer spectrum of $Pr_3Cu_4Sn_4$ acquired at 2 K is shown in Figure 4.4. The spectrum shows two equal area components with fields of 6.99(2) T and 1.53(2) T (plotted in red and blue), also consistent with the crystallographic populations of the two Sn sites, with a small ($< 6\%$ area) unsplit impurity.

The Sn-4h site has two Pr-2d (2.9 μ_B) neighbours oriented parallel to the *a*-axis and four Pr-4e (2.3 μ_B) also parallel to the *a*-axis (Figure 4.5(b)). The Sn-4f has four Pr-4e neighbours that occur as two anti-parallel pairs and their contributions should cancel, leaving only a single Pr-2d moment to affect the Sn-4f site (Figure 4.5(a)). Assuming again that the local field is simply a vector sum over the magnetic neighbours (isotropic transfer), we estimate a Sn-4h:Sn-4f field ratio of 5.2:1 which compares well with the observed ratio of 4.57(6):1 and allows us to assign the higher field component to Sn atoms in the Sn-4h site. We note that magnetic $Pr_3Cu_4Sn_4$ spectrum fits best with a rather large η, 0.9(1), unlike all other compounds measured in this study. The variation in values of the quadrupole parameters is discussed in more detail later (see Chapter 7).

Similarly to the $Nd_3Ag_4Sn_4$, we expect, assuming isotropic field transfer, that the

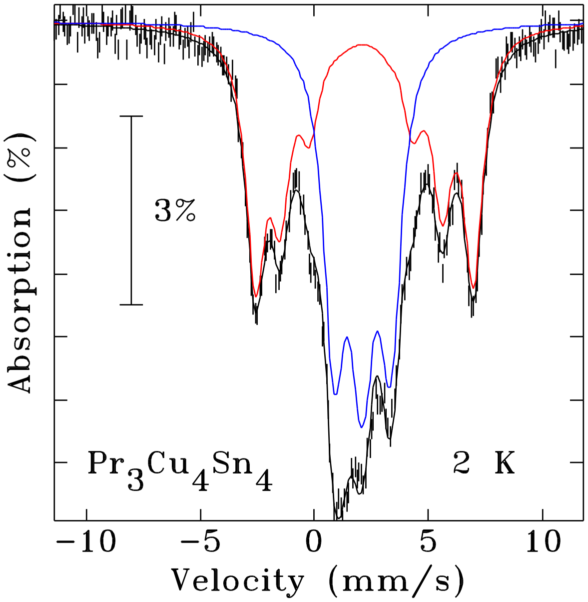

Figure 4.4: ^{119}Sn Mössbauer spectrum of $Pr_3Cu_4Sn_4$ acquired at 2 K. The component associated to the Sn-4h site is shown in red, and the component associated to the Sn-4f site is shown in blue.

angles between B_{hf} and V_{zz} for both Sn sites be either 90° or 0°. The fitted angle at the Sn-4h is 84(3)° in quite good agreement with the prediction. The fitted angle at the Sn-4f site is 76(5)°, still in reasonable agreement with the prediction.

4.2 $Ho_3Cu_4Sn_4$

The magnetic behaviour of $Ho_3Cu_4Sn_4$ measured by neutron diffraction, heat capacity and magnetization, is quite complex and the original neutron diffraction results [30] had to be subsequently revised to include more intermediate magnetic structures [36]. Magnetization places the primary ordering temperature at just above 8 K [30, 80, 81]. Specific heat data, however, along with neutron diffraction results, show that the Ho-2d sublattice orders at 7.6 K in an incommensurate magnetic structure. The Ho-2d moments then shifts into a similar but commensurate structure at 5.5 K only to

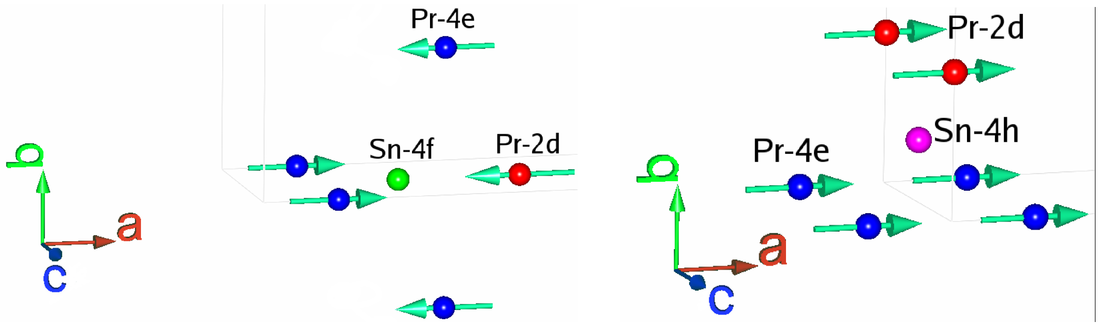

(a) Pr-2d (red) and Pr-4e (blue) neighbour moments to the Sn-4f (green) site.

(b) Pr-2d (red) and Pr-4e (blue) neighbour moments to the Sn-4h (pink) site.

Figure 4.5: Nearest neighbour moments to the Sn-4f and Sn-4h sites in $Pr_3Cu_4Sn_4$ taken from neutron diffraction results [28].

subsequently reorient again at 4.4 K. The Ho-4e sublattice orders independently at 3.3 K in an incommensurate magnetic structure and undergoes a reorientation at 2.3 K.

The spectrum at 1.63 K (Figure 4.6(b)), shows the expected two-site form, with hyperfine fields of 3.89(1) T and 1.79(2) T. The temperature dependence of these fields (Fig. 4.7(b)) however, is not simple. $J = \frac{1}{2}$ Brillouin functions (rather than the expected $J = 8$) gave the best fits to the basic trends up to 8 K and yielded an average ordering temperature of 8.2(1) K, consistent with magnetization data, but somewhat above that inferred from heat capacity. Examination of the magnetic structure obtained from neutron diffraction adopted by the Ho-4e moments at 1.63 K leads to the expectation that their contributions to the transferred hyperfine field cancel at both Sn sites (Figures 4.8(a) and 4.8(b)). The two Ho-2d neighbours of the Sn-4h site are parallel to each other, and the Sn-4f site has a single Ho-2d neighbour, leading to a simple prediction of a 2:1 field ratio for Sn-4h:Sn-4f. The observed ratio at 1.63 K is 2.17(3):1, and this allows us to assign the higher field component to the Sn-4h site.

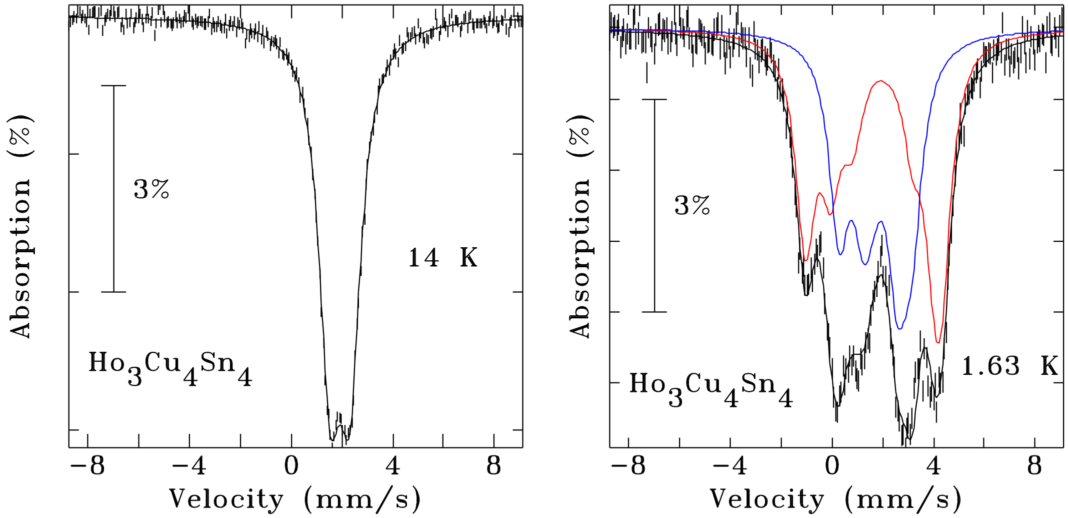

(a) Quadrupole doublet ^{119}Sn Mössbauer spectrum of $Ho_3Cu_4Sn_4$ at 14 K.

(b) Magnetic ^{119}Sn Mössbauer spectrum of $Ho_3Cu_4Sn_4$ acquired at 1.63 K.

Figure 4.6: ^{119}Sn Mössbauer spectra of $Ho_3Cu_4Sn_4$ at 14 K and 1.63 K.

The fitted angle between B_{hf} and V_{zz} is 90(1)° for Sn-4h site in excellent agreement with the point group symmetry prediction. The fitted angle between B_{hf} and V_{zz} is 80(5)° for the Sn-4f site, again in good agreement with the point symmetry prediction.

As discussed above, the Sn-4f site has a single Ho-2d neighbour whereas the Sn-4h site has two. The temperature dependence of B_{hf}, shown in Figure 4.7(b), becomes problematic since above 6 K, the ratio between fields observed is greater than a factor of two in favour of the Sn-4h site, greater than the maximum ratio allowed by nearest neighbour coordination. Any order of the Ho-2d sublattice must lead to a transferred field at the Sn-4f site since the single neighbour moment cannot cancel with any other. Yet, above 8 K, the field would be 0 at the Sn-4f site and non-zero at the Sn-4h. Hence, the Sn-4f, Sn-4h site assignment is considered valid only up to 6 K (shown as a dashed line in Figure 4.7(b)).

The temperature dependence of the B_{hf} is quite smooth with the exception of a slight break above 6 K. The events at 5.5 K, 4.4 K, 3.3 K and 2.3 K cannot be

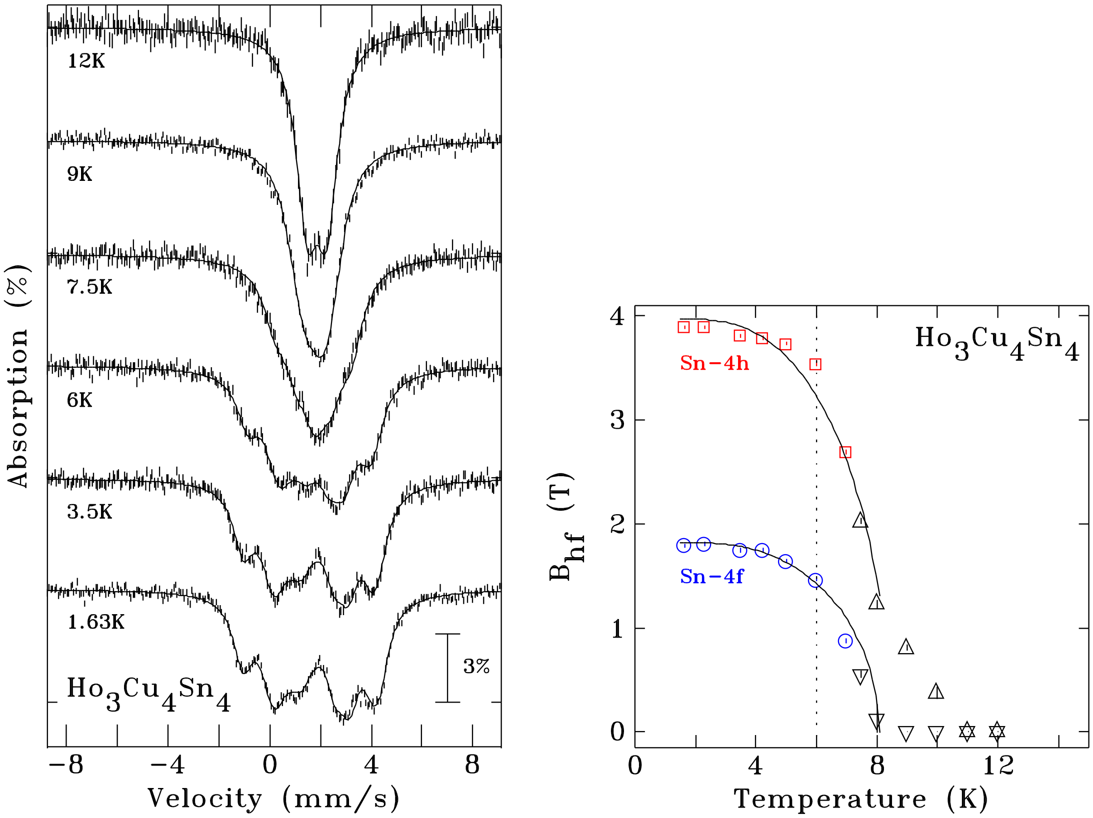

(a) Temperature dependence of the ^{119}Sn Mössbauer spectra of $Ho_3Cu_4Sn_4$.

(b) Temperature dependence of the fitted hyperfine magnetic field B_{hf}. The Sn-4h site (□) and the Sn-4f site (◯) assignments are only considered valid up to 6 K, above which the high field (△) and low field (▽) components cannot be associated to a specific Sn site.

Figure 4.7: Temperature dependence of the ^{119}Sn Mössbauer spectra of $Ho_3Cu_4Sn_4$ and the fitted hyperfine magnetic field B_{hf}.

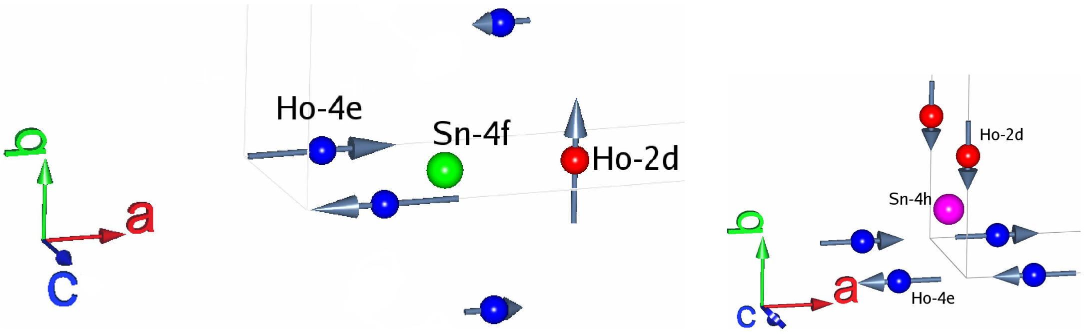

(a) Ho-2d (red) and Ho-4e (blue) neighbour moments to the Sn-4f (green) site.

(b) Ho-2d (red) and Ho-4e (blue) neighbour moments to the Sn-4h (pink) site.

Figure 4.8: Nearest neighbour moments to the Sn-4f and Sn-4h sites in $Ho_3Cu_4Sn_4$ at base temperature.

resolved or simply cannot be detected by ^{119}Sn Mössbauer spectroscopy. The typical doublet obtained in the paramagnetic state (as seen in Figure 4.6(a)) does not appear at the expected transition temperature and a residual transferred field persists up to just above 10 K, suggesting the possible presence of short range magnetic order in the Ho-2d sublattice above the primary ordering temperature, similar to what was observed for the Ho-4e lattice above its ordering temperature [36].

4.3 $Nd_3Cu_4Sn_4$

$Nd_3Cu_4Sn_4$ provides a third relatively simple example of magnetic ordering in the $R_3T_4Sn_4$ compound series. It also serves to illustrate the power of ^{119}Sn Mössbauer spectroscopy in detecting magnetic order. Heat capacity and susceptibility measurements both place the onset of magnetic order at 1.8 K [29], however a more recent neutron diffraction study failed to find any magnetic scattering at 1.5 K [28]. It is immediately clear from the 1.6 K spectrum shown in Figure 4.9(a) that a magnetic splitting is present at that temperature. The patterns can be fitted with two equal

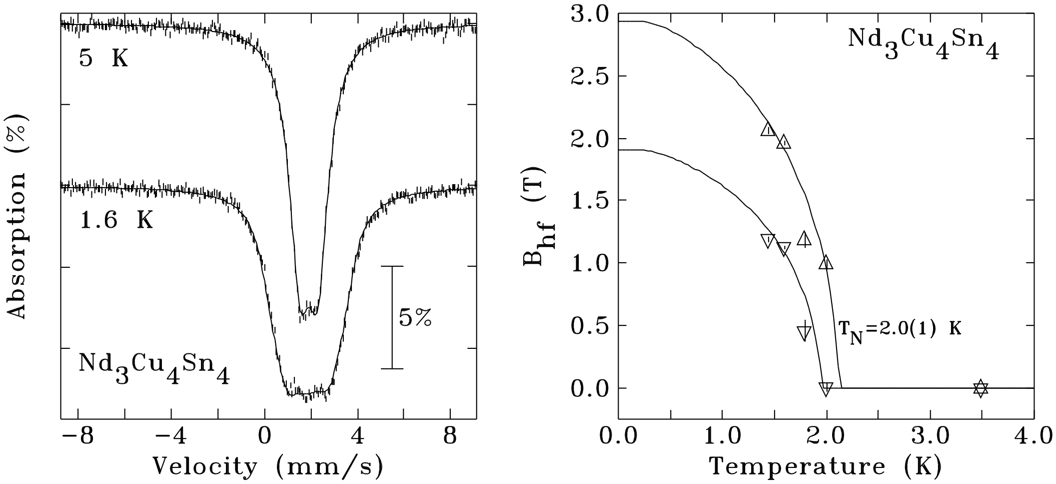

(a) Temperature dependence of the ^{119}Sn Mössbauer spectra of $Nd_3Cu_4Sn_4$.

(b) Temperature dependences of the fitted hyperfine magnetic field B_{hf} for the high field (△) and low field (▽) components.

Figure 4.9: Temperature dependence of the ^{119}Sn Mössbauer spectra of $Nd_3Cu_4Sn_4$ and the fitted hyperfine magnetic field B_{hf}.

area subspectra. The low resolution due to small splitting, however, makes determining the correct model somewhat speculative. Tracking the temperature dependence of the observed splitting yields an estimated ordering temperature of 2.0(1) K, fully consistent with the previously reported values.

The observed hyperfine fields (2.06(3) T and 1.19(2) T at 1.45 K) are not especially small and allow us to fit the temperature dependence of the hyperfine fields of both subspectra to a $J = \frac{9}{2}$ Brillouin function (as was the case for $Nd_3Ag_4Sn_4$). The resulting fit, shown in Figure 4.9(b), reveals that the field is above 50% of the extrapolated maximum by 1.45 K (our lowest temperature) indicating that it should detected by neutron diffraction at 1.5 K. An initial neutron diffraction measurement at 0.38 K was performed on the $Nd_3Cu_4Sn_4$ sample used in the ^{119}Sn Mössbauer spectroscopy measurements and is shown in Figure 4.10. The neutron diffraction pattern taken at 0.38 K (shown in red) clearly exhibits a magnetic contribution not seen in the paramagnetic 3.2 K pattern shown in blue. The green pattern is the difference between the magnetic and non-magnetic diffraction patterns (scaled by a factor of three for clarity), and shows the exclusively magnetic scattering. It is as of yet still unclear why no magnetic signal was observed in the original neutron diffraction work [28]. It is possible that $Nd_3Cu_4Sn_4$ adopts a complex magnetic structure that leads to distributed and therefore weak scattering at temperatures around and above 1.5 K.

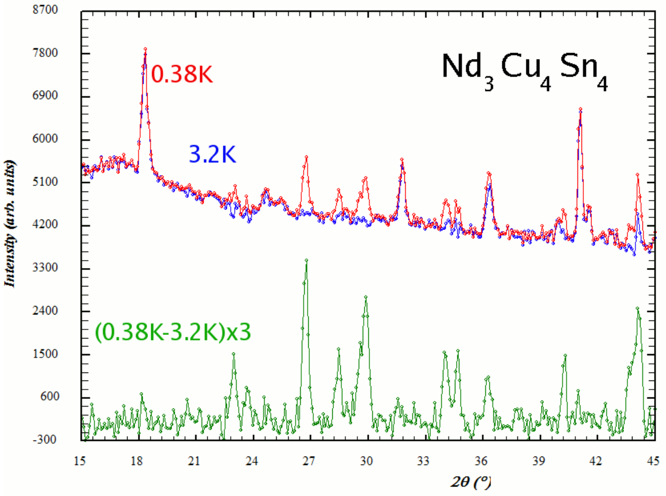

Figure 4.10: Preliminary neutron diffraction results on $Nd_3Cu_4Sn_4$. There is a clear additional magnetic contribution to the 0.38 K pattern (shown in red), that is not present in the paramagnetic pattern (shown in blue). The purely magnetic portion of the signal is shown in a difference between the magnetic and non-magnetic patterns (shown in green).

Finally, it is relevant to note that the observed field ratio of 1.74:1 suggests that we are seeing only the effects of the Nd-2d moments and that the Nd-4e sublattice is either not ordered or it adopts a magnetic structure that leads to a cancellation at the two Sn sites (as is the case in $Ho_3Cu_4Sn_4$).

4.4 Conclusions

^{119}Sn Mössbauer spectroscopy measurements on $Nd_3Ag_4Sn_4$ and $Pr_3Cu_4Sn_4$ have demonstrated that the technique leads not only to a value of the transition temperature consistent with earlier neutron diffraction results, but also a value for the transferred field ratio between the two Sn sites consistent with the neutron diffraction derived magnetic structure, and values of the angles between B_{hf} and V_{zz} that are consistent with point symmetries for both Sn sites.

In the case of $Ho_3Cu_4Sn_4$, ^{119}Sn Mössbauer spectroscopy measurements demonstrated the clear and unambiguous presence of magnetic interactions above the ordering temperature which went undetected in the neutron diffraction experiments. The ability of ^{119}Sn Mössbauer spectroscopy to detect order that may be invisible to neutron diffraction experiments is demonstrated even more strikingly in the case of $Nd_3Cu_4Sn_4$ for which neutron diffraction detected no order at all.

Neutron diffraction is most sensitive to long ranged static order. As the magnetic peak intensity scales as the square of the ordered moment, neutron diffraction is not very sensitive to small moments. On the other hand, ^{119}Sn Mössbauer spectroscopy is sensitive to the size of the hyperfine field at the probe nucleus which grows linearly with the ordered moment. Consequently, the technique is sensitive not only to long ranged order but also exhibits a clear splitting even for very small fields often related to short ranged order. Measurements on $Nd_3Ag_4Sn_4$, $Pr_3Cu_4Sn_4$ and $Ho_3Cu_4Sn_4$ confirm previously obtained results (in the $Nd_3Cu_4Sn_4$ case, correct an error) and add information that would be far more difficult or even impossible to obtain via neutron diffraction. These results also indicate that the two techniques can be coupled to achieve a better understanding of the magnetic behaviour of these materials. The combination is especially useful when neutron diffraction encounters significant physical or experimental limitations as the next chapters will demonstrate.

Chapter 5

Sm Compounds

The $Sm_3T_4Sn_4$ compounds appear to be typical members of the $R_3T_4Sn_4$ family and the transition temperatures obtained from magnetization and susceptibility data seem to scale well with the de Gennes factor. However, as was mentioned in section 2.4, there is no available data on these compounds from a direct probe of magnetism. This lack of data stems mostly from the experimental difficulties involved in neutron diffraction measurements (as discussed in section 3.2.4). In this section, the combined use of ^{119}Sn Mössbauer spectroscopy and flat-plate neutron diffraction reveals a wealth of new behaviour. The results presented in this section can also be found in print elsewhere [79, 82].

5.1 $Sm_3Ag_4Sn_4$

Initial magnetic characterization by ac susceptibility, shown in Figure 5.1, reveals a clear peak at 8.25(15) K, close to the 9 K value previously attributed to the onset of antiferromagnetic (AF) order in this compound obtained from magnetization data [33]. An extremely weak departure from Curie-Weiss 1/T behaviour may be present between 20 and 25 K, and this is confirmed by the out-of-phase signal (χ'') shown in the inset to Figure 5.1, where a clear feature is apparent at 24(1) K. As shown below using ^{119}Sn Mössbauer spectroscopy, the onset of magnetic order occurs at ∼26 K, while the 8.25(15) K event marks a spin reorientation, making the assignment of the primary ordering identifiable in the susceptibility data only in hindsight.

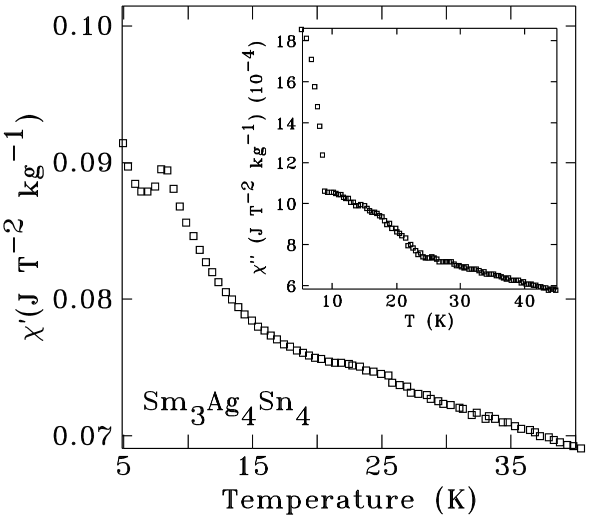

Figure 5.1: Temperature dependence of the in-phase ac susceptibility (χ') in $Sm_3Ag_4Sn_4$, acquired with a field of 1 mT at 337 Hz. The inset shows the out-of-phase signal, acquired at 977 Hz on a much larger (0.5 g) sample. The reorientation transition at 8.25(15) K is evident in both channels, while only χ'' shows a clear signature of the bulk ordering at 24(1) K.

5.1.1 ^{119}Sn Mössbauer Spectroscopy

Examination of the 2.2 K spectrum, shown in Figure 5.2, reveals two magnetically split, equal-area components, consistent with the populations of the Sn-4f and Sn-4h sites. Each component has a distinct hyperfine field (8.44(2) and 3.11(2) T), with no significant non-magnetic contribution present. We conclude that all of the Sn in the sample is in the primary $Sm_3Ag_4Sn_4$-phase and that each of the two crystallographically distinct Sn sites is also a magnetically unique site. There is no apparent line broadening or subsplitting of the components that might reflect a more complex magnetic environment.

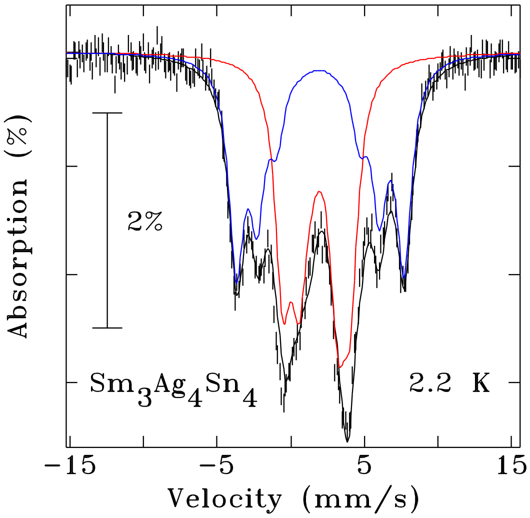

Figure 5.2: ^{119}Sn Mössbauer spectrum of $Sm_3Ag_4Sn_4$ acquired at 2.2 K. The solid line through the data is a full Hamiltonian fit. The two equal-area components making up the fit are shown in blue for the Sn-4f component and red for the Sn-4h component.

The spectrum was fitted by fixing the magnitude of the quadrupole splitting, $eQ_eV_{zz}/2\sqrt{1+\frac{\eta^2}{3}}$, to 0.87 mm/s for both subspectra. This value was obtained from spectra taken in the paramagnetic state (at 35 K) where again, only a simple doublet is observed, indicating that the electrostatic environments of the two Sn sites are quite similar and could not be resolved. Since a paramagnetic ^{119}Sn Mössbauer spectrum can only reveal the magnitude of $eQ_eV_{zz}/2\sqrt{1+\frac{\eta^2}{3}}$, the negative sign of $eQ_eV_{zz}/2\sqrt{1+\frac{\eta^2}{3}}$ for both subspectra was established by fitting the spectra in the magnetically ordered state at 2.2 K. As discussed in the previous chapter, due to the point groups of the Sn-4f and Sn-4h sites ($2mm$ and $m2m$ respectively), we expect the principal axis of the electric field gradient tensor, V_{zz} , to be parallel to one of the crystallographic axes. The electric field gradient asymmetry parameter, η, was found to be small (<0.2) in both cases. η was therefore set to zero and not refined in the initial analysis of the Mössbauer spectra.

Figure 5.3(a) shows the progression of the ^{119}Sn Mössbauer spectra with temperature. Clearly the magnetic splitting persists well above the 9 K transition temperature inferred from susceptibility data. No significant (<2%) impurity was detected at any temperature, indicating that the magnetic behaviour observed here reflects bulk ordering in the primary phase. Moreover, the spectral areas remain equal throughout, evidence that we can resolve the evolution of B_{hf} at each Sn site (4h and 4f). From our fits, we obtain the temperature dependence of B_{hf} for each site and the corresponding angle θ between B_{hf} and V_{zz}, shown in Figure 5.3(b).

The temperature dependence of B_{hf} for each component was fitted to a sum of two $J = \frac{5}{2}$ (the value for Sm^{3+}) Brillouin functions. This yields Néel temperatures ($\mathrm{T_N}$) of 26.2(4) and 25.2(1.3) K from the high-field and low-field sites, respectively, giving a weighted average transition temperature of $\mathrm{T_N} = 26.0(5)$ K. Similarly, the low-temperature event occurs at 8.6(3) and 8.0(3) K for an average of 8.3(3) K, and corresponds precisely with the 8.25(15) K peak seen in $\chi'(\mathrm{T})$ (Figure 5.1). This event marks an abrupt change in the direction of B_{hf} at both Sn sites, and must in turn reflect a change in the surrounding Sm moment directions. Such behaviour has been observed in other compounds such as $\mathrm{Tb_3Ag_4Sn_4}$ [6] and $\mathrm{Dy_3Ag_4Sn_4}$ [38], and given the presence of magnetic order well above 8 K, the ^{119}Sn Mössbauer data clearly show that the sharp feature seen in Figure 5.1 is not actually due to the onset of long-range magnetic order, but rather marks a magnetic reorientation transition.

There is no observed change in linewidth on passing through the 8 K event, nor are there any changes to the spectral shape that cannot be accounted for by the static Hamiltonian used to calculate the line positions and intensities; we therefore conclude that the magnetic order that is observed in the Mössbauer spectra for $8\ \mathrm{K} < \mathrm{T} < 26\ \mathrm{K}$ is static in nature and reflects long-range ordering of the Sm moments. However, as a local probe of magnetic order, Mössbauer spectroscopy cannot definitively show that long-ranged magnetic order is present. For this information, we turn to neutron diffraction.

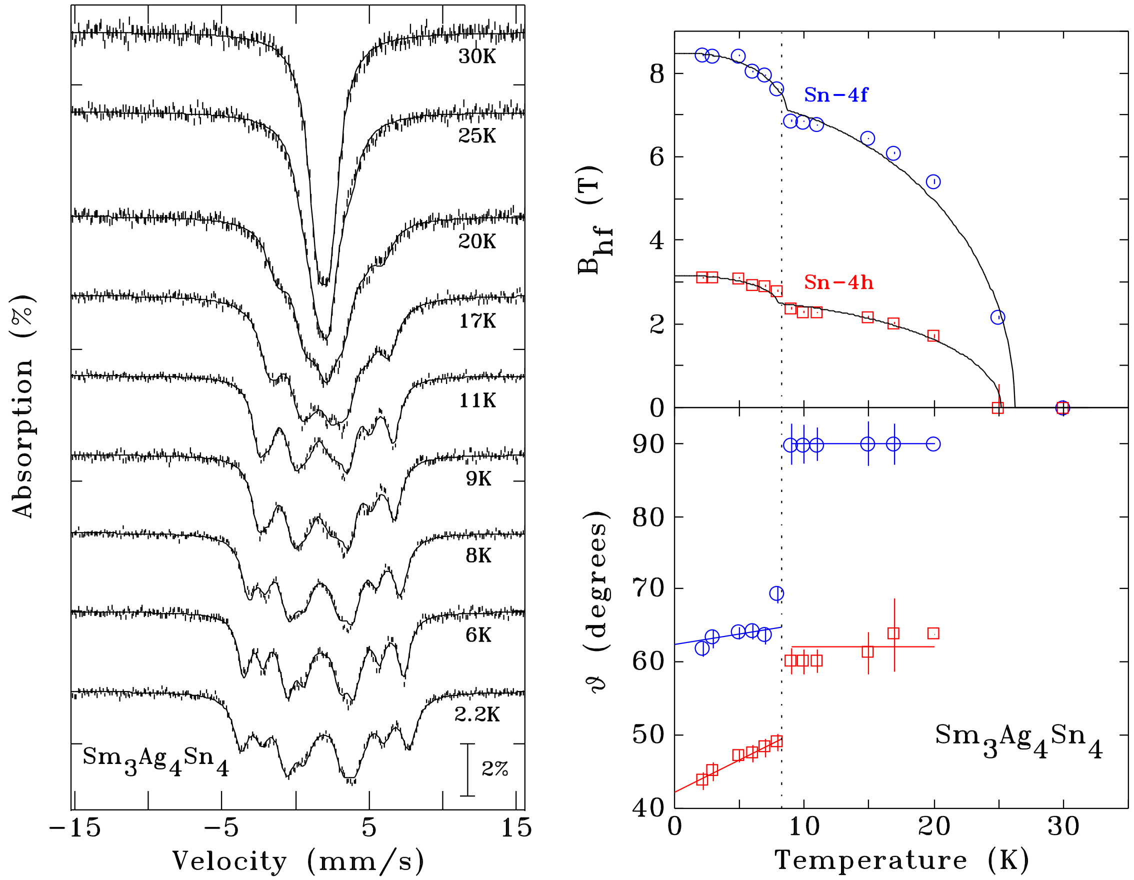

(a) Temperature dependence of the ^{119}Sn Mössbauer spectra of $Sm_3Ag_4Sn_4$. There is a clear magnetic contribution to the spectra well above 9 K.

(b) Top: temperature dependence of the hyperfine field B_{hf} fitted with a sum of two $J = \frac{5}{2}$ Brillouin functions; Bottom: the angle (ϑ) between V_{zz} and B_{hf}. Solid lines are guides to the eye.

Figure 5.3: Summary of the ^{119}Sn Mössbauer spectroscopy data for $Sm_3Ag_4Sn_4$.

5.1.2 Neutron Diffraction

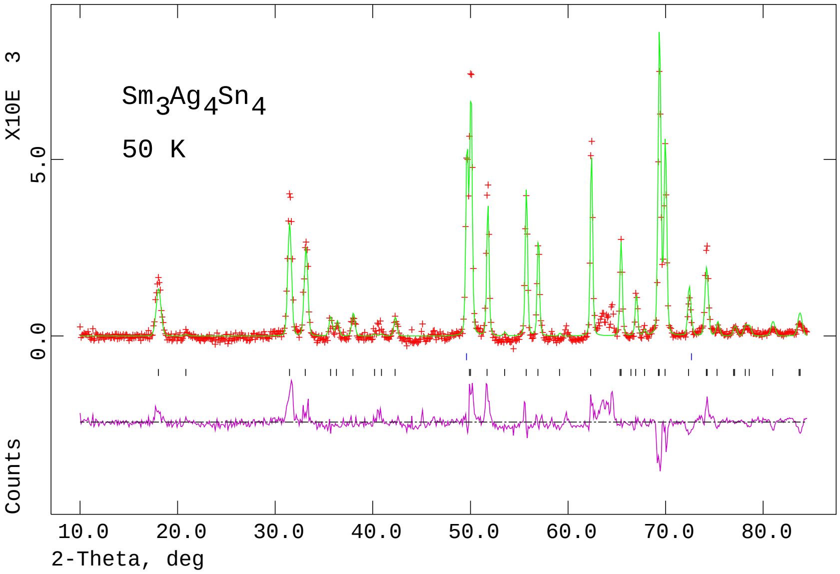

Figure 5.4: Neutron diffraction pattern taken at 50 K (paramagnetic state) at a wavelength of 2.37150(13) Å. A Rietveld refinement is shown as a solid line through the data with the difference between the calculated and observed pattern shown below. Bragg markers for the primary $Sm_3Ag_4Sn_4$ phase (bottom) and the sample holder (top) are also shown.

Figure 5.4 shows the neutron diffraction pattern of $Sm_3Ag_4Sn_4$ taken in the paramagnetic state (50 K) at a wavelength of 2.37150(13) Å. As anticipated, the signal is quite weak, with the strongest structural peaks having a count rate of ∼100 cts hr^{-1}. Rietveld refinement of the pattern was achieved using GSAS [76] via the EXPGUI interface [77]. Analysis confirmed the structure and lattice parameters established by x-ray diffraction measurements. Although the 3 K diffraction pattern, shown at the top of Figure 5.5, shows no striking change from the paramagnetic state, a weak peak near $2\vartheta = 9°$ is visible above background. The magnetic scattering is isolated by taking the difference between the patterns at 3 and 50 K (middle curve in Figure 5.5) as described in Section 3.2.2, and we see that the only significant magnetic signal is associated with the 9° peak. The 9° peak which can be identified as being due to the (100) reflection in the *Immm* space group. The width of this peak is consistent with both the instrumental resolution function and the structural peaks at higher angles, leading us to conclude that long-ranged magnetic order is definitely established at 3 K in this compound. The *Immm* structure however does not allow reflections with $h+k+l$ being odd. We can conclude then that the magnetic structure must have a larger spatial periodicity than the crystallographic unit cell, and hence the Sm moments must be ordered antiferromagnetically as discussed in Section 3.2.2. Furthermore, the presence of this (100) peak indicates that the Sm moments have at least some component in the *bc*-plane.

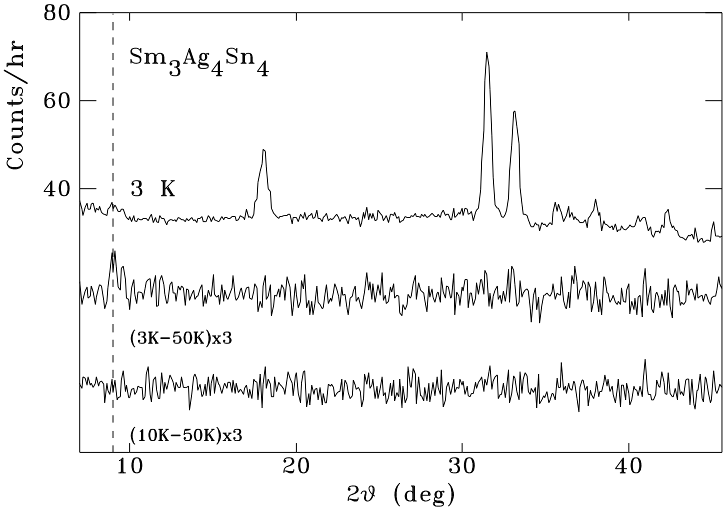

Figure 5.5: Top: neutron diffraction pattern for $Sm_3Ag_4Sn_4$ taken at 3 K showing a weak magnetic peak at $2\vartheta = 9°$ (dotted line). Middle: difference between the 3 and 50 K patterns (scaled by a factor of 3) to emphasize the magnetic peak. Bottom: difference between the 10 and 50 K patterns enlarged by the same factor of 3, showing no apparent magnetic signal. All measurements were made at a wavelength of 2.37150(13) Å.

The presence of the (100) peak also indicates that it is highly likely that the magnetic structure is commensurate with the crystallographic cell, and that the magnetic propagation vector is either (0,0,0) or (1,1,1). It is important to note that in the $Gd_3Cu_4Ge_4$-type structure, for both rare earth sites, the (1,0,0), (0,1,0), (0,0,1) and (1,1,1) propagation vectors are equivalent. The magnetic representations, computed using the SARAh [25] program are:

$$\Gamma_{mag-2d} = 1\Gamma_3 + 1\Gamma_5 + 1\Gamma_7 \tag{5.1}$$

and,

$$\Gamma_{mag-4e} = 1\Gamma_2 + 1\Gamma_3 + 1\Gamma_5 + 1\Gamma_6 + 1\Gamma_7 + 1\Gamma_8 \tag{5.2}$$

The two possible **k** vectors yield identical sets of IRs, and their basis vectors are listed in Table 5.1. As was stated in section 2.3.3, for body centered lattices, only half of the atoms are explicitly stated, and the remaining half which correspond to the body centering operation can be computed directly using Equation 2.9. In this case since the omitted atom's moment will either be parallel to the listed moment if **k**=(0,0,0), or anti-parallel if **k**=(1,1,1).

We may rule out Γ_2 and Γ_3 for both propagation vectors, as they only allow the 4e site to order along the crystal a-axis, incompatible with the observation of a magnetic (100) peak. As noted above, (100) scattering cannot result from ferromagnetic order, and previous magnetization measurements [33] have shown that $Sm_3Ag_4Sn_4$ exhibits antiferromagnetic order. Thus, we can also rule out the ferromagnetic groups Γ_5 and Γ_7 with **k**=(0,0,0).

Of the remaining candidate magnetic groups only two (Γ_6 and Γ_8 with $\mathbf{k} = (1,1,1)$) yield enough intensity on the (100) peak to be consistent with the data shown in Figure 5.5. Remarkably, neither of these groups permits magnetic ordering at the 2d site. In vast majority of $R_3T_4X_4$ compounds ordering on the 2d site is either the only form seen, or at least the preferred ordering, with the 4e sites ordering only at a much reduced temperature. If the Sm-4e sublattice is indeed the only one to order, this sets $Sm_3Ag_4Sn_4$ apart from all other members of the $R_3Ag_4Sn_4$ series.

IR	Basis	Atom	Re(a)	Re(b)	Re(c)	Im(a)	Im(b)	Im(c)
Γ_3	ψ_1	$(\frac{1}{2}, 0, \frac{1}{2})$	1	0	0	0	0	0
Γ_5	ψ_2	$(\frac{1}{2}, 0, \frac{1}{2})$	0	1	0	0	0	0
Γ_7	ψ_3	$(\frac{1}{2}, 0, \frac{1}{2})$	0	0	1	0	0	0
Γ_2	ψ_1	(x_R,0,0)	1	0	0	0	0	0
		($1 - x_R$,0,0)	-1	0	0	0	0	0
Γ_3	ψ_2	(x_R,0,0)	1	0	0	0	0	0
		($1 - x_R$,0,0)	1	0	0	0	0	0
Γ_5	ψ_3	(x_R,0,0)	0	1	0	0	0	0
		($1 - x_R$,0,0)	0	1	0	0	0	0
Γ_6	ψ_4	(x_R,0,0)	0	0	1	0	0	0
		($1 - x_R$,0,0)	0	0	-1	0	0	0
Γ_7	ψ_5	(x_R,0,0)	0	0	1	0	0	0
		($1 - x_R$,0,0)	0	0	1	0	0	0
Γ_8	ψ_6	(x_R,0,0)	0	1	0	0	0	0
		($1 - x_R$,0,0)	0	-1	0	0	0	0

Table 5.1: The basis vectors computed from the IRs of the $Immm$ space group for the Sm-2d and Sm-4e sites in $Sm_3Ag_4Sn_4$. The basis vectors listed are identical for the propagation vectors **k**=(0,0,0) and **k**=(1,1,1).

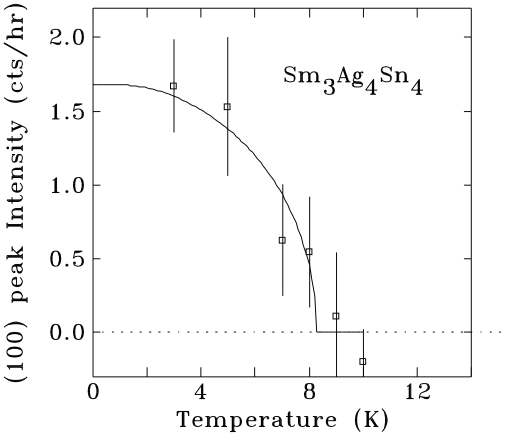

Figure 5.6: Temperature dependence of the intensity of the (100) reflection at $2\vartheta = 9°$. The solid line is a Brillouin function fit and the transition temperature derived from the fit, 8.3(4) K, is in excellent agreement with the moment reorientation temperature obtained from ^{119}Sn Mössbauer spectroscopy.

Tracking of the intensity of the (100) peak with temperature (Figure 5.6) shows that it disappears at 8.3(4) K, in perfect agreement with the reorientation temperature measured by ^{119}Sn Mössbauer spectroscopy. It is clear from the bottom curve in Figure 5.5 that no significant magnetic signal is observed at 10 K, despite clear evidence in the ^{119}Sn Mössbauer spectra that the compound remains ordered until 26 K. Simulation of the possible magnetic groups that support antiferromagnetic (AFM) ordering of the Sm moments reveals that only the two candidate groups for the low-temperature structure yield a strong magnetic signature; the others all lead to multiple weak magnetic peaks. As a result, our failure to detect magnetic scattering above 9 K does not lead to the conclusion that above 8.3(4) K the moments are disordered, but rather, when taken with the clear magnetic signal in the ^{119}Sn Mössbauer spectra, it implies a change in magnetic order, with the Sm moments rotating closer to the a-axis. The overall weakness of the magnetic scattering, and the absence of magnetic peaks at 10 K, preclude further analysis of the neutron diffraction data. The magnetic structure between 8.3 K and 26.0 K cannot be determined.

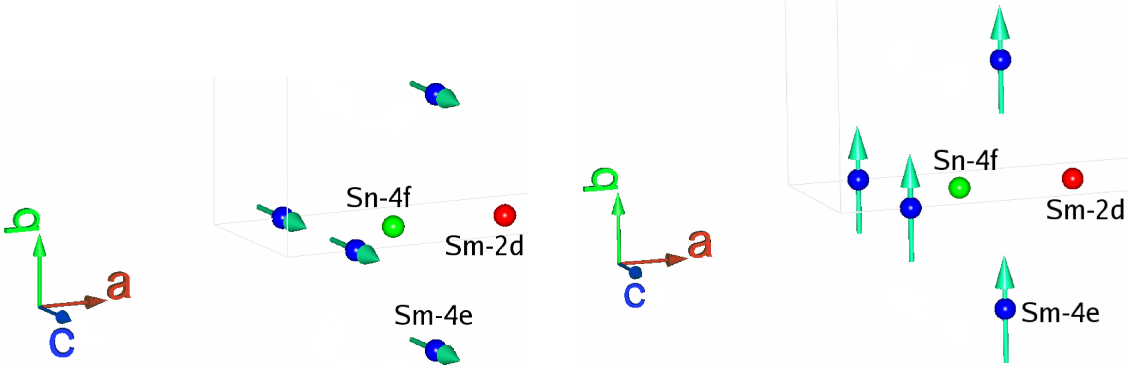

(a) Sm-2d (red) and Sm-4e (blue) neighbours to the Sn-4f (green) site in $Sm_3Ag_4Sn_4$ for the Γ_6 magnetic space group with $\mathbf{k} = (1, 1, 1)$.

(b) Sm-2d (red) and Sm-4e (blue) neighbours to the Sn-4f (green) site in $Sm_3Ag_4Sn_4$ for the Γ_8 magnetic space group with $\mathbf{k} = (1, 1, 1)$.

Figure 5.7: Sm-2d and Sm-4e neighbours to the Sn-4f site in $Sm_3Ag_4Sn_4$ for the Γ_6 and Γ_8 magnetic space groups with $\mathbf{k} = (1, 1, 1)$.

5.1.3 Combining the neutron scattering and ^{119}Sn Mössbauer data

^{119}Sn Mössbauer spectroscopy and neutron diffraction provide distinct, complementary information on the magnetic ordering in $Sm_3Ag_4Sn_4$ which can be used to differentiate between the possible magnetic space groups (Γ_6 along the c-axis or Γ_8 along the b-axis), and determine which is most likely adopted. The magnetic environments for the two possible magnetic space groups allowed by the neutron diffraction data are depicted in Figure 5.7 for the Sn-4f site, and Figure 5.8 for the Sn-4h site.

If we consider only the isotropic contribution to the transferred hyperfine field, neither magnetic group yields a transferred field at the Sn-4h site as the four Sm-4e first neighbours for this site consist of two antiparallel pairs, so their effects cancel (Figure 5.8). We must therefore include anisotropic contributions which consists of a vector sum of the projections of the moments onto the unit vectors directed along

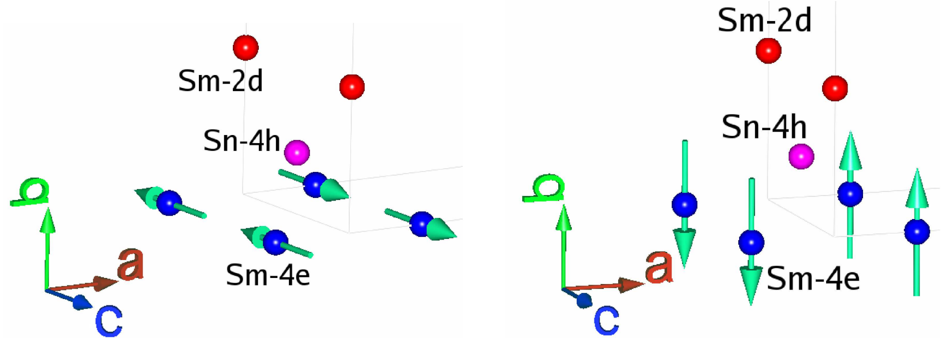

(a) Sm-2d (red) and Sm-4e (blue) neighbours to the Sn-4h (pink) site in $Sm_3Ag_4Sn_4$ for the Γ_6 magnetic space group.

(b) Sm-2d (red) and Sm-4e (blue) neighbours to the Sn-4h (pink) site in $Sm_3Ag_4Sn_4$ for the Γ_8 magnetic space group.

Figure 5.8: Sm-2d and Sm-4e neighbours to the Sn-4h site in $Sm_3Ag_4Sn_4$ for the Γ_6 and Γ_8 magnetic space group.

the Sn-rare earth bonds as described in Section 3.1.11.

As shown in Figure 5.7, both magnetic groups the isotropic contribution to the transferred hyperfine field at the Sn-4f site will be non-zero, pointing in the $+c$ direction for Γ_6 since all four Sm-4e moments point in that direction and likewise in the $+b$ direction for Γ_8. The anisotropic contribution is also non-zero for both magnetic groups. The situation at the Sn-4h site (Figure 5.8) is, however, quite different. As noted above, the isotropic contribution cancels for both possible groups. In addition, the anisotropic contribution is zero for the Γ_6 structure, with the result that only the Γ_8 structure yields a non-zero transferred hyperfine field at the Sn-4h site, and then only when the anisotropic contribution is taken into account. This also leads to the assignment of the higher field site in Figures 5.2 and 5.3(b) to the Sn-4f site which is reversed from all other $R_3T_4Sn_4$ compounds.

The ordered Sm moments of intermetallics typically deviates substantially from the $g_J \mu_B J$ value observed for most other rare earths. This is often attributed to

Compound	$\lvert\mu\rvert$ (μ_B)
$SmAl_2$	0.2
$SmIr_2$	0.2
$SmRh_2$	0.53
$SmNi_2$	0.25
$SmPt_2$	0.19

Table 5.2: Some experimentally obtained values of the ordered Sm moment in Sm intermetallic compounds (taken from [83] and the references therein).

a J-level mixing between the ground state of Sm^{3+} ($J = \frac{5}{2}$) and its first excited state ($J = \frac{7}{2}$), along with crystal electric fields [83]. The first excited state lies at only 120.6 meV (only Eu^{3+} is smaller at 43.1 meV), and the nearest is Nd^{3+} at 232.7 meV [84], and so this effect is most prominent in Sm and Eu compounds. Some examples of experimental values for the ordered Sm moment in intermetallic compounds are listed in Table 5.2 (taken from [83], and references therein).

Theoretical work by Adachi *et al.* [85] investigating the severely reduced (0.1 μ_B) ordered Sm moment in hcp Sm metal, found that in the moment due only to J-level mixing caused mainly by the exchange interaction to be about 0.54 μ_B. Only when crystal field interactions were taken into account did the expected moment reduce further to 0.1 μ_B. Rietveld refinement of the 3 K pattern, assuming that the Γ_8 structure is correct, yields a Sm moment of 0.47(10) μ_B on the Sm-4e site. (Note that both structures, Γ_8 and Γ_6, yield the same intensity for the (100) reflection, and the derived Sm moment is independent of this final choice).

Assuming that the magnetic order below 8 K in $Sm_3Ag_4Sn_4$ follows the Γ_8 structure, then we should observe a transferred hyperfine field at both Sn sites: Sn-4f along b and Sn-4h along a. If we further assume that V_{zz} is along one of the crystallographic axes for each Sn site, this analysis predicts that the angle between B_{hf} and V_{zz} should be $\vartheta = 90°$ at both Sn sites; however, this is not consistent with the results shown in Figure 5.3(b). Force-fitting $\vartheta = 90°$ at both sites yields extremely poor fits, and a grid search in both η and the polar angle ϕ did not lead to a better fit to the spectra than is shown in Figure 5.3(a). It is therefore likely that some subtlety of the transfer process is being missed. As neutron diffraction is unlikely to yield further information (samples prepared with a less absorbing Sm isotope would be smaller than the one employed here and so would not yield a better signal), the best way forward appears to be using single-crystal samples for ^{119}Sn Mössbauer spectroscopy, where the actual moment directions could be established directly.

5.2 $Sm_3Cu_4Sn_4$

Magnetic susceptibility and heat capacity data placed the ordering temperature at 8.79 K [29] which scales well with the de Gennes factor and the other $R_3Cu_4Sn_4$ compounds. However, the magnetic behaviour of $Sm_3Cu_4Sn_4$ turns out to be surprisingly different from not only the behaviour implied by the magnetic susceptibility measurements, but also that of $Sm_3Ag_4Sn_4$ and provides an example of a limitation inherent to neutron diffraction beyond the obvious, and quite severe problems caused by the highly absorbing Sm.

5.2.1 ^{119}Sn Mössbauer Spectroscopy

The ^{119}Sn Mössbauer spectrum at 1.6 K presents the usual two equal-area magnetic subspectra with fields of 6.97(1) T and 2.27(1) T (Figure 5.9). The spectra appearing at the bottom of Figure 5.11 (the 5 K and 1.56 K spectra) can be adequately fitted using the static hyperfine field model. A visual inspection of the ^{119}Sn Mössbauer spectra shown in Figure 5.11, however, reveals some unusual changes on heating: rather than simply moving together as the hyperfine field decreases with increasing temperature, the outer lines seem to broaden and become less distinct, while the central region fills in. This behaviour is confirmed by the use of the static field model for all temperatures leading to a steady increase in the linewidth with a steady decrease in the relative spectral area between the high and low field subspectra.

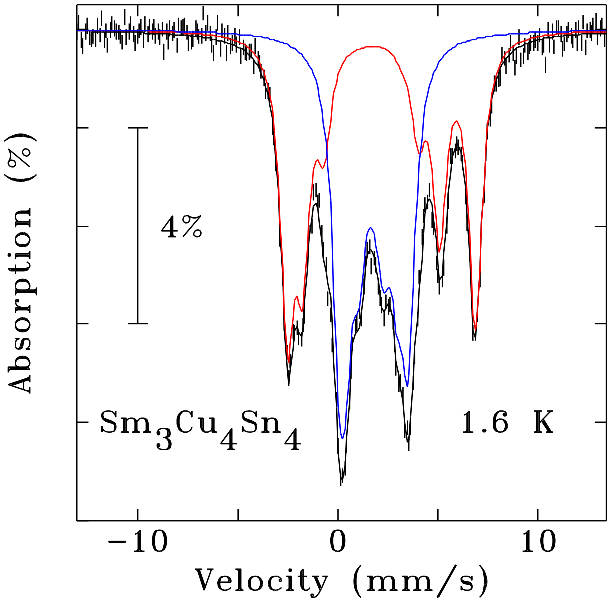

Figure 5.9: ^{119}Sn Mössbauer spectrum of $Sm_3Cu_4Sn_4$ acquired at 1.6 K.

A possible scenario that would produce this effect is that there is distribution of hyperfine magnetic environments around the Sn atoms in the structure. To model this behaviour, a pair of Gaussian distributions of hyperfine fields is assumed at each site. In this model we define an average field $\langle B_{hf} \rangle$, with a distribution width σ_B and construct each subspectrum as a sum of subspectra for which the spectral area follows a Gaussian distribution. This model yields adequate fits but the derived parameters do not follow expected trends. The temperature dependence of the hyperfine fields shows no apparent evidence of the three events previously identified at 9 K and below, and a magnetic splitting persists in the spectra until at least 40 K, well beyond any expected ordering temperature (Figure 5.10(a)). The fitted widths of the two distributions (Figure 5.10(b)) increase abruptly at about 5 K, and then decrease gradually above about 10 K. However it is the behaviour of the subspectral area, shown in Figure 5.10(c), that is unphysical. In all of the $R_3T_4Sn_4$ compounds studied up to this point, the spectra consist of two (or in one case, $Dy_3Ag_4Sn_4$ [38], three) subspectra with well defined areas that remain relatively stable as a function of temperature. This process fails here, and we see the low-field component becoming completely dominant as the distributions broaden. This behaviour corresponds closely to that described in Section 3.1.8, and implies the presence of slow moment dynamics rather than static long range order.

Fitting the spectra using a conventional dynamic up/down relaxation model (described in Section 3.1.8) yields good results for $T > 6$ K, however below this, the fitted fluctuation rates are so slow as to be effectively static and a static model was used for the lowest temperatures (Figure 5.11). It is important to note that the change in model used at low temperatures is solely for operational convenience and is based on the observation that the fluctuation rates are too slow to be resolved. It does not necessarily mean that the Sm moments are actually static. The trend in relaxation rates shown in Figure 5.12 shows a fairly steady decline on cooling and it is likely that this trend continues once it passes below our ability to resolve it.

5.2.2 Neutron Diffraction

The neutron diffraction pattern, measured using the flat-plate sample holder described in Section 3.2.4 and used for $Sm_3Ag_4Sn_4$, shows no change with decreasing temperature (Figure 5.13). Indeed, the difference between the 3 K and 20 K patterns consists only of statistical fluctuations, and appears more consistent with a paramagnetic state at 3 K.

The observation of an effectively static ordered state in the ^{119}Sn Mössbauer spectra without any sign of order in the neutron diffraction pattern is a result of the very different ways in which the two techniques detect magnetism. Mössbauer spectroscopy provides information on the immediate surroundings of the probe nucleus during the fraction of a microsecond over which the γ-nuclear interactions occur. As long as the

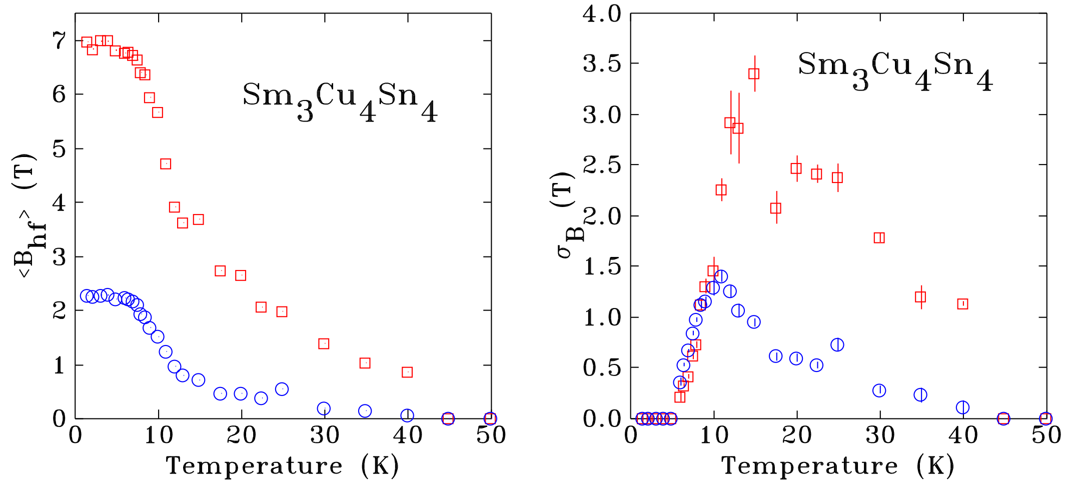

(a) Temperature dependence of the fitted average hyperfine magnetic field with a Gaussian field distribution model.

(b) Temperature dependence of the width of the hyperfine magnetic field Gaussian distribution σ_B.

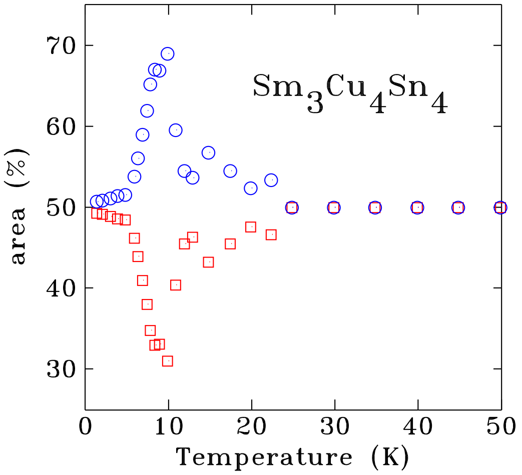

(c) Temperature dependence of the spectral area of each component in the Gaussian field distribution model.

Figure 5.10: The temperature dependence of the key fitted parameters obtained with a Gaussian field distribution model.

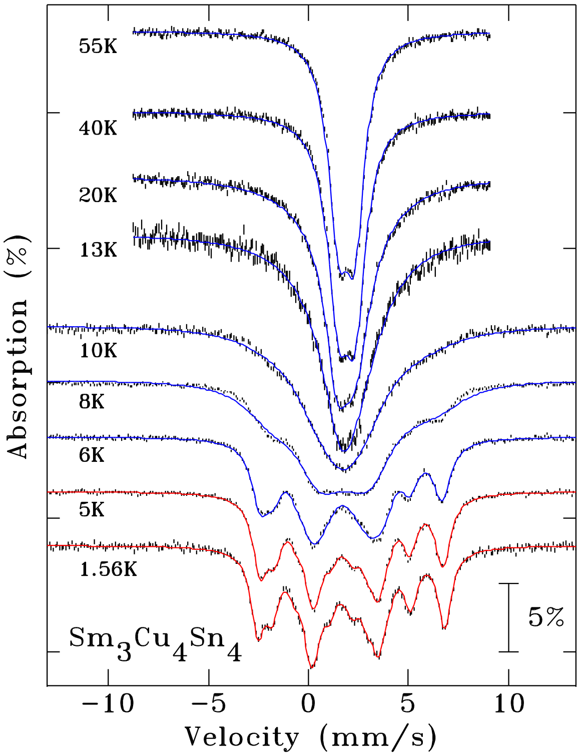

Figure 5.11: ^{119}Sn Mossbauer spectra of $Sm_3Cu_4Sn_4$ at selected temperatures. Solid lines are the result of dynamic fits (blue) for T>6 K, and static fits (red) for T<5 K (see text).

magnetic environment does not change during that time, the experiment yields an effectively static pattern. By contrast neutron diffraction only yields magnetic peaks when the moments are both static, since the interaction is essentially instantaneous, and spatially organized. The results of our measurements on $Sm_3Cu_4Sn_4$ suggest that this system does not exhibit long-range magnetic order above 3 K.

5.3 Conclusions

The ^{119}Sn Mössbauer spectroscopy measurements on $Sm_3Ag_4Sn_4$ clearly demonstrate the technique's sensitivity to magnetic order beyond what can be obtained from either

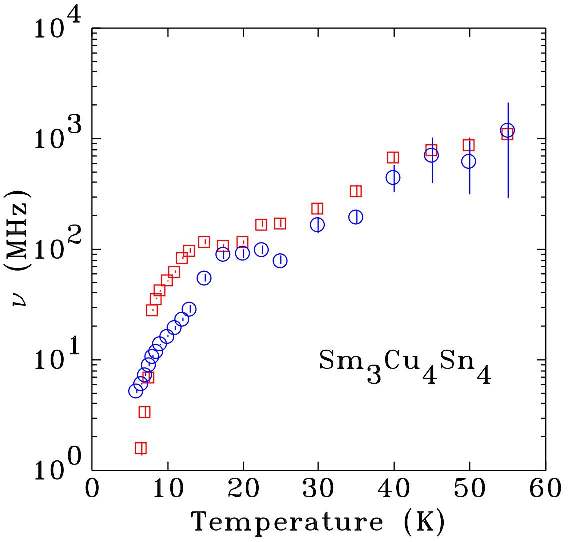

Figure 5.12: Temperature dependence of the fluctuation rates for the dynamic fits to the ^{119}Sn Mössbauer spectra of $Sm_3Cu_4Sn_4$. Above 40 K the fluctuation rates are so high that the spectra exhibit motional narrowing and can be fitted equally well using a static paramagnetic doublet, while below 6 K, the fluctuations are too slow to be resolved, and the spectra present as statically ordered.

neutron diffraction or bulk magnetization measurements, both of which are more sensitive to the reorientation of the moments than to the primary ordering. The understanding of the low temperature magnetic phase can only be achieved through a highly effective combination of neutron diffraction and Mössbauer spectroscopy, where each technique in isolation provides only incomplete information. In fact, as the (100) peak is quite weak, having the ^{119}Sn Mössbauer spectroscopy data allowed a more targeted search in temperature for the neutron diffraction experiments, without which the magnetic signature might have been missed.

The dynamic behaviour the Sm moments in $Sm_3Cu_4Sn_4$ is precisely in the sensitivity range of ^{119}Sn Mössbauer spectroscopy and does not yield a strong and clear signal with other experimental techniques. Although the neutron diffraction results are completely consistent with the ^{119}Sn Mössbauer spectroscopy results, without the

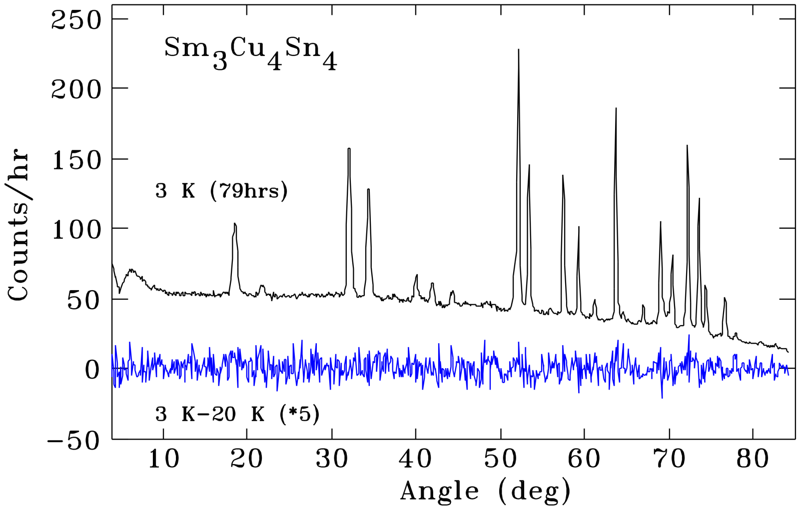

Figure 5.13: Top: Neutron diffraction pattern for $Sm_3Cu_4Sn_4$ taken at 3 K showing clearly resolved nuclear peaks, but no apparent magnetic scattering. Bottom: Difference between the 3 K and 20 K patterns (scaled by a factor of 5) to emphasize the absence of magnetic scattering. Measurements were made at a wavelength of 2.3715 Å.

latter, hardly any conclusions could be drawn at all.

As stated above, the $Sm_3Cu_4Sn_4$ and $Sm_3Ag_4Sn_4$ were thought to scale well with the de Gennes factor within their respective $R_3T_4X_4$ series, yet it is clear and unambiguous, even from the ^{119}Sn Mössbauer spectroscopy results alone, that this is not the case, and the Sm compounds significantly defy expectations.

Chapter 6

Gd Compounds

The Gd compound in a rare earth series is often of highest interest as it is expected to have the highest ordering temperature, due to the Gd maximal de Gennes factor, and is largely immune to crystal fields interactions due to its spherical ($L = 0$) ground state [86]. These properties make the Gd members of rare earth compound series the reference for the de Gennes scaling of the series and making an accurate determination of their magnetic properties of capital importance.

Compounds with a high Gd content however, suffer from even more severe absorption than Sm compounds in neutron diffraction experiments, consequently neutron diffraction experiments on these compounds are often skipped. The Gd compounds in the $R_3T_4X_4$ series are at the root of the observed failure of de Gennes scaling, and lead to the consideration of exotic ordering mechanisms to explain the failure. It will be demonstrated in this chapter through the use of ^{119}Sn and ^{155}Gd Mössbauer spectroscopy and flat-plate neutron diffraction, that the ordering temperature of $Gd_3Ag_4Sn_4$ and $Gd_3Cu_4Ge_4$ are more than twice as high as originally thought. $Gd_3Ag_4Sn_4$ actually follows de Gennes scaling quite well, and it is the $Gd_3Cu_4Sn_4$ and $Gd_3Cu_4Ge_4$ compounds that remain as outliers.

The use of ^{119}Sn Mössbauer spectroscopy in $Gd_3Ag_4Sn_4$ and $Gd_3Cu_4Sn_4$ is similar to that which has been presented in the previous two chapters. As discussed in

Section 3.1.10 ^{155}Gd Mössbauer spectroscopy is different in one important respect: the field measured at ^{155}Gd nuclei is due to the Gd moment directly, and is not merely transferred from other species in the compound. Moreover, the crystallographic populations of each Gd site in the compounds considered here are not equal. The 2:1 population ratio between the Gd-4e and Gd-2d sites leads to the expectation that ^{155}Gd Mössbauer spectra will consist of two subspectra with a 2:1 area ratio. Each sublattice can then be associated directly to a hyperfine environment. ^{155}Gd Mössbauer spectroscopy presents however, a different challenge in determining the hyperfine environment at the Gd sites. In a typical ^{155}Gd Mössbauer spectrum the line overlap, even at high fields, is far more severe than in a ^{119}Sn Mössbauer spectrum for which the lines are mostly well resolved. An appropriate model can still be determined however, since even the overall shape of the spectrum is intimately linked to the hyperfine environment.

The point symmetries of the Gd-2d and Gd-4e sites, mmm and $2mm$ respectively, lead to the conclusion (like the point symmetries of the Sn-4f and Sn-4h sites discussed in the previous chapters) that the principal axis of the electric field gradient, V_{zz}, points along one of the crystallographic axes for each site. The point symmetries do not exclude the possibility of an asymmetry η to the electric field gradient. ^{170}Yb Mössbauer spectroscopy measurements on $Yb_3Cu_4Ge_4$ established that for this compound the R-2d site exhibit a large electric field gradient asymmetry [40]. Preliminary ^{170}Yb Mössbauer spectroscopy results on $Yb_3Cu_4Si_4$, indicate similar behaviour. Since the compound adopts the same $Gd_3Cu_4Ge_4$-type structure, it is likely that the Gd-2d sites in the compounds studied here exhibit a similar asymmetry. We thus set the $\eta = 1$ for the Gd-2d site and $\eta = 0$ for the Gd-4e, and the quality of fit will determine whether this model is consistent with the measurements. Some of the results presented in this section can also be found in print elsewhere [79, 87].

6.1 $Gd_3Cu_4Ge_4$

$Gd_3Cu_4Ge_4$ was the first of the $R_3T_4X_4$ systems to be studied and lends its name to the structure type. As described in section 2.4, different magnetic transition temperatures can be found in the literature (heat capacity: 8.5 K [40], magnetic susceptibility: 11 K [42], magnetization: 12 K [43]), and all three values inconsistent with de Gennes scaling in the $R_3Cu_4Ge_4$ compound series. The ^{155}Gd Mössbauer spectra of $Gd_3Ag_4Sn_4$ were collected using the cold source setup described in section 3.1.10

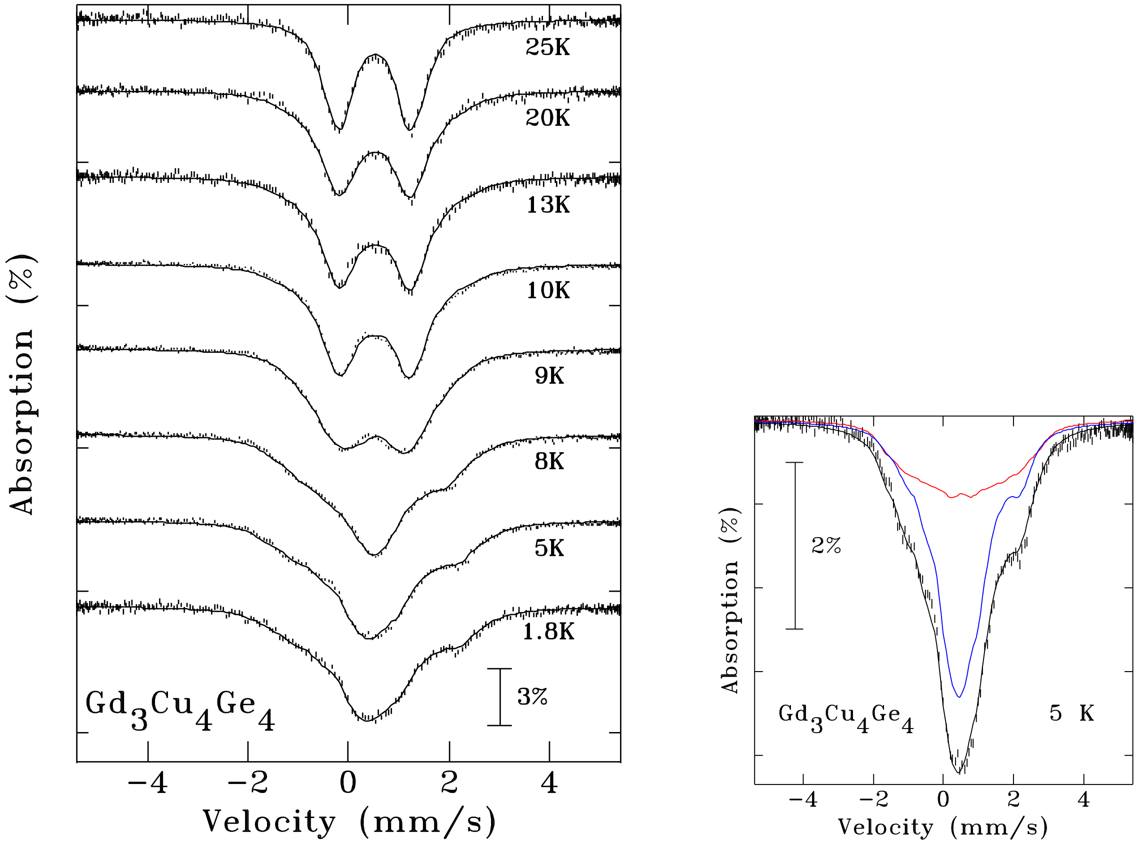

Figure 6.1: Left: ^{155}Gd Mössbauer spectra of $Gd_3Cu_4Ge_4$. Right: ^{155}Gd Mössbauer spectrum of $Gd_3Cu_4Ge_4$ collected at 5 K, the Gd-2d site subspectrum is shown in red, the Gd-4e subspectrum is shown in blue.

The ^{155}Gd Mössbauer spectra of $Gd_3Cu_4Ge_4$ are shown in Figure 6.1, and a magnetic splitting persists up to 25 K. The ^{155}Gd Mössbauer spectrum of $Gd_3Cu_4Ge_4$ acquired at 5 K is shown on the right of Figure 6.1. The spectrum is fitted with two subspectra with an area ratio of 2:1, allowing the distinction between the Gd-2d (component shown in red) and Gd-4e (component shown in blue) contributions. The Gd-4e component yields an angle ϑ of 90° between the principal axis of the electric field gradient and the magnetic field, while the Gd-2d component yields a magnetic field that makes an angle of 20° with V_{zz}. It is important to note that the principal axis of the electric field gradient at the Gd-2d site does not necessarily point in the same crystallographic direction as the principal axis of the electric field gradient at the Gd-4e site. The fits to the magnetic pattern also indicate that V_{zz} is negative at the Gd-2d site and is consistent with a highly asymmetric electric field gradient, while V_{zz} is positive at the Gd-4e site and the electric field gradient is axially symmetric. A fit to the 25 K pattern (in the paramagnetic phase), yields eQ_gV_{zz} (e is the electronic charge, and Q_g is the nuclear quadrupole moment of the ground state nucleus) values of $-3.33(3)$ mm/s at the Gd-2d site and $+2.74(2)$ mm/s at the Gd-4e site.

The temperature dependence of the fitted hyperfine magnetic field, shown on the left of Figure 6.2 shows how the Gd-2d and Gd-4e sublattices appear to order at the same temperature of 25.0(8) K. As we lower the temperature though, the field at the Gd-2d site grows to saturation far sooner than the field at the Gd-4e site. The field at the Gd-4e only truly begins to rise below 9.6(3) K. This indicates that it is more likely that the Gd-2d moments order at 25.0(8) K whereas the Gd-4e moments are either partially, or weakly ordered. The severe line overlap observed in the magnetic ^{155}Gd Mössbauer spectroscopy data, makes distinguishing the phases difficult at low fields, and consequently the relatively low field observed at the Gd-4e site above 9.6 K could be a fitting artefact. A complete resolution of these issues will require neutron diffraction measurements.

A $J = \frac{1}{2}$ Brillouin function fits the data far better than the expected $J = \frac{7}{2}$ Brillouin function, as was observed in the $Ho_3Cu_4Sn_4$ ^{119}Sn Mössbauer spectroscopy data. These data demonstrate that $Gd_3Cu_4Ge_4$ is yet another case where an ordering temperature is mislabeled due to the primary ordering event yielding a weak or absent signal in bulk magnetic measurements.

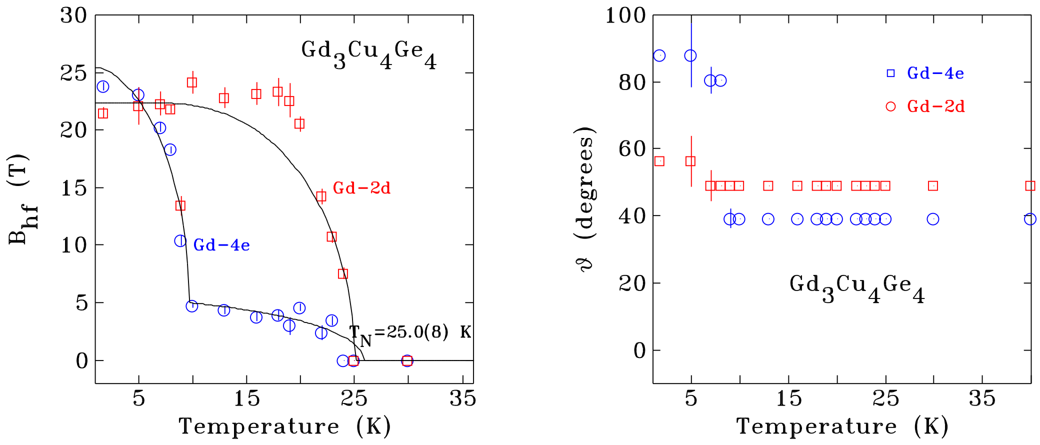

Figure 6.2: Left: Temperature dependence of the hyperfine magnetic field obtained from ^{155}Gd Mössbauer spectroscopy at the Gd-2d (red) and Gd-4e (blue) sites. A $J = \frac{1}{2}$ Brillouin function yields a transition temperature of 24.0(2) K for the Gd-2d site and a transition temperature of 10.1(2) K for the Gd-4e site. Right: Temperature dependence of the fitted angle ϑ between the hyperfine magnetic field and the principal axis of the electric field gradient obtained from ^{155}Gd Mössbauer spectroscopy.

Using the transition temperature for $Gd_3Cu_4Ge_4$ found via ^{155}Gd Mössbauer spectroscopy, the transition temperatures of the $R_3Cu_4Ge_4$ compounds still does not follow de Gennes scaling law (Figure 6.3), although the gap is somewhat narrowed.

6.2 $Gd_3Ag_4Sn_4$

The ac susceptibility (χ') for $Gd_3Ag_4Sn_4$ (Figure 6.4) exhibits a marked downturn at about 8 K, which has previously been attributed to the onset of AF order [33]. A fit of the higher temperature data yields an effective moment of 8.16(4) μ_B and a Curie-Weiss temperature (θ_p) of $-50(2)$ K, consistent with the value of -54 K re-

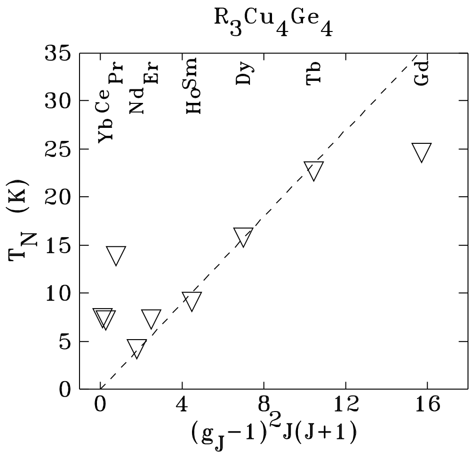

Figure 6.3: The highest magnetic transition temperatures in the $R_3Cu_4Ge_4$ (▽) compounds plotted versus the de Gennes factor $(g_J - 1)^2 J(J + 1)$ if we use the value for T_N found by ^{155}Gd Mössbauer spectroscopy for the Gd compound [8, 35, 39, 40, 41].

ported previously [33], and reflecting the dominance of antiferromagnetic interactions common to the $R_3T_4X_4$ family of compounds.

No changes in $\chi'(T)$ are apparent other than the feature at 8 K. In particular, there is no direct evidence for the actual onset of long-range magnetic order near 29 K (see below). There is a change in χ'', the out-of-phase response (shown as an inset to Figure 6.4) near 30 K, however it is difficult to argue that this is a real signature of ordering in $Gd_3Ag_4Sn_4$ without using previous knowledge of the actual transition temperature as justification. In addition, no such feature is seen for $Gd_3Cu_4Sn_4$ (discussed below).

6.2.1 ^{119}Sn Mössbauer

It is immediately clear from the spectra shown in Figure 6.5 that magnetic order is present well above the 8 K ordering temperature inferred from the χ' data shown in Figure 6.4. Spectra up to at least 27 K clearly show magnetic splitting. No significant (<2%) impurity contribution was detected at any temperature, so the

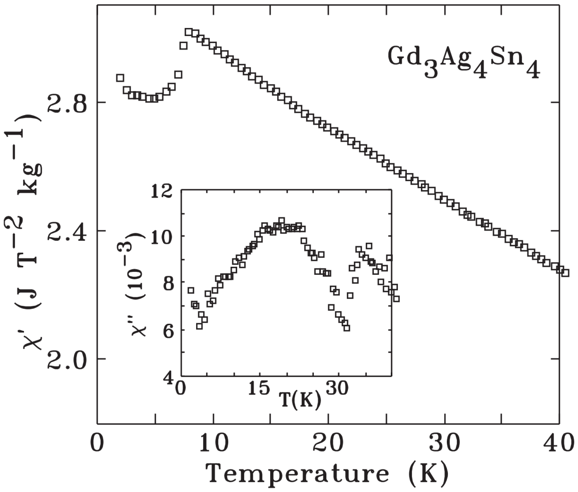

Figure 6.4: ac susceptibility data (χ') for $Gd_3Ag_4Sn_4$ in a 1 mT ac field at 337 Hz. The inset shows the out-of-phase signal (χ''), which provides the only evidence of the bulk transition near 30 K.

behaviour observed here using ^{119}Sn Mössbauer spectroscopy undoubtedly reflects bulk ordering of the primary phase.

The $Gd_3Ag_4Sn_4$ spectrum at 2.3 K in Figure 6.6 consists of two equal-area magnetic patterns with different hyperfine fields (9.11(3) and 4.52(3) T) consistent with the crystallographic populations of the Sn-4f and Sn-4h sites. Both patterns exhibit significantly broadened lines (FWHM of 1.16(4) mm/s at 2.3 K compared with 0.55(2) mm/s at 30 K) and this broadening decreases with increasing temperature as the magnetic splitting is lost. This evolution in linewidth suggests that there is an unresolved distribution of hyperfine fields ($\delta B_{hf}/B_{hf} \sim 10\%$) at each of the Sn sites resulting from a complex ordering of the Gd moments. It is important to note a significant difference between the broadened $Gd_3Ag_4Sn_4$ spectra considered here and the broadened $Sm_3Cu_4Sn_4$ spectra discussed in Chapter 5: the spectral areas for $Gd_3Ag_4Sn_4$ maintain their 1:1 ratio at all temperatures and the broadening decreases with temperature, allowing us to rule out magnetic moment relaxation.

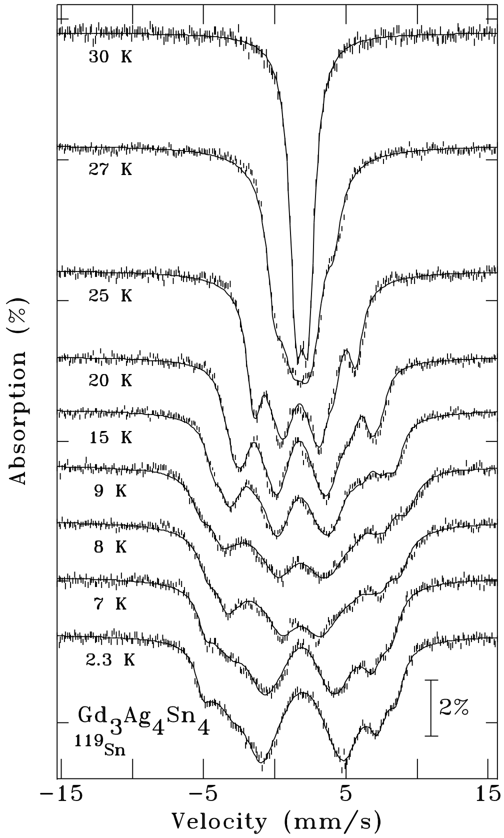

Figure 6.5: Temperature dependence of the ^{119}Sn Mössbauer spectra of $Gd_3Ag_4Sn_4$. There is a clear magnetic contribution to the spectra well above the previously assigned magnetic ordering temperature of 8 K.

A fit to the temperature dependence of B_{hf} at each of the two sites with a $J = \frac{7}{2}$ Brillouin function to obtain an average Néel temperature (T_N) of 28.8(2) K for $Gd_3Ag_4Sn_4$. As noted above, there is no clear signature in $\chi'(T)$ (Figure 6.4) associated with this bulk ordering transition. Further examination of $B_{hf}(T)$ reveals a marked change in the temperature dependence of both components below 9 K, with the high-field component showing an initial decrease and the lower-field component increasing. The decrease in the field strongly implies a magnetic structure transition from a magnetic structure above 9 K in which some of the Gd are collinear, to a structure below 9 K in which those same moments cancel.

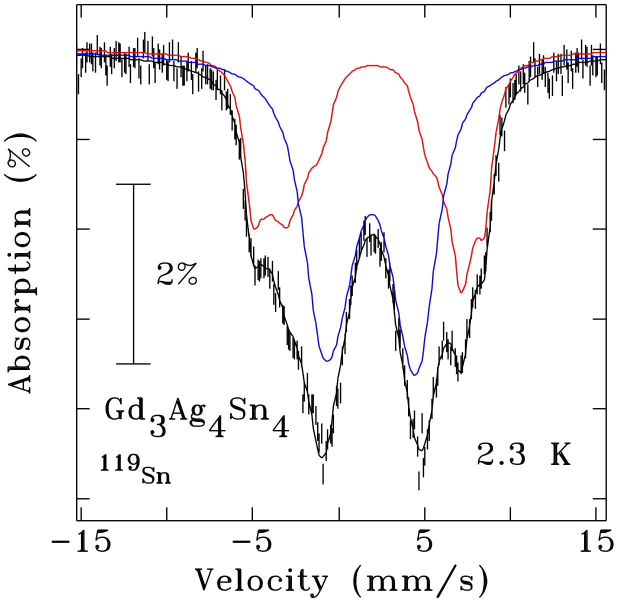

Figure 6.6: The two equal-area subspectra used to fit the 2.3 K ^{119}Sn Mössbauer spectrum of $Gd_3Ag_4Sn_4$.

The broad lines and significant line overlap present at all temperatures effectively preclude detailed analysis using a full Hamiltonian solution. However, if we assume that a first-order solution is adequate, and treat the electric field gradient V_{zz} as being axially symmetric (the resolution issues preclude a determination of η), then we can define a quadrupole shift:

$$\epsilon = \frac{eQ_eV_{zz}}{4}(3\cos^2\vartheta - 1) \tag{6.1}$$

where ϑ is the angle between V_{zz} and B_{hf} . ϵ represents the projection of V_{zz} onto B_{hf} at each of the two Sn sites. Plotting the temperature dependence of this projection, shown on the right of Figure 6.7 reveals evidence for a change in field direction below 8 K in addition to the changes in B_{hf} apparent on the left of Figure 6.7. The change in ϵ is close to a factor of -2 at both Sn sites. This is best seen at the high-field site, where line overlap is less severe and the fits are more reliable: ϵ changes from $\sim$+0.6 mm/s above 8 K to ~ -0.3 mm/s below 8 K. This change suggests that there is

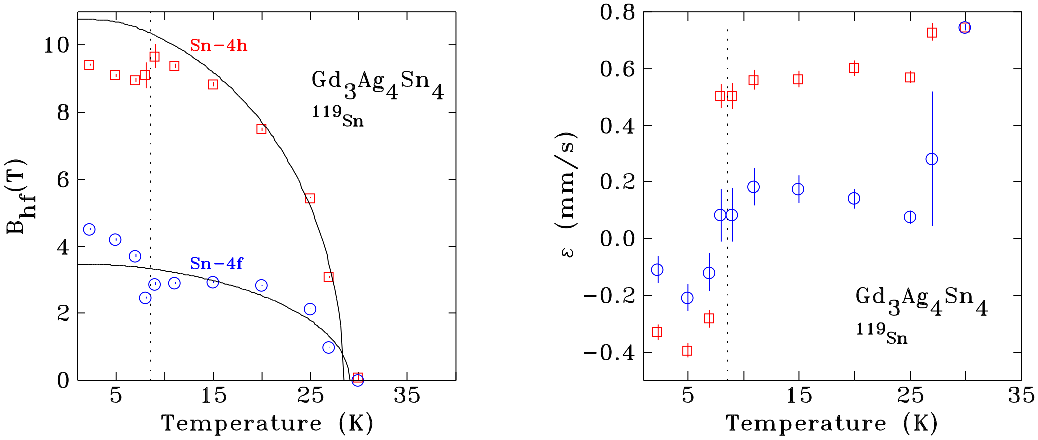

Figure 6.7: Left: Temperature dependence of the fitted transferred hyperfine magnetic field in $Gd_3Ag_4Sn_4$ clearly indicating the onset of magnetic order at 28.8(2) K. The reorientation temperature is indicated by the dotted line. Right: Temperature dependence of the fitted ϵ in $Gd_3Ag_4Sn_4$.

a 90° change in the orientation of the hyperfine field at the two Sn sites. This analysis leads to the conclusion that the 8 K feature in $\chi'(T)$ that was originally identified as the ordering temperature [33] actually marks a spin reorientation transition.

In light of these results, neutron diffraction measurements were performed on $Gd_3Ag_4Sn_4$ using the flat-plate sample mounting described in section 3.2.4 [88]. At 3 K, both the Gd-2d and Gd-4e sublattices adopt antiferromagnetic structures with the moments oriented parallel to the *c*-axis. The Gd-2d structure is incommensurate, while that of the Gd-4e moments is commensurate with the crystal lattice. Analysis of the Sn environments implied by the fitted magnetic structures provides confirmation of the derived structures. Both the Sn-4h and the Sn-4f sites each have four Gd-4e neighbours, and at 3 K these are arranged as two anti-parallel pairs, so their net influence at the two Sn sites should cancel, as shown on the left of Figure 6.8. The two Gd-2d moments near the Sn-4h site are parallel while the Sn-4f site has a single Gd-2d neighbour leading to an expected 2:1 hyperfine field ratio (as noted in the $Ho_3Cu_4Sn_4$ and $Nd_3Cu_4Sn_4$ cases). This prediction is in excellent agreement with the observed ratio of 2.02(2):1 at 2.3 K.

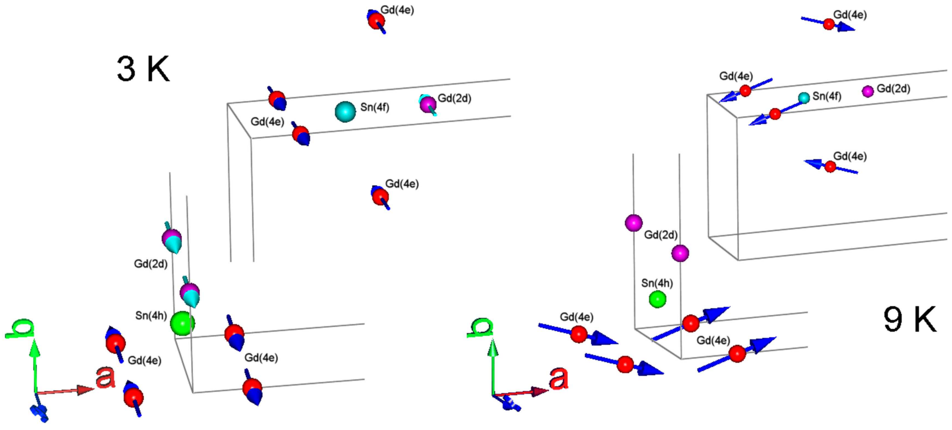

Figure 6.8: Magnetic environments of the two Sn sites in $Gd_3Ag_4Sn_4$ at 3 K (left) and 9 K (right) derived from fits of the neutron diffraction data. Note: No moments are shown for the Gd-2d sites at 9 K as a complete description of their order above the reorientation temperature could not be determined.

Above 9 K, the Gd-4e moments reorient onto the *ab* plane and adopt a magnetic structure that is doubled along the *b*-axis and has the moments tilted by ∼20° from the *a*-axis. The Gd-2d sublattice remains incommensurate but the weak signal and limited number of distinct reflections precludes a more detailed analysis [88]. Above the spin reorientation (shown as 9 K in Figure 6.8) the Gd-4e contributions now add at the Sn-4h site and partially cancel at the Sn-4f site. This leads to Gd-4e contributions at both Sn sites. If we consider only the effects of the Gd-4e moments, then we find that the transferred fields at the Sn sites rotate by 90° (from along the *c*-axis at 3 K to along the *a*-axis at 9 K) consistent with the factor of -2 change in the quadrupole shift (ϵ) on the right of Figure 6.7, but the predicted field ratio remains at 2:1 and does not correspond well with the observed 3.4:1 ratio. The change in field ratio means that the Gd-2d continue to contribute to the net transferred hyperfine fields above the reorientation temperature. However, in order for the Gd-2d moments to have a significant impact on the total transferred hyperfine fields at the two Sn sites, they must be at least close to parallel to the Gd-4e moment directions: i.e. they must also undergo a 90° reorientation along with the Gd-4e moments. The strength of the Gd-Gd exchange interactions implied by the 28.2(2) K ordering temperature coupled with the weak anisotropy typical of Gd^{3+} moments (due to its immunity to crystal electric field effects) makes it reasonable to expect that the two sublattices rotate together. Although many Gd-2d moment configurations could be consistent with the observed increase in the transferred hyperfine field ratio, the change in hyperfine field direction and the increase in field ratio both suggest that the Gd-2d moments follow rotation from the *c*-axis to the *ab* plane of the Gd-4e moments on heating through 9 K. Thus the combination of neutron diffraction and ^{119}Sn Mössbauer spectroscopy leads naturally to a self consistent description of the magnetic order in $Gd_3Ag_4Sn_4$ below the 9 K spin reorientation and of the Gd-4e order above 9 K, and strongly implies a likely magnetic structure for the Gd-2d moments above 9 K. In order to confirm this magnetic behaviour and determine conclusively the behaviour of the Gd-2d moments, we turn to ^{155}Gd Mössbauer spectroscopy.

6.2.2 ^{155}Gd Mössbauer Spectroscopy

The ^{155}Gd Mössbauer spectra of $Gd_3Ag_4Sn_4$ were collected using the cold source setup described in section 3.1.10 and used for $Gd_3Cu_4Ge_4$.

The left of Figure 6.9 shows the ^{155}Gd Mössbauer spectra collected for this study. All were successfully fitted with two spectral components having a 2:1 area ratio, consistent with the crystallographic sites for Gd (Gd-2d and Gd-4e). The spectra also confirm the transition temperature inferred from both ^{119}Sn Mössbauer spectroscopy and neutron diffraction. The magnetic spectra can be fitted with a negative V_{zz} with a high asymmetry for the Gd-2d site, and a positive V_{zz} with no asymmetry for the Gd-4e site. Using the ^{155}Gd Mössbauer spectroscopy data in the paramagnetic phase we obtain eQ_gV_{zz} values of $-2.2(2)$ mm/s for the Gd-2d site and $+2.32(9)$ mm/s for

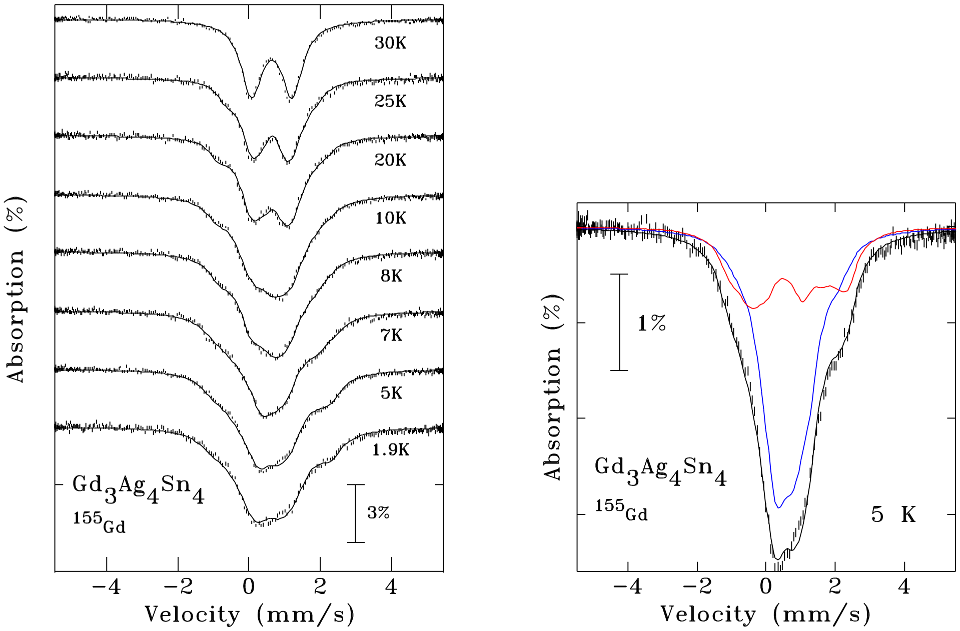

Figure 6.9: Left: ^{155}Gd Mössbauer spectra collected from $Gd_3Ag_4Sn_4$. Right: ^{155}Gd Mössbauer spectrum of $Gd_3Ag_4Sn_4$ collected at 5 K, the Gd-2d site subspectrum is shown in red, the Gd-4e subspectrum is shown in blue.

the Gd-4e site.

The right of Figure 6.9 shows the ^{155}Gd Mössbauer spectrum collected at 5 K (below the moment reorientation temperature). The pattern can be fitted with two subspectra with a 2:1 area ratio, again consistent with the crystallographic sites of Gd. The Gd-2d component (shown in red) has a field of 24.8(4) T that is parallel to V_{zz}, whereas the Gd-4e site (blue) has a field of 23.1(3) T orthogonal to V_{zz}, i.e. $\vartheta = 90°$. ^{155}Gd Mössbauer spectroscopy does not directly yield field directions in terms of the crystal lattice. However, the point symmetry of the two Gd sites (*mmm* for Gd-2d and 2*mm* for Gd-4e) implies that V_{zz} is along one of the crystallographic axes for each Gd site; thus the Gd-2d and Gd-4e moments also point along one of the crystallographic axes.

From the left of Figure 6.9, we can see that the lower tip of the pattern which

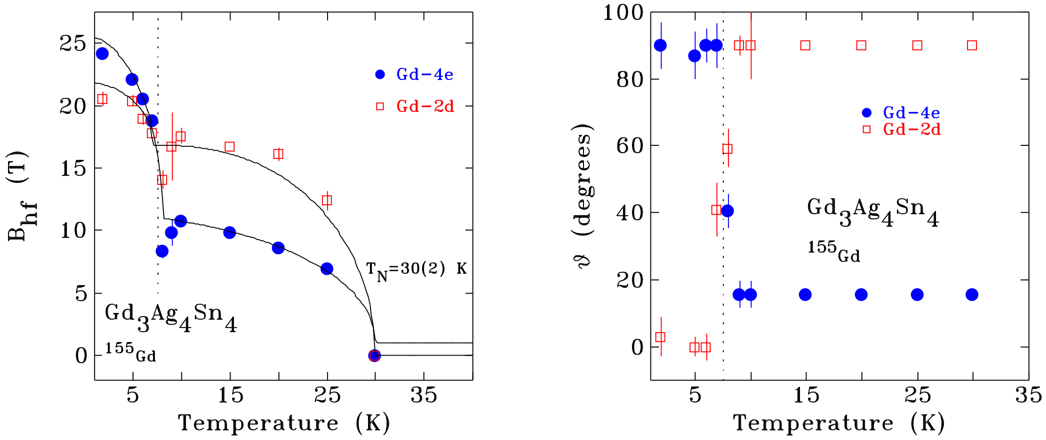

Figure 6.10: Left: Temperature dependence of the fitted hyperfine field in the ^{155}Gd Mössbauer spectroscopy data of $Gd_3Ag_4Sn_4$. Right: Temperature dependence of the fitted angle ϑ between the hyperfine field and the principal axis of the electric field gradient in the ^{155}Gd Mössbauer spectroscopy data of $Gd_3Ag_4Sn_4$.

points to left in the 7 K pattern switches rather abruptly to the right at 8 K, i.e. the visual asymmetry of the pattern is reversed. This type of shift often indicates a change in ϑ, and it can be seen from the right of Figure 6.10 that indeed the Gd-2d moments undergo a 90° reorientation, whereas the Gd-4e moments undergo a 75° rotation.

6.2.3 Combining Measurements On $Gd_3Ag_4Sn_4$

The combination of the results from each experimental technique provides a complete picture of the Gd moment behaviour in $Gd_3Ag_4Sn_4$. The ^{119}Sn Mössbauer spectroscopy data clearly indicate that the primary ordering occurs at 28.8(2) K. Moreover, the transferred field at both Sn sites undergoes a 90° rotation. The 2:1 transferred hyperfine field ratio obtained by ^{119}Sn Mössbauer spectroscopy below 8 K is consistent with the Gd-2d and Gd-4e magnetic structures obtained by neutron diffraction since the Gd-4e moments are anti-parallel around both Sn sites and cancel, leaving only a single Gd-2d moment around the Sn-4f site, and 2 parallel Gd-2d moments around the Sn-4h site.

Even though neutron diffraction cannot resolve the Gd-2d order above 8 K, ^{119}Sn Mössbauer spectroscopy combined with the Gd-4e magnetic structure obtained by neutron diffraction leads to the conclusion that the Gd-2d moments must undergo a 90° rotation as the temperature is raised through 8 K. It is a clear and robust confirmation of our method that the ^{155}Gd Mössbauer indicates a 90° rotation of the Gd-2d moments as well as confirming the rotation of the Gd-4e moments from a $\sim 20°$ angle to 90° also consistent with neutron diffraction results.

These results demonstrate the power, and often the necessity of a combination of direct probes of magnetism in order to describe and understand the magnetic order of rare earth compounds.

6.3 $Gd_3Cu_4Sn_4$

Figure 6.11 shows χ'(T) for $Gd_3Cu_4Sn_4$. The behaviour is quite similar to that seen for $Gd_3Ag_4Sn_4$ (Figure 6.4), and a fit of $1/\chi'$ versus temperature yields a θ_p of $-59(1)$ K, suggesting slightly stronger AF interactions. The fit also yields a paramagnetic Gd moment of $\mu_{eff} = 8.00(4)\ \mu_B$, close to the free-ion moment of 7.94 μ_B. There is a broad feature centered near 8 K with some structure evident at lower temperatures, suggesting an ordering temperature of about 8 K. However, specific heat measurements place the bulk ordering temperature at about 13 K [34], in a region where no marked changes in χ'(T) are apparent. No significant features could be found in χ''(T). However, closer examination of the ac-susceptibility data reveals a slight change in slope (emphasized by plotting $d\chi'/dT$ on Figure 6.11) above 12 K.

The temperature derivative of χ'(T) also show two marked peaks, at 7.9(1) K and 6.4(1) K, that are consistent with events reported in heat capacity (C_p) data (at 8.2 K and 6.5 K) [34]. The entropy of the 8 K event is comparable to that associated with

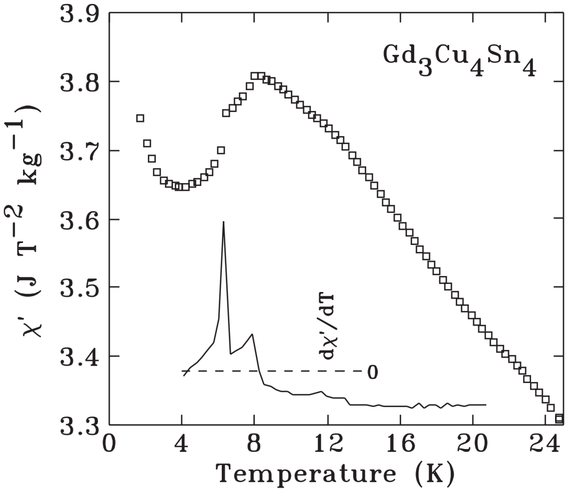

Figure 6.11: ac susceptibility (χ') for $Gd_3Cu_4Sn_4$ at 337 Hz in a drive field of 1 mT. The temperature derivative ($d\chi'/dT$) is shown as a solid line

the primary ordering at 13 K, and has been attributed to a magnetic realignment, while the remarkably sharp feature in C_p(T) near 6 K was identified as characteristic of a first-order event [34].

While the $d\chi'/dT$ features at 8 K and 6 K are quite clear, they are not expected to be associated with bulk ordering, which C_p(T) places at about 13 K, where we see only a weak break in slope. As with the χ''(T) behaviour observed for $Gd_3Ag_4Sn_4$, it is unlikely that the small change in slope would be considered a signature of bulk ordering without prior knowledge of the heat capacity data to bias the search. The absence of a clear, objectively identifiable and consistent signature of bulk magnetic ordering in the susceptibility again demonstrates the weakness of χ'(T) data taken in isolation.

6.3.1 ^{119}Sn Mössbauer Spectroscopy

The ^{119}Sn Mössbauer spectrum of $Gd_3Cu_4Sn_4$ at 1.55 K shown on the right of Figure 6.12 is considerably more complex than those of related compounds. The characteristic broadened central doublet resulting from an unresolved low-field sextet is clearly present and accounts for about half of the total absorption area, as expected for one of the two equipopulous Sn sites. However, the pattern of multiple sharp lines at higher velocities (both positive and negative) is far too complex to fit with a single component. We found that a three-component fit with area ratios of 2:1:1 was the minimum set that would account for the observed pattern at high velocities, in addition to the 50% component associated with the low-field pattern. The three high-field components could be traced reliably up to about 11 K before line overlap caused them to blend into each other. We therefore believe that this decomposition of the spectra into a total of four components is correct and that it reflects complex ordering of the Gd moments in $Gd_3Cu_4Sn_4$. A similar three-component fit to the ^{119}Sn Mössbauer spectra of $Dy_3Ag_4Sn_4$ was found to be consistent with the magnetic structure determined by neutron diffraction [38].

The temperature dependence of the fitted magnetic field of all four components is shown in Figure 6.13, where it is clear that they extrapolate to an average transition temperature of 13.6(1) K, consistent with the ∼13 K derived from heat capacity data [34]. As with $Gd_3Ag_4Sn_4$, we found no significant impurity contribution in the spectra, and therefore confirm that 13.6(1) K represents the onset of bulk order in $Gd_3Cu_4Sn_4$.

Remarkably, there is no evidence in the ^{119}Sn Mössbauer spectroscopy data for the second, large thermal event at 8.2 K [34] that would correspond with the clear peak seen at 7.9 K in $\chi'(T)$ (Figure 6.11). 8 K is less than 60% of the transition temperature and the fields for all four components are at more than 80% of the saturation values seen at 1.55 K. Magnetic changes are clearly detected in $Tb_3Ag_4Sn_4$ [6], $Sm_3Ag_4Sn_4$ (seen in Chapter 5) and here in $Gd_3Ag_4Sn_4$ (left of Figure 6.7). With the large separation between the transition temperature and the lower event in $Gd_3Cu_4Sn_4$, any major rearrangement of the Gd moments should affect one or more of the Sn sites. Indeed, given the extremely complex sub-splitting of the large field component, the

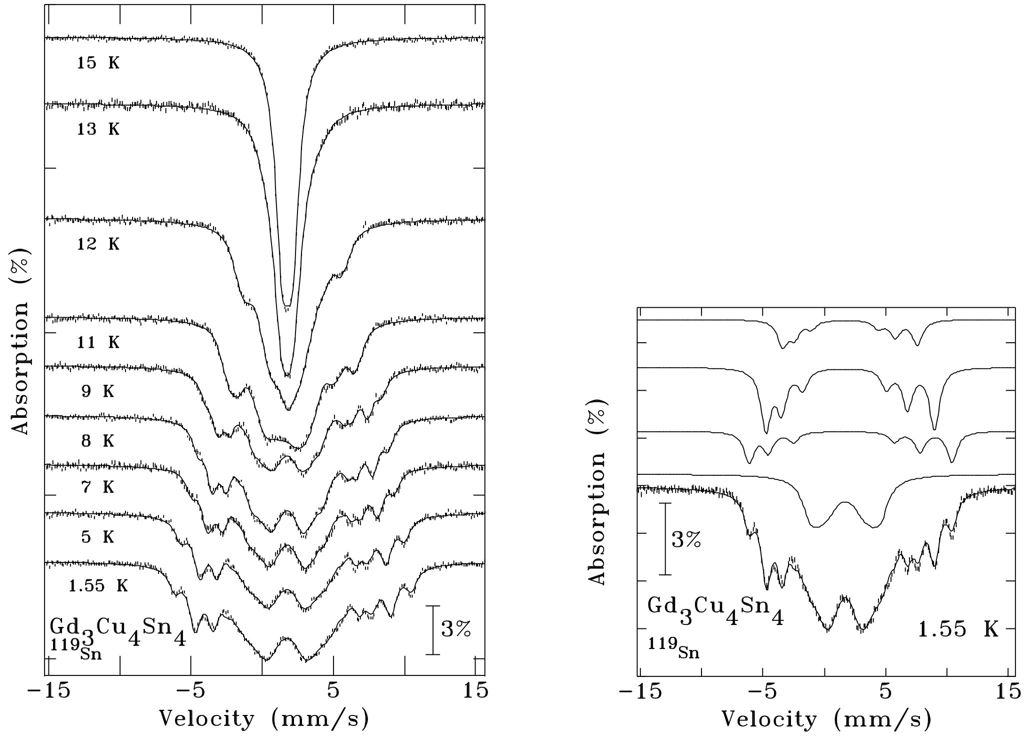

Figure 6.12: Left: ^{119}Sn Mössbauer spectra of $Gd_3Cu_4Sn_4$. Left-hand panel shows the temperature dependence of the spectra and the onset of magnetic order below ∼13 K. Solid lines are fits, described in the text. Right-hand panel shows the four components used to fit the 1.55 K spectrum.

potential for detecting changes in the magnetic structure should be greatly enhanced.

Similarly, there is no indication of the first-order event reported to occur near 6 K [34]. First-order magnetic transitions have clear signatures in the ^{119}Sn Mössbauer spectra of $Tb_3Ag_4Sn_4$ [6] and Gd_5Sn_4 [89], but no changes are detected here, in the subspectral areas, the quadrupole shifts or the hyperfine fields of $Gd_3Cu_4Sn_4$. The remarkable complexity of the spectra should make it easier to detect major changes in the magnetic structure, especially on the scale implied by C_p(T).

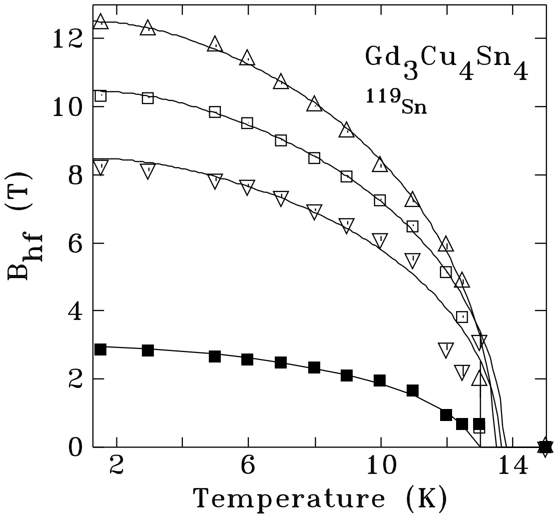

Figure 6.13: Temperature dependence of the ^{119}Sn hyperfine fields in $Gd_3Cu_4Sn_4$ showing the onset of bulk magnetic order at 13.6(1) K. Solid lines are independent fits to $J = \frac{7}{2}$ Brillouin functions for each component.

6.3.2 ^{155}Gd Mössbauer Spectroscopy

The ^{155}Gd Mössbauer spectra of $Gd_3Cu_4Sn_4$ are shown on the left of Figure 6.14. The onset of magnetic order determined from ^{155}Gd Mössbauer spectroscopy is consistent with the ∼13 K value .

Previous ^{155}Gd Mössbauer spectroscopy data on this compound also exhibited a transition temperature of ∼13 K, however the area ratio found was closer to 3:1, and magnetic field persisted at the Gd-4e site up to the Gd-2d transition temperature [90]. The ^{155}Gd Mössbauer spectrum collected at 5 K, shown on the right of Figure 6.14 shows the two components of the spectrum with a 2:1 ratio consistent with the crystallographic populations of each Gd sublattice, with the Gd-2d contribution shown in red and the Gd-4e contribution shown in blue. Fits in the magnetic phase showed that, as in the two other compounds discussed above, eQ_gV_{zz} is negative at the Gd-2d site, and positive at the Gd-4e site, while the asymmetry was high at the Gd-2d site, and low at the Gd-4e site. A fit to the paramagnetic 15 K pattern yields a

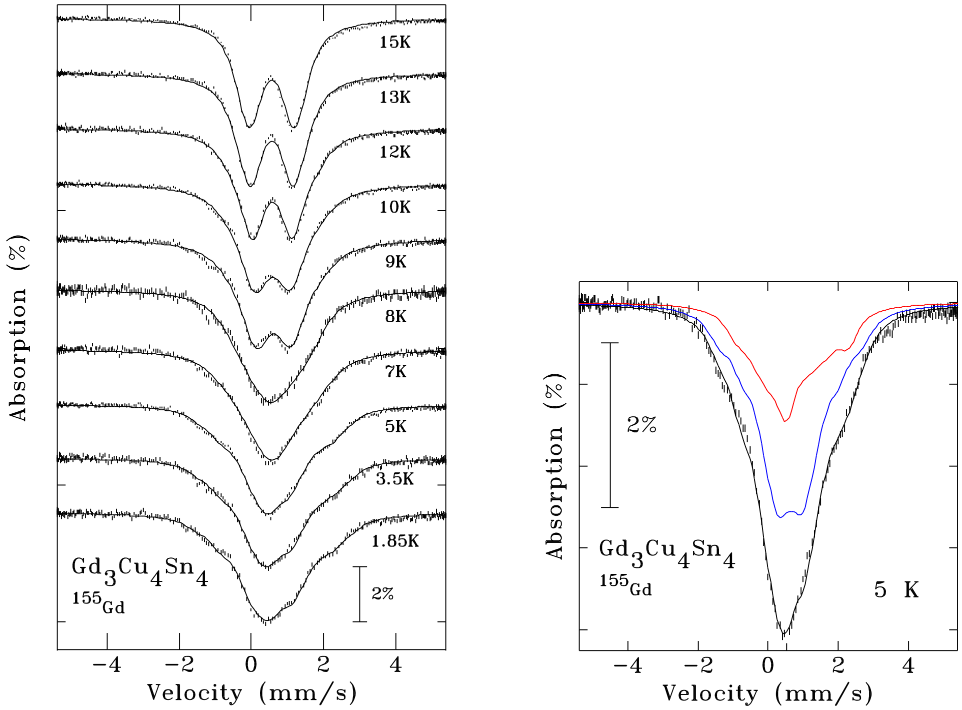

Figure 6.14: ^{155}Gd Mössbauer spectra of $Gd_3Cu_4Sn_4$. Left-hand panel shows the temperature dependence of the spectra and the onset of magnetic order below ∼13 K. Solid lines are fits, described in the text. Right-hand panel shows the Gd-2d (red) and Gd-4e (blue) components used to fit the 5 K spectrum.

eQ_gV_{zz} of −2.81(3) mm/s at the Gd-2d site and +2.33(2) mm/s at the Gd-4e site. The value of eQ_gV_{zz} we obtain for the Gd-2d site is significantly different than the value previously obtained. When measuring eQ_gV_{zz} in the paramagnetic state only a doublet is observed and with two components with similar values, the areas of the components will have an important influence on the fitted eQ_gV_{zz} values. When the area is underrepresented, the split can grow and the net effect on the pattern is to broaden the tail edges of the pattern. When the subspectrum is forced to have a larger area, the splitting of the peaks have to decrease to yield a good fit.

The temperature dependence of the hyperfine field is shown in Figure 6.15 and shows the separate ordering temperatures for the Gd-2d (13 K) and Gd-4e (8 K) sublattices. As was the case for the ^{119}Sn Mössbauer spectroscopy data on this compound, the ^{155}Gd Mössbauer spectroscopy data also shows no indication of the first order event seen in the susceptibility (Figure 6.4), at around 6.5 K, and in C_p(T) near 6 K [34].

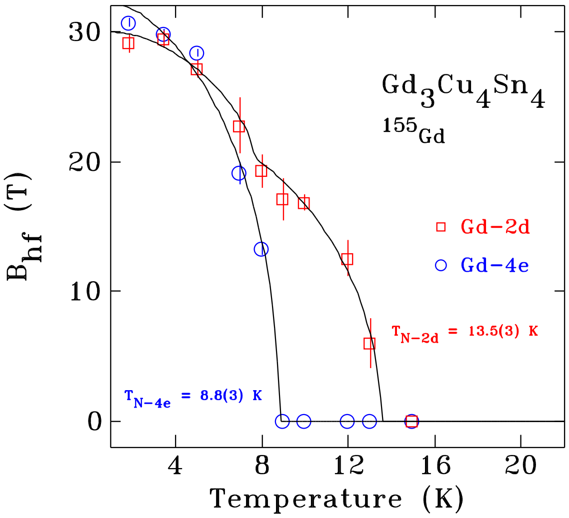

Figure 6.15: Temperature dependence of the fitted magnetic field from ^{155}Gd Mössbauer spectroscopy data on $Gd_3Cu_4Sn_4$ showing the separate ordering temperatures of the Gd-2d (13.5(3) K) and Gd-4e (8.8(3) K) sublattices.

The relative subspectral areas of the Gd-2d and Gd-4e sites allows again for the identification of each component independent of magnetic behaviour. While the magnetic scattering in neutron diffraction data is also phase quantitative, the identification of the origin of the magnetic signal using ^{155}Gd Mössbauer spectroscopy is entirely unambiguous, and will be of great value in the analysis of neutron diffraction data.

6.3.3 Neutron Diffraction

The neutron diffraction data on $Gd_3Cu_4Sn_4$ were acquired using the flat-plate sample holder described in section 3.2.4. The pattern acquired at 26 K using a wavelength of 2.37211(11) Å, shown in Figure 6.16, confirms the crystal structure and lattice

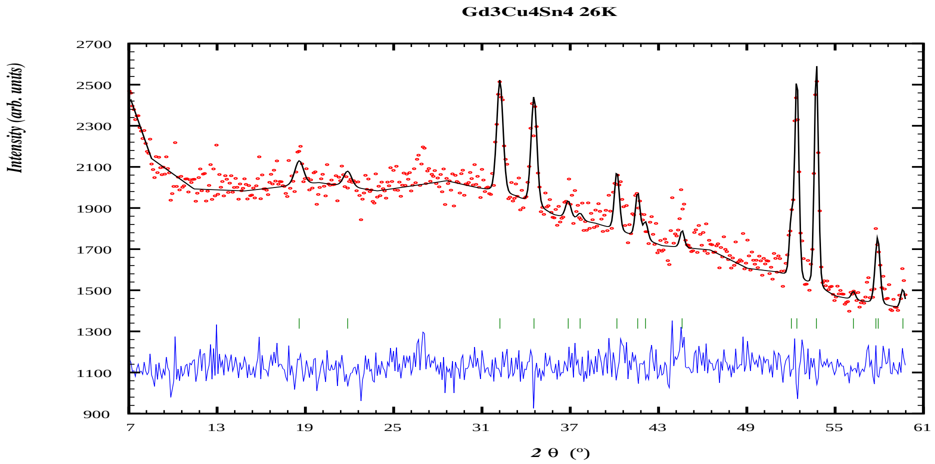

Figure 6.16: Neutron diffraction pattern of $Gd_3Cu_4Sn_4$ acquired at 26 K with a wavelength of 2.37211(11) Å, confirming the crystal structure and lattice parameters found by x-ray diffraction.

parameters found by x-ray diffraction. The scattering is quite weak, as was observed with the Sm compounds. For Gd compounds the weak scattering is less problematic as the expected saturation moment of Gd is around 7 μ_B, far larger than the Sm moment. Since the intensity of magnetic peaks scales as the square of the moment, the magnetic scattering will be far more sizeable.

The signal originating from nuclear scattering will not interfere with magnetic scattering (as discussed in section 3.2.2), thus peaks appearing in addition to the structural diffraction pattern indicate magnetic ordering. By inspecting the temperature dependence of the neutron diffraction patterns, shown in Figure 6.17, we can identify the peaks of magnetic origin. The dotted lines in Figure 6.17 indicate the two sets of magnetic peaks: one at $2\theta \sim 10°$ and a triplet at $2\theta \sim 20°$. Most of the magnetic peaks do not coincide with crystallographic reflections indicating an antiferromagnetic structure.

In order to isolate the magnetic signal, the difference between the magnetic pattern (3.1 K) and the crystallographic pattern (26 K) was computed. The resulting purely

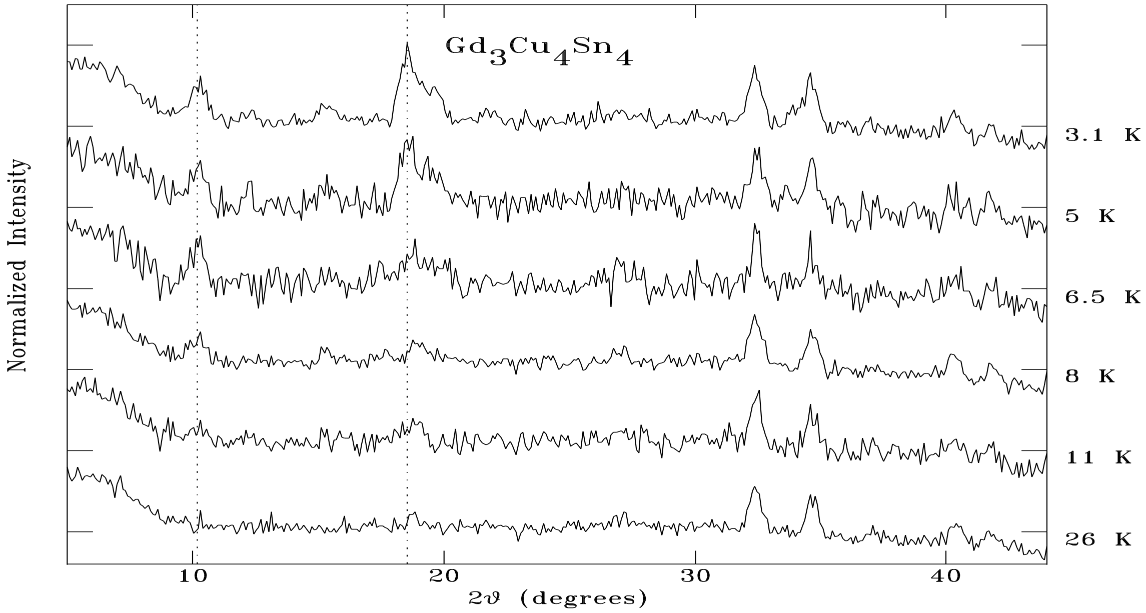

Figure 6.17: Temperature dependence of the neutron diffraction patterns of $Gd_3Cu_4Sn_4$ acquired at a wavelength of 2.37211(11) Å. The additional peaks which begin to appear below 13 K are quite strong by 3.1 K. The dotted lines indicate the two sets of peaks that will be attributed to ordering in the Gd-2d and Gd-4e sublattices.

magnetic signal can then be fitted in order to isolate the locations of the magnetic peaks, as shown in Figure 6.18.

Using the peak locations found via the difference plot of Figure 6.18, the temperature dependence of the peak intensities can be obtained. The temperature dependence of the intensities of the $\sim 10°$ and $\sim 19.7°$ peaks are shown in Figure 6.19 as examples. The $\sim 10°$ peak appears close to 13.6 K and the intensity of the $\sim 19.7°$ peak increases below 8 K. Using the ^{155}Gd Mössbauer spectroscopy results shown above, we can assign the $\sim 10°$ peak to the Gd-2d magnetic moments and the triplet peaks around 20° to the Gd-4e magnetic moments.

With the magnetic peaks in the neutron diffraction pattern identified and localized, the **k** vector for each sublattice (or possibly both) can be found. The intensity of

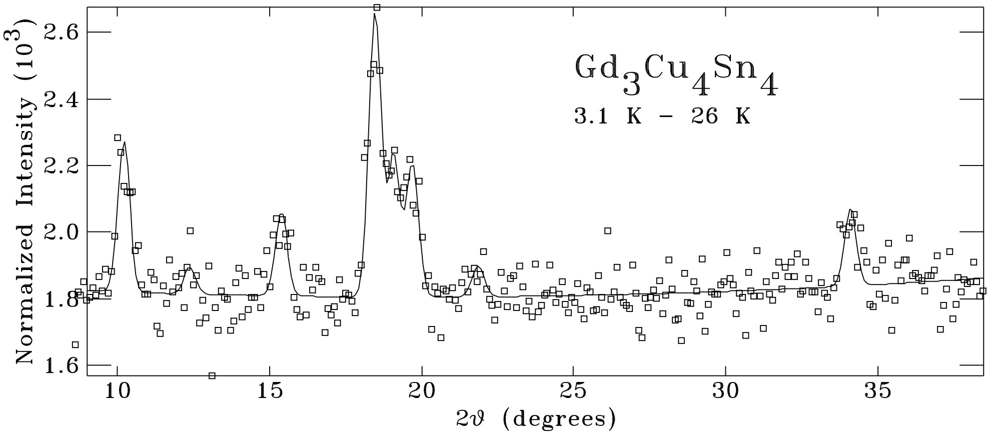

Figure 6.18: Difference between the scaled magnetic neutron diffraction pattern of $Gd_3Cu_4Sn_4$ (3.1 K) and the paramagnetic neutron diffraction pattern of $Gd_3Cu_4Sn_4$ (26 K), showing only the magnetic contribution to the scattering at 3.1 K.

magnetic reflections will depend on the exact magnetic structure adopted, however a LeBail fit using the crystal lattice parameters and trial **k** vectors can be performed by first restricting the search to special vectors which are simple fractions, then broadening the search.

Order of the Gd-4e moments

The Gd-4e sublattice fit yielded a propagation vector $\mathbf{k}_{4e}$=(0.43(1) 0.511(2) 0.484(1)), thus the magnetic periodicity is not a simple multiple of the crystallographic cell. The irreducible representations (IRs) computed for the Gd-4e moments with $\mathbf{k}_{4e}$ are listed in Table 6.1, and the decomposition of the magnetic representation into the IRs is:

$$\Gamma_{mag} = 3\Gamma_1 \tag{6.2}$$

The moments at the Gd-4e site are separated into two orbits: there is no symmetry operation that links the $(x_R, 0, 0)$ and $(x_R + \frac{1}{2}, \frac{1}{2}, \frac{1}{2})$ moments to the $(1 - x_R, 0, 0)$ and $(\frac{1}{2} - x_R, \frac{1}{2}, \frac{1}{2})$ moments. In our fits, if we treat the moments for the $(x_R, 0, 0)$ and $(x_R + \frac{1}{2}, \frac{1}{2}, \frac{1}{2})$ as independent from the $(\frac{1}{2} - x_R, \frac{1}{2}, \frac{1}{2})$ $(x_R + \frac{1}{2}, \frac{1}{2}, \frac{1}{2})$ moments,

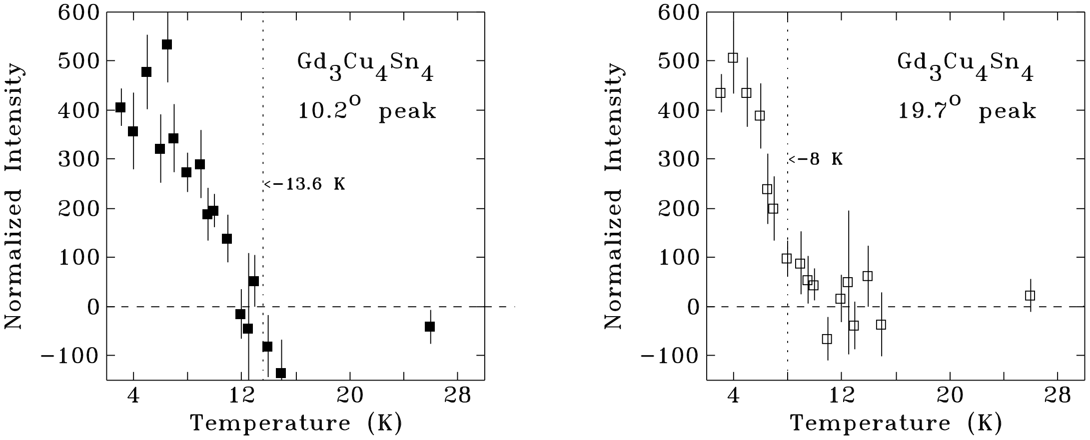

Figure 6.19: Temperature dependence of the magnetic peaks at $2\theta \sim 10^\circ$ and $\sim 19.7^\circ$ which, using the ^{155}Gd Mössbauer spectroscopy results, can be associated to the Gd-2d and Gd-4e moments respectively.

we obtain very large errors and parameter values that dependent strongly on the number of refinement steps, indicating that the problem is over-parametrized. We thus proceed by restricting the moments in different ways (ferromagnetic coupling, antiferromagnetic coupling), and assessing the quality of fit.

The model that fits the data best consists of order in the *ab*-plane only, with an antiferromagnetic coupling between the orbits. A fit of the 3.1 K pattern is shown in Figure 6.20, with the peaks associated with the Gd-2d order omitted (see below).

IR	Basis	Atom	Re(a)	Re(b)	Re(c)	Im(a)	Im(b)	Im(c)
Γ_1	ψ_1	$(x_R, 0, 0)$	1	0	0	0	0	0
	ψ_2	$(x_R, 0, 0)$	0	1	0	0	0	0
	ψ_3	$(x_R, 0, 0)$	0	0	1	0	0	0

Table 6.1: The basis vectors computed from the IRs of the $Immm$ space group for both orbits of the Gd-4e site in $Gd_3Cu_4Sn_4$ with the propagation vector $\mathbf{k}_{4e} = (0.43(1)\ 0.511(2)\ 0.484(1))$.

The resolution of the signal seen in Figure 6.17 does not allow differentiation between an amplitude modulated or square-wave modulated magnetic structure. However, given that the pattern is collected at 3.1 K (a quarter of the transition temperature), a sine-wave modulation with $\mathbf{k}_{4e}$=(0.43(1) 0.511(2) 0.484(1)) would leave a large portion of the moments not fully ordered which is unlikely. It is then reasonable to conclude that the moments are most likely square-wave modulated. The square-wave moment amplitude modulation is modeled by taking the first three terms of the square wave Fourier decomposition (using cosine waves consistent with Equation 2.13). The ordered moment at the Gd-4e site is 7.3(4) μ_B with the moments making an angle of 15(10)° with respect to the a-axis, while the expected fully ordered moment value 7 μ_B for Gd. This partially justifies the square-wave modulation assumption in that a sine-wave fit yields the unphysical value of 9.3(6) μ_B. The rather large error on the moment value, as well as the angle, comes mostly from a large error on the b component of the moment.

Relating the Gd-4e order to ^{119}Sn Mössbauer spectroscopy data

The $\mathbf{k}_{4e}$ propagation vector is very close to $(\frac{1}{2}, \frac{1}{2}, \frac{1}{2})$, and is not measurably different from $(\frac{1}{2}, \frac{1}{2}, \frac{1}{2})$ as far as ^{119}Sn Mössbauer spectroscopy is concerned. For the purposes of the transferred calculation we can make the useful approximation of assuming a $(\frac{1}{2}, \frac{1}{2}, \frac{1}{2})$ propagation vector when we calculate the effect of the Gd-4e moment ordering on the transferred field at the Sn-4f and Sn-4h sites. Consequently, any two Gd-4e moments separated by a lattice length in any crystallographic direction will be anti-parallel. The Gd-4e atoms around the Sn-4h site can be separated into two pairs separated by a lattice length in the c direction (right of Figure 6.21) and thus must be anti-parallel. Likewise, two of the Gd-4e moments around the Sn-4f site are separated by a lattice length in the c direction and the other two are separated by a lattice length in the b direction (left of Figure 6.21). If we consider isotropic field transfer, which yielded consistent results in the case of $Gd_3Ag_4Sn_4$, the Gd-4e

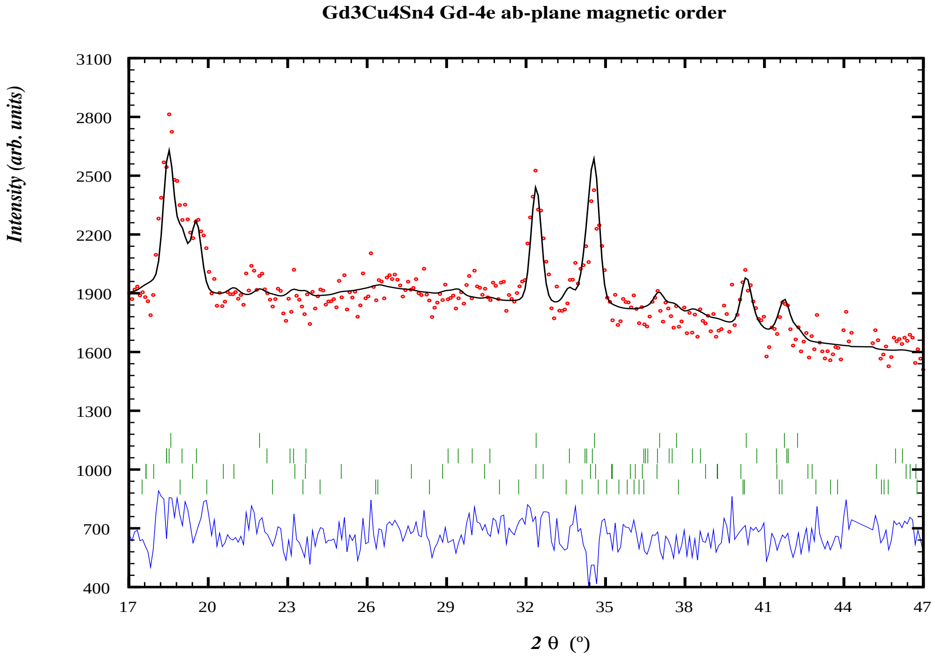

Figure 6.20: $Gd_3Cu_4Sn_4$ neutron diffraction pattern acquired at 3.1 K. The top Bragg markers belong to the crystallographic structure only, while the three following sets represent the first, second and third terms of the square wave Fourier decomposition. The peaks associated with the Gd-2d order have been omitted for the fit, while the Gd-4e adopt the magnetic structure described in the text.

moments should not contribute to the transferred hyperfine magnetic field at either of the Sn sites. This explains why there is no observed change in the temperature dependence of the transferred hyperfine field, shown on the left of Figure 6.13, at ~ 8 K where the Gd-4e moments order.

Order of the Gd-2d moments

The Gd-2d order in $Gd_3Cu_4Sn_4$ is responsible for the most complex ^{119}Sn Mössbauer spectra included in this study. Unfortunately, the neutron diffraction analysis presents much of the same difficulty as the high temperature Gd-2d order does in $Gd_3Ag_4Sn_4$

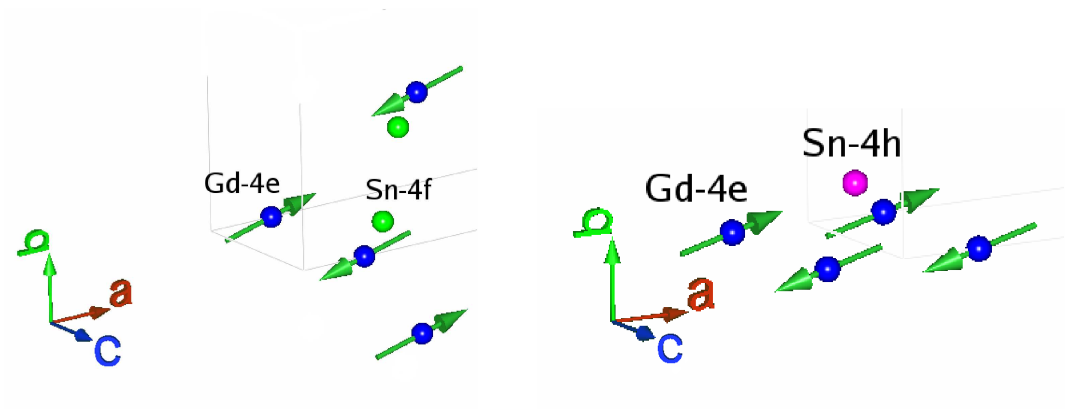

Figure 6.21: Left: Gd-4e nearest neighbour moments to the Sn-4f site in $Gd_3Cu_4Sn_4$. Right: Gd-4e nearest neighbour moments to the Sn-4h site in $Gd_3Cu_4Sn_4$.

discussed above. The Gd-2d moments must yield four distinct environments in order to be consistent with the ^{119}Sn Mössbauer spectroscopy results. Since the ordering of the Gd-4e moments has no effect on the ^{119}Sn Mössbauer spectra, the Sn-4f site has only one remaining rare earth neighbour that can contribute to the transferred hyperfine field. The one Gd-2d neighbour to the Sn-4f is solely responsible for the field at that site which represents half of the spectral area in the ^{119}Sn Mössbauer spectra. We therefore conclude that the low field component of the ^{119}Sn Mössbauer subspectrum which accounts for half the spectral area is assigned to the Sn-4f atoms.

The remaining three fields with 2:1:1 area ratio must therefore be the result of three individual environments at the Sn-4h site, which only has two Gd-2d neighbours. The Gd-2d moments neighbouring the Sn-4h site are separated by a lattice length along the c-axis and hence, the c component of the propagation vector must be non zero. Additionally, we cannot have a zero field component, consequently the Gd-2d moments cannot be anti-parallel.

One of the simpler ways to fulfill the modulation in the c-direction without having the moments be anti-parallel, is to have the Gd-2d moments have separate $\mathbf{k}$ vectors for each moment component, i.e. a separate $\mathbf{k}$ vector for μ_x and μ_y. The simplest way to have three separate environments for the Sn-4h site with a 2:1:1 area ratio is to have canted moments which are either parallel, at a shallow angle, and at a larger angle. These arrangements are shown in Figure 6.22.

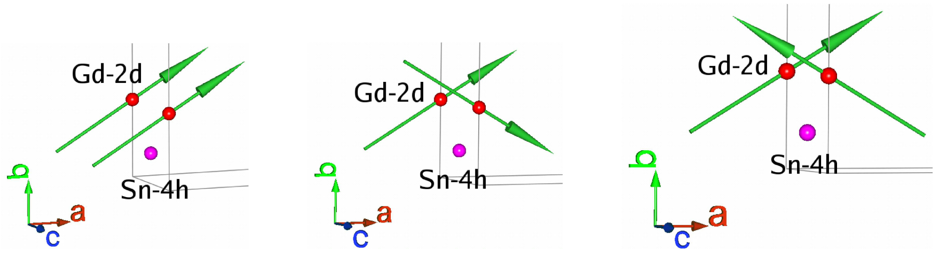

Figure 6.22: Relative orientations of Gd-2d moments that yield the maximum transferred field (Left), middle transferred field (Middle) and minimum transferred field (Right).

The main issue with the arrangements proposed in Figure 6.22 is that in order to fulfill the subspectral area distribution observed in the ^{119}Sn Mössbauer spectra, we need to lower the symmetry of the Gd-2d site by treating the 2 atoms in the unit cell as independent atoms not related by symmetry. There is no clear mechanism as to how this would occur, and hence this situation is unlikely.

The difficulty in adequately determining the magnetic structure, as was the case in $Gd_3Ag_4Sn_4$, stems from paucity and low intensity of peaks associated with the Gd-2d moments. We observe only a single truly resolved peak at 10.2°, with a second peak stemming from the Gd-2d moments, at 15.2°. We can however determine conclusively that the propagation vector for the Gd-2d site moments is neither (0,0,0), nor (1,1,1), meaning that the magnetic lattice must be larger than the crystallographic lattice.

6.4 Conclusions

$Gd_3Cu_4Ge_4$ and $Gd_3Ag_4Sn_4$ exhibit long ranged magnetic order far above the previously assigned magnetic ordering temperatures obtained from bulk magnetization measurements. Moreover, when these new ordering temperatures are used to compare with the other members of their respective $R_3T_4X_4$ series, the de Gennes scaling breakdown is either not as severe ($Gd_3Cu_4Ge_4$) or scales quite well ($Gd_3Ag_4Sn_4$, shown in Figure 6.23).

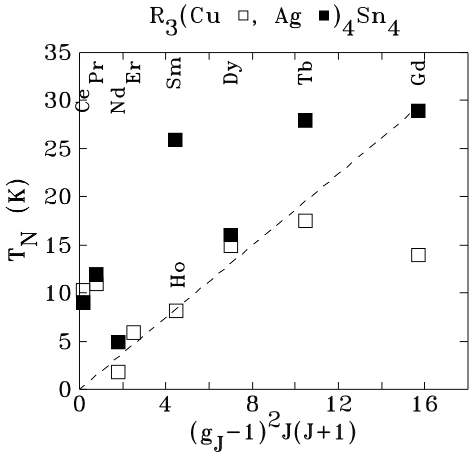

Figure 6.23: The highest magnetic transition temperatures in the $R_3Cu_4Sn_4$ (□) and $R_3Ag_4Sn_4$ (■) compounds versus the de Gennes factor $(g_J - 1)^2 J(J+1)$, with the value for $Gd_3Ag_4Sn_4$, $Sm_3Ag_4Sn_4$ and $Sm_3Cu_4Sn_4$ obtained in this work.

It is worth noting that the ^{119}Sn Mössbauer spectroscopy data on both $Gd_3Cu_4Sn_4$ and $Gd_3Ag_4Sn_4$ are somewhat similar to that of $Dy_3Ag_4Sn_4$ in that we observe significantly broadened spectra [38]. The magnetic structure of $Dy_3Ag_4Sn_4$, acquired under far more favourable circumstances (magnetic peaks of significantly greater intensity, better count rates and thus less noise), do not clearly indicate why we should observe broadened lines. ^{119}Sn Mössbauer spectroscopy data appear to be revealing magnetic behaviour invisible to neutron diffraction such as slow dynamics.

The $Gd_3Cu_4Sn_4$ compound proves to be the most complex of the compounds studied here. The transitions for the Gd-2d and Gd-4e sublattices are clearly separate, and their magnetic space groups at low temperature lead to a magnetic cell larger than the crystallographic cell. Although it is rather simple to explain why the ^{119}Sn

Mössbauer spectroscopy did not detect the ordering of the Gd-4e sublattice, the spectral makeup of the Sn-4h component of the ^{119}Sn Mössbauer spectrum is far more complex and the magnetic symmetry of the Gd-2d sublattice yields too few peaks in neutron diffraction measurements to allow for a clear and unambiguous magnetic structure determination. Moreover, the $Gd_3Cu_4Sn_4$ compound is confirmed to be a severe outlier in the de Gennes scaling of the $R_3Cu_4Sn_4$ compounds, shown in Figure 6.23. Finally, none of the techniques used in this study, all direct probes of magnetism, and neutron scattering sensitive to structural properties, exhibit any feature at 6.5 K, leaving no indication of the first-order event reported to occur at 6.5 K [34].

Chapter 7

Discussion and Conclusions

7.1 $\mathrm{R_3T_4X_4}$ and the Electric Field Gradient

The present work focuses on the magnetic properties of the $\mathrm{R_3T_4X_4}$ materials and the experimental determination of these. However the electric quadrupole properties measured by ^{119}Sn and ^{155}Gd Mössbauer spectroscopy of the $\mathrm{R_3T_4X_4}$ materials presented in this work can yield some information about this compound family.

The values of the quadrupole parameters measured by ^{119}Sn and ^{155}Gd Mössbauer spectra contain information about the local charge symmetry around the probe nucleus. A spherical charge distribution leads to no quadrupole splitting, whereas a charge distribution with lower than cubic symmetry is observed as electric field gradient with a principal axis value V_{zz}. If the electric field gradient is not axially symmetric ($V_{xx} \neq V_{yy}$) a non zero asymmetry parameter value η. One important limitation of both ^{119}Sn and ^{155}Gd Mössbauer spectroscopy is that, in the paramagnetic phase, the simple doublet observed yields only $\left|\frac{eQ_eV_{zz}}{2}\sqrt{(1+\eta^2/3)}\right|$ and a determination of the sign of V_{zz} as well as the size of η requires measurements in the magnetic phase.

7.1.1 Sn compounds as measured by ^{119}Sn Mössbauer Spectroscopy

It is a confirmation of the structural consistency of $R_3T_4X_4$ compounds in adopting the $Gd_3Cu_4Ge_4$-type structure that the ^{119}Sn Mössbauer spectra acquired in the paramagnetic state all have similar values (Figure 7.1). The $Nd_3Cu_4Sn_4$ and $Sm_3Ag_4Sn_4$ values stand out as larger than the others.

First considering $Nd_3Cu_4Sn_4$, as was discussed in Chapter 4, the lowest temperature magnetic spectrum obtained has an observed hyperfine magnetic field that does not yield sufficient splitting to determine with certainty an exact model of the magnetism present with certainty. The inflated value could likely be due to a non-zero asymmetry, η, of the electric field gradient. If the actual value of eQV_{zz} is closer to 0.78 mm/s, like most other Cu based compounds, this would yield an η value of roughly 0.67, indicating that the electric field gradient evolves from highly asymmetric to symmetric as the we progress through the rare earth series.

Considering the $Sm_3Ag_4Sn_4$ values, it is important to note that the magnetic phase spectra were better fit with a negative $\frac{eQV_{zz}}{2}$. Combining this result with the important contribution of anisotropic hyperfine field transfer, $Sm_3Ag_4Sn_4$ clearly distinguishes itself from other members of the $R_3Ag_4Sn_4$ compound family. $Sm_3Ag_4Sn_4$ is also an outlier in terms of de Gennes scaling, and hence it is possible that its magnetic pathology has an electronic origin which is revealing itself through the electric field gradient.

The remaining members, those that have similar $\frac{eQV_{zz}}{2}$ values as well as $\eta = 0$, allow for a determination of the likely direction of V_{zz} at both Sn sites. Using the point symmetry of the Sn-4f and Sn-4h sites in the $Gd_3Cu_4Ge_4$-type structure, V_{zz} points along one of the crystallographic axes. From the ^{119}Sn Mössbauer spectroscopy data coupled with the neutron diffraction data on $Nd_3Ag_4Sn_4$, $Ho_3Cu_4Sn_4$, and $Gd_3Ag_4Sn_4$, we determine that V_{zz} points along the c-axis at the Sn-4f site and along the a-axis at the Sn-4h site.

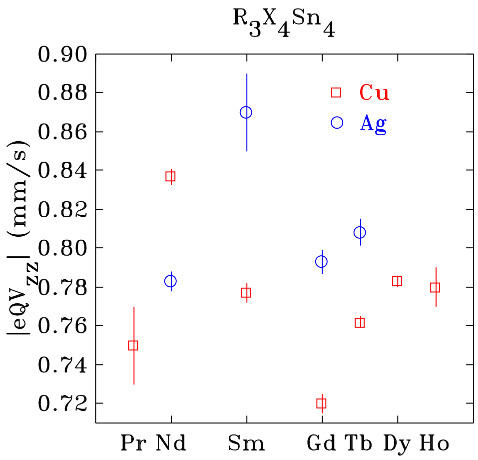

Figure 7.1: Values of $|eQV_{zz}|$ from fitted ^{119}Sn Mössbauer spectra in the paramagnetic phase just above the magnetic transition temperature for each compound. Note that the value for $\text{Pr}_3\text{Cu}_4\text{Sn}_4$ assumes $\eta = 1$ based on the spectra obtained in the magnetic phase.

Variation in measured V_{zz} values, even within a compound family, is not entirely uncommon. In a similar system, the RTSn family of compounds, the Ag compounds have $\frac{eQV_{zz}}{2}$ values of approximately -1 mm/s [91], whereas the Cu compounds have $\frac{eQV_{zz}}{2}$ values around 0.6 mm/s [92, 93, 94, 95]. Even within the Cu series the value of $\frac{eQV_{zz}}{2}$ for GdCuSn is an outlier at 1 mm/s [96]. We note that although the RTSn system does not share the structural uniformity seen in the $\text{R}_3\text{T}_4\text{Sn}_4$ compounds (two possible hexagonal structures, CaIn_2-type (space group $P6_3/mmc$) or GaGeLi-type (space group $P6_3mc$)), the compounds considered for comparison here all adopt the GaGeLi-type structure.

7.1.2 Gd compounds as measured by ^{155}Gd Mössbauer spectroscopy

The measured values of eQ_gV_{zz} for the three compounds studied here are listed in Table 7.1. We see that the $\text{Gd}_3\text{Ag}_4\text{Sn}_4$ is somewhat of an outlier in that the eQ_gV_{zz}

Compound	eQ_gV_{zz} (mm/s) Gd-2d	eQ_gV_{zz} (mm/s) Gd-4e
$Gd_3Cu_4Ge_4$	$-3.33(3)$	$+2.74(2)$
$Gd_3Ag_4Sn_4$	$-2.2(2)$	$+2.32(9)$
$Gd_3Cu_4Sn_4$	$-2.81(3)$	$+2.33(2)$

Table 7.1: Values of the quadrupole splitting in Gd compounds measured by ^{155}Gd Mössbauer spectroscopy.

value for the Gd-4e site is larger than that of the Gd-2d site, unlike the other two compounds studied.

In the case of $Gd_3Ag_4Sn_4$, for which base temperature neutron diffraction data is best understood, combining the neutron diffraction and ^{155}Gd Mössbauer spectroscopy measurements easily yields the direction of the principal axis of the electric field gradient (V_{zz}). We determine that V_{zz} points along the *c*-axis at the Gd-2d site, and along the *a*-axis at the Gd-4e site. In the absence of a well determined magnetic structure for the Gd-2d site in $Gd_3Cu_4Sn_4$, we must limit ourselves to the Gd-4e site. The ^{155}Gd Mössbauer spectroscopy results indicate that the moment make an angle of $55(3)^\circ$ with V_{zz}, and thus if the moment is mostly along the *a*-axis, then V_{zz} is along *b*. Given the statistics of the pattern however, this conclusion must be taken with caution as the direction of the moment is based entirely on the intensity ratio of the magnetic peaks since the moment is planar. A similar problem is encountered with $Gd_3Ag_4Sn_4$ [88]. Finally, $Gd_3Cu_4Ge_4$ still requires neutron diffraction data before we can determine the direction of V_{zz} at the Gd sites.

Table 7.1 also reveals that the variation in the lattice contribution to the electric field gradient at the rare earth site can be quite important. Since Gd^{3+} is an S-state ion ($L = 0$), there is no $4f$ contribution to the electric field gradient and the observed V_{zz} values are entirely due to contributions from the lattice. We observe a

50% increase from $Gd_3Ag_4Sn_4$ to $Gd_3Cu_4Ge_4$ at the Gd-2d site, while there is far less variation at the Gd-4e site. The analysis cannot be taken further though considering the relatively poor resolution of quadrupole doublets in the paramagnetic region in ^{155}Gd Mössbauer spectroscopy.

7.2 Magnetic Properties

The structural uniformity, revealed by x-ray diffraction measurements, neutron diffraction measurements, and the measured quadrupole splitting by ^{119}Sn Mössbauer spectroscopy, make the broad variety of magnetic behaviour observed in the $R_3T_4X_4$ system all the more surprising. A diversity of the behaviour is found in terms of transition temperatures, magnetic structures, and as we have discovered in this study, whether the moments undergo static order at all. We have found cases in which the magnetic structures are relatively simple and the ^{119}Sn Mössbauer spectroscopy results can be interpreted relatively simply, such as $Nd_3Ag_4Sn_4$, $Pr_3Cu_4Sn_4$, and $Ho_3Cu_4Sn_4$. We have also found that the magnetic structures adopted by $Gd_3Cu_4Sn_4$ and $Gd_3Ag_4Sn_4$ are far more complex, as are the ^{119}Sn Mössbauer spectroscopy results, and that the use of ^{155}Gd Mössbauer spectroscopy is a necessary component in understanding the magnetic behaviour. Meanwhile, $Sm_3Cu_4Sn_4$ and $Sm_3Ag_4Sn_4$ exhibit behaviours that lie strictly outside of that which is observed for other members of this compound family.

7.2.1 Experimental Considerations

The weakness of magnetic susceptibility measurements

Magnetic susceptibility measurements are a very popular tool to determine magnetic ordering temperatures due to the ease of operation of commercial equipment and typically clear signatures of magnetic order, even though the technique offers little in terms of magnetic structure characterization. A more important limitation of the technique is determining the exact source of the signal measured. The technique is sensitive to the total magnetic response of the material used, hence a small impurity by mass can potentially swamp the signal. Differentiating the impurity signal from the primary phase signal then requires a precise determination of the nature of the impurity and precise determination of its magnetic properties so that the contribution may be subtracted. Magnetic susceptibility measurements on the $R_3T_4X_4$ materials have shown that the onset of magnetic order often yields a weak signature, exacerbating the problem. The weak peaks observed in $Sm_3Cu_4Sn_4$ [29] that were attributed to magnetic order could have come from impurities in small quantities with strong magnetic susceptibility signals.

An excess of detected peaks is not the most common problem though. As we have seen in this work, there are several cases in which magnetic susceptibility failed to detect the onset of magnetic order entirely. There is no clear trend in the failure of detecting magnetic order in the $R_3T_4X_4$. The lack of signal does not appear to be site dependent: in the $Gd_3Ag_4Sn_4$ case the ordering of both sublattices at 28.8(2) K was missed. The absence of signal does not appear to be attributable only to the specific rare earth atom present since in both the $Er_3Cu_4X_4$ [4] and $Gd_3T_4Sn_4$ (this work) compound families the ordering is properly detected in some but not all members.

There is as of yet no clear mechanism that could explain the failure of the technique to detect the onset of magnetic order for some members of the $R_3T_4X_4$ compound family. The results reported in this work however, clearly demonstrate the need to complement magnetic susceptibility data with other experimental techniques in order to properly understand the nature of magnetic order.

^{119}Sn Mössbauer spectroscopy

The use of ^{119}Sn Mössbauer spectroscopy in this study provided unique and valuable information about the magnetic properties of several members of the $R_3T_4Sn_4$ system. As will be further discussed below, the relative sizes of the transferred fields between

Sn sites in the same compound allowed us to identify the Sn sites responsible for each subspectrum in most cases. The size of the transferred between compounds however, is a more complex matter. The transferred hyperfine fields measured for the Cu and Ag compounds are shown on the left of Figure 7.2.

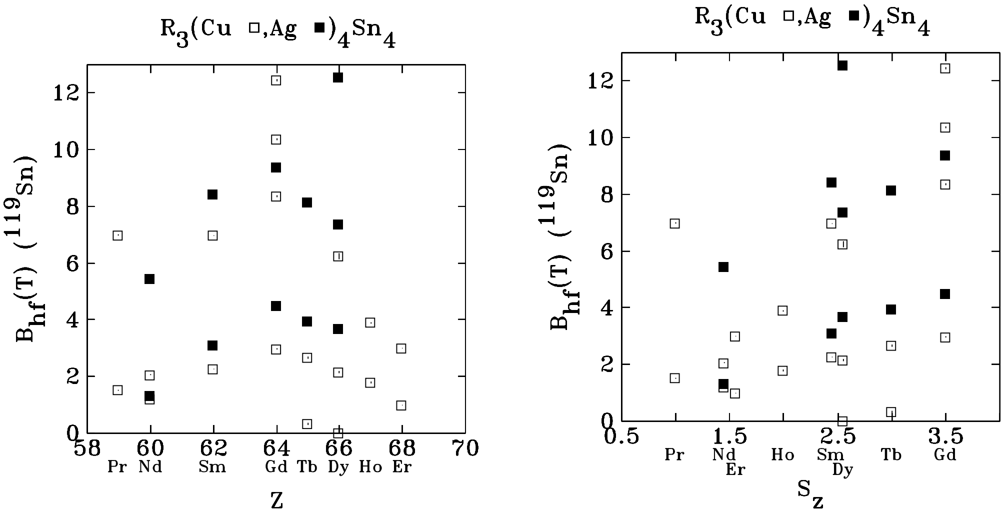

Figure 7.2: Transferred hyperfine fields measured by ^{119}Sn Mössbauer spectroscopy at base temperatures for the $R_3(Cu, Ag)_4Sn_4$ compounds with respect to atomic number Z on the left and with respect to the spin angular momentum S_z on the right.

Work by Delyagin *et al.* suggests that the transferred field does not depend strictly on the ordered moment of the compound [97], but rather on the number of nearest neighbours, the spin angular momentum of the rare earth atom, S_z, and the distance between the rare earth and Sn atoms. Clearly, since the Gd and Sm compounds have comparable size fields, while the Gd ordered moment is at least an order of magnitude larger than the Sm moment, the transferred field cannot depend on the ordered moment alone. The left of Figure 7.2 shows the transferred field as a function of S_z. Considering the various subspectral fields, a generally increasing trend with S_z can be seen, with the $Dy_3Ag_4Sn_4$ as an obvious outlier. We note that a direct comparison with the data in [97] is difficult since the characteristic distance R_{nn}/R_{4f}

for this work is far smaller (∼1.82 versus ∼5.75), and yet the S_z dependence of the transferred hyperfine field is in reasonable agreement with the model.

Neutron diffraction and Mössbauer spectroscopy complementarity

Neutron diffraction and Mössbauer spectroscopy are sensitive to magnetism in very different ways. Neutron diffraction is sensitive to long range periodic order, and thereby yields information about magnetic symmetry. Mössbauer spectroscopy is a local probe of the magnetic environment through both the hyperfine field and the electric field gradient. It is thanks to these different sensitivities to the same phenomenon that the two techniques complement each other so well, and were put to great use in this study. Also, as mentioned above, the mechanism which determines the magnitude of the transferred hyperfine field is not fully understood, and combining neutron diffraction with ^{119}Sn Mössbauer spectroscopy data, also contributes significantly to the understanding of the field transfer.

Even a simplistic transferred field model assuming only isotropic transfer (ignoring the small variations in distance, but taking into account the different moment sizes) leads to a quite reasonable agreement with existing neutron diffraction data. In the case of $Sm_3Ag_4Sn_4$ the neutron diffraction data indicated that anisotropic transfer must be taken into account. The field ratios observed by ^{119}Sn Mössbauer spectroscopy and their corresponding neutron diffraction data derived ratios (assuming isotropic transfer unless otherwise indicated) are listed in Table 7.2. One apparent trend of Table 7.2 is that the model used tends overestimate the transferred field the light rare earths (Pr, Nd, Sm) whereas it underestimates them for the heavy rare earths (Gd, Tb, Dy, Ho, Er).

It is worth noting as well that work on the $R(Mn,Fe)_6Sn_6$ system has shown that the size of the anisotropic contribution to the transferred hyperfine field (A_p in Equation 3.23) can be different depending the Sn site within the same material [61, 98, 99]. Given that the field ratios obtained from ^{119}Sn Mössbauer spectroscopy

Compound	Sn-4h:Sn-4f (isotropic)	Sn-4h:Sn-4f B_{hf}
$Pr_3Cu_4Sn_4$	5.2	4.57(6)
$Nd_3Ag_4Sn_4$	5.55	4.11(6)
$Sm_3Cu_4Sn_4$	complex: dynamics	
$Sm_3Ag_4Sn_4$	0.57 (aniso)	0.368(3)
$Gd_3Cu_4Sn_4$	complex	
$Gd_3Ag_4Sn_4$	2	2.08(1)
$Tb_3Cu_4Sn_4$	–	–
$Tb_3Ag_4Sn_4$	complex	2.07
$Dy_3Cu_4Sn_4$	–	–
$Dy_3Ag_4Sn_4$	Sn-4h$_1$:Sn-4h$_2$:Sn-4f 1.98:0.58:1	Sn-4h$_1$:Sn-4h$_2$:Sn-4f 3.42(3):2.00(3):1
$Ho_3Cu_4Sn_4$	2	2.17(3)
$Er_3Cu_4Sn_4$	2	2.86

Table 7.2: Transferred hyperfine fields as predicted from neutron diffraction data with an isotropic field transfer model (unless otherwise indicated), and the experimental values obtained from ^{119}Sn Mössbauer spectroscopy data.

measurements compare so well with neutron diffraction derived ratios, it is likely that the values of A_s for the $R_3T_4Sn_4$ series are quite similar at the Sn-4f and Sn-4h sites.

Gd and Sm compounds (and where applicable, Eu compounds as well) have been largely omitted from neutron diffraction study, and when possible, ^{119}Sn Mössbauer spectroscopy replaced neutron diffraction entirely, for example in the RTSn or the RSn_3 compounds. Even with ^{119}Sn Mössbauer spectroscopy data readily available, the analysis was fairly limited. For example, the analysis of $SmSn_3$ leads to a proposed magnetic structure from a ^{119}Sn Mössbauer spectrum with an essentially invisible magnetic splitting [100]. Moreover, the same study omitted $SmSn_3$ from analysis among other members of that compound family citing the J-level mixing as the reason for the incongruity of some of the results. ^{119}Sn Mössbauer spectroscopy data on $Sm_3Ag_4Sn_4$ has shown that there is non-negligible anisotropic contribution to the transferred hyperfine field, and it is possible that the same process is responsible for the observed behaviour.

In this context, the flat-plate neutron diffraction measurements on the Sm and Gd compounds proved to be a powerful new tool. The results presented here clearly demonstrate that the magnetic structures, and more broad magnetic features of these materials, so often under explored, can be revealed, even if sometimes only partially. In the current experimental configuration however, the magnetic contribution to the neutron scattering signal can still be quite weak and the flat-plate neutron diffraction technique is most effective when combined with Mössbauer spectroscopy. The application of these various techniques is thus finally allowing more direct access to the magnetic properties of Gd compounds, often the prized members of rare earth compound series.

7.2.2 Magnetism in the $\mathrm{R_3T_4Sn_4}$ system

Compiling existing data (summarized in Tables 2.4 and 2.5), with revisions including the discoveries made in this study (Tables 7.4 and 7.3), the magnetic behaviour of the $\mathrm{R_3T_4Sn_4}$ system remains extremely diverse. The four most important revisions are for $\mathrm{Sm_3Ag_4Sn_4}$ (significant increase in $\mathrm{T_N}$), $\mathrm{Sm_3Cu_4Sn_4}$ (no actual ordering, slow moment dynamics), $\mathrm{Gd_3Ag_4Sn_4}$ (significant increase in $\mathrm{T_N}$) and $\mathrm{Nd_3Cu_4Sn_4}$ (confirm the transition temperature obtained from heat capacity and magnetization data, and confirm the presence of magnetism via neutron diffraction). A more minor revision was made to the magnetic behaviour of $\mathrm{Ho_3Cu_4Sn_4}$ (persisting magnetic interactions to just above 10 K).

The revisions in transition temperature of the $\mathrm{Sm_3Ag_4Sn_4}$ and $\mathrm{Gd_3Cu_4Sn_4}$ compounds establishes that the Ag based compounds tend to order at higher temperatures than their Cu based counterparts, with the Ce compounds as slight outliers. One of the main issues that drove the study of these systems in recent years was the breakdown of de Gennes scaling. Clearly, even with the revisions in transition temperatures made here, the problem persists, though not in all the places originally thought. While $\mathrm{Sm_3Ag_4Sn_4}$ was first thought to obey the scaling, it is now a clear outlier by a factor of more than 3. $\mathrm{Gd_3Ag_4Sn_4}$ made a clean return to de Gennes compliance while the transition temperatures for $\mathrm{Gd_3Cu_4Sn_4}$ and to a lesser extent $\mathrm{Gd_3Cu_4Ge_4}$, remain persistently low. Thus, as the system continues to show immense diversity and complexity, the information obtained in this study significantly alters the landscape.

Sm compounds are typically thought to behave as outliers because of the J-level mixing mentioned earlier, as was thought in the $\mathrm{SmSn_3}$ case. It is still surprising though that the $\mathrm{Sm_3Ag_4Sn_4}$ compound has strong magnetic stability compared to its neighbouring compounds while $\mathrm{Sm_3Cu_4Sn_4}$ in essence shows a greatest lack of it of all $\mathrm{R_3T_4Sn_4}$ compounds showing no evidence of static order. These results serve to underline that the variation in behaviour between Ag and Cu compounds are as diverse

Compound	T_N 2d (K)	T_N 4e (K)	Reorientation Temperature (K)	Magnetic Structure Type	Ref.
$Ce_3Cu_4Sn_4$	10.3(n)		7.8(n) - 2.6(n)	incom.+com.	[35]
$Pr_3Cu_4Sn_4$	11(n)			com.	[28]
$Nd_3Cu_4Sn_4$	1.8(m-h-Moss) < 1.5(n)*				[29, 28], [This Work]
$Sm_3Cu_4Sn_4$	dynamic (Moss)				[This Work]
$Gd_3Cu_4Sn_4$	13.5(3) (Moss-n)	8.8(3) (Moss-n)		incom.	[This Work]
$Tb_3Cu_4Sn_4$	17.5(n)			incom.	[30]
$Dy_3Cu_4Sn_4$	15(n)			incom.	[30]
$Ho_3Cu_4Sn_4$	7.6 (h)	3.3(h)	2.3(h) - 4.4(h) 5.5(h)	incom.+com.	[36]
	mag. inter.> 10 (Moss)**			incom. + com.	[This Work]
$Er_3Cu_4Sn_4$	5.9(n)	2(n)	5.6(n)	incom.	[4, 37]

Table 7.3: Magnetic transition temperatures and lower temperature magnetic transitions of the $R_3Cu_4Sn_4$ compounds, as measured by heat capacity (h), neutron diffraction (n), Mössbauer spectroscopy (Moss) and bulk magnetization (m), revised from Table 2.4 to include the results presented in this work. The magnetic structure type, commensurate (com.) or incommensurate (incom.) is also listed. * Although we have yet to perform neutron diffraction measurements above 0.38 K, we have confirmed that some magnetic signal is clearly observed at 0.38 K. ** The nature of the magnetism persisting to just above 10 K in $Ho_3Cu_4Sn_4$ cannot be unambiguously characterized.

Compound	T_N 2d (K)	T_N 4e (K)	Reorientation Temperature (K)	Magnetic Structure Type	Ref.
$Ce_3Ag_4Sn_4$	9(m)-<1.5(n)				[31, 32]
$Pr_3Ag_4Sn_4$	12(n)		9	incom. +com.	[8]
$Nd_3Ag_4Sn_4$	5(n)			com.	[8]
$Sm_3Ag_4Sn_4$	-	26.0(5) (Moss)	8.3(3) (Moss - n)	com	[This Work]
$Gd_3Ag_4Sn_4$	28.8(2) (Moss)		8 (Moss - n)	incom. + com.	[This Work],[88]
$Tb_3Ag_4Sn_4$	28(n-Moss)		13(Moss)		[6]
$Dy_3Ag_4Sn_4$	16(n)		14(n)	com. + incom.	[38]
$Ho_3Ag_4Sn_4$	NA				
$Er_3Ag_4Sn_4$	NA				

Table 7.4: Magnetic transition temperatures and lower temperature magnetic transitions of the $R_3Ag_4Sn_4$ compounds, as measured by neutron diffraction (n), Mössbauer spectroscopy (Moss) and bulk magnetization (m), revised from Table 2.5 to include the results presented in this work. The magnetic structure type, commensurate (com.) or incommensurate (incom.) is also listed.

as the variations between compounds of different rare earth. The Gd compounds studied here, exhibited somewhat unusual behaviour beyond the de Gennes scaling failures in the $R_3Cu_4Sn_4$ and $R_3Cu_4Ge_4$ in that we observed line broadening in ^{119}Sn Mössbauer spectroscopy data for both $Gd_3Cu_4Sn_4$ and $Gd_3Ag_4Sn_4$. Typically this would indicate a distribution of fields, as was originally thought in the $Sm_3Cu_4Sn_4$ system, and it is possible that the relatively noisy neutron diffraction signal is hiding more subtle features of the magnetic structure. Clearly, the Gd-2d structure must be quite complex to produce the observed ^{119}Sn Mössbauer spectrum.

7.3 Future Work

7.3.1 Sm Compounds

The neutron diffraction flat plate mounting technique has been demonstrated to yield usable data with Sm based compounds. The Sn signal from ^{119}Sn Mössbauer spectroscopy measurements is large and yet it is unclear in what proportions the isotropic and anistropic hyperfine field contribute to the total observed field. It would be well worth measuring more Sm compounds to find one that has a clear magnetic contribution to the neutron diffraction pattern at all temperatures for which ^{119}Sn Mössbauer spectra also show the presence of a transferred field, to determine the proportions of the anisotropic and isotropic transfer more precisely.

7.3.2 Single Crystals of $R_3T_4X_4$

Single crystals of any of the $R_3(Cu, Ag)_4Sn_4$ compounds have yet to be synthesized. Workers have already been able to synthesize compounds with the $Gd_3Cu_4Ge_4$-type structure ($Ho_3Pd_4Ge_4$ [101], $Sc_4Ni_4Ge_4$ [102], $Yb_3Pd_4Ge_4$ [103] and $Er_3Pd_{3.68(1)}Ge_4$ [104]), indicating that single crystals of $R_3(Cu, Ag)_4Sn_4$ compounds are likely possible.

Single crystals are of great experimental value since measurements can target specific crystallographic directions. Techniques that are used with powder averaging, such as Mössbauer spectroscopy and neutron diffraction, are of even greater value with single crystals. Since the γ absorption in Mössbauer spectroscopy depends on the relative orientation of the fields at the nucleus and the γ direction, moment directions can determined directly. In neutron scattering the crystallographic directions can be probed individually greatly simplifying the analysis as well as clarifying possible ambiguities.

7.3.3 Intermediate Compositions

A natural progression for the study of these compounds is to determine the behaviour of compounds with intermediate compositions. Preliminary results from the $\mathrm{Tb_{3-x}Ho_xCu_4Sn_4}$ system [105] have been reported as well as a study on the $\mathrm{Ho_{3-x}Y_xCu_4Sn_4}$ system [106]. However, since the $\mathrm{Ho_3Cu_4Sn_4}$ seems to present an particularly high complexity with several reordering events, starting with other combinations could be more valuable. Since $\mathrm{Dy_3Cu_4Sn_4}$ appears to exhibit fairly simple magnetic behaviour and $\mathrm{Dy_3Ag_4Sn_4}$ undergoes several, well defined magnetic transitions, a $\mathrm{Dy_3(Cu, Ag)_4Sn_4}$ could shed some light on the nature of the independent ordering or the rare earth sublattices. $\mathrm{Tb_4Cu_4Sn_4}$ also appears to have a fairly simple magnetic behaviour while $\mathrm{Tb_3Ag_4Sn_4}$ undergoes a magnetostructural transition followed by a subsequent moment reorientation, making a $\mathrm{Tb_3(Cu, Ag)_4Sn_4}$ series also interesting. Preliminary results indicate that the $\mathrm{Tb_3(Cu, Ag)_4Sn_4}$ compound series follows expected trends in lattice constant (Figure 7.3), however sufficient sample purity has not yet been achieved.

7.3.4 The crystal electric field in the $\mathrm{R_3T_4X_4}$ system

Although crystal electric field effects are far smaller for the rare earths than for the transition metal magnetic materials (discussed in Chapter 1), it has been demonstrated that they can have an important impact on the transition temperatures of

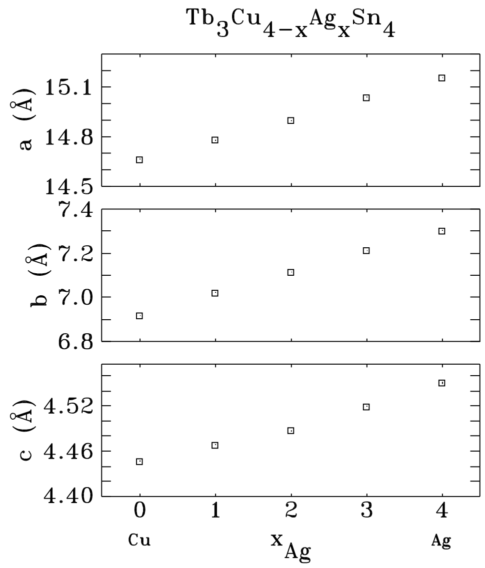

Figure 7.3: Preliminary results on the $Tb_3(Cu, Ag)_4Sn_4$ compound series fitted lattice parameters from x-ray diffraction, exhibiting the expected lattice expansion from Cu to Ag.

rare earth compounds [86], and it has been suggested that this could be the reason for the breakdown of de Gennes scaling in the compounds discussed in this work [14, 107]. A proper measurement of the crystal field levels could provide important enlightenment on this issue, and allow for a better understanding of the transition temperature scaling in these compounds. It should be noted however, that since the $Gd_3Cu_4Sn_4$ and $Gd_3Cu_4Ge_4$ compounds represent two of the more important outliers, and they are little affected by crystal field effects [86], the mystery will likely not be entirely resolved with these measurements.

7.3.5 Structural Properties Revisited

As mentioned above, this study focused on compounds within a range of temperatures for which the crystal structures are all the $Gd_3Cu_4Ge_4$-type and do not change. However, we have also mentioned that the $Tb_3Ag_4Sn_4$ system undergoes a magnetocrystalline transition [6]. Moreover, the $Tm_3Cu_4Sn_4$ system appears to exhibit the same monoclinic distortion from the $Gd_3Cu_4Ge_4$-type structure later discovered in $Tb_3Ag_4Sn_4$ [108], and recent data indicates that the compound transforms into the orthorhombic phase above room temperature [109]. The $Er_3Cu_4Sn_4$ system also shows evidence of adopting the monoclinic distorted structure at low temperature [109]. Studying the $Tb_3(Cu, Ag)_4Sn_4$ system will shed light on the nature and guiding forces of the transition, but a broader crystallographic survey is clearly needed.

Appendix A

Lattice Parameters of the $R_3T_4Sn_4$ Compounds

A.1 Lattice Parameters

The lattice parameters from Figure 2.9 are listed here in textual form in Table A.1 for the Cu compounds and Table A.2 for the Ag Compounds.

A.2 Interatomic Distances

Interatomic distances were not refined but rather calculated using the fitted crystal structure and the BLOKJE program [110].

Compound	a (Å)	b (Å)	c (Å)	
$Ce_3Cu_4Sn_4$	15.098(2)	7.022(1)	4.597(1)	[34]
$Pr_3Cu_4Sn_4$	15.004(7)	6.981(3)	4.567(2)	[8]
$Nd_3Cu_4Sn_4$	14.964(5)	6.976(2)	4.545(1)	[8]
$Sm_3Cu_4Sn_4$	14.856	6.968	4.520	[29]
$Gd_3Cu_4Sn_4$	14.743(4)	6.939(2)	4.4736(11)	[87]
$Tb_3Cu_4Sn_4$	14.6655(9)	6.9183(4)	4.4470(3)	[30]
$Dy_3Cu_4Sn_4$	14.612(1)	6.9110(5)	4.4312(3)	[30]
$Ho_3Cu_4Sn_4$	14.5744(8)	6.9052(3)	4.4187(2)	[30]
$Er_3Cu_4Sn_4$	14.5327(8)	6.8978(3)	4.4050(2)	[30]

Table A.1: Lattice parameters for the $R_3Cu_4Sn_4$ compounds.

Compound	a (Å)	b (Å)	c (Å)	
$Ce_3Ag_4Sn_4$	15.547(8)	7.362(3)	4.679(1)	[31]
$Pr_3Ag_4Sn_4$	15.451(4)	7.349(2)	4.654(1)	[8]
$Nd_3Ag_4Sn_4$	15.404(6)	7.339(3)	4.632(2)	[8]
$Sm_3Ag_4Sn_4$	15.300(3)	7.324(2)	4.597(1)	[82]
$Gd_3Ag_4Sn_4$	15.223(4)	7.309(2)	4.565(1)	[87]
$Tb_3Ag_4Sn_4$	15.1581(4)	7.3034(17)	4.5502(11)	[6]
$Dy_3Ag_4Sn_4$	15.1150(32)	7.2826(13)	4.5296(8)	[38]
$Ho_3Ag_4Sn_4$				
$Er_3Ag_4Sn_4$				

Table A.2: Lattice parameters for the $R_3Cu_4Sn_4$ compounds.

Compound	2d-2d (Å)	2d-4e (Å)	4e-2d (Å)	4e-4e1 (Å)	4e-4e2 (Å)
$Ce_3Cu_4Sn_4$	4.59700	4.01796	4.01796	3.90736	4.59700
$Pr_3Cu_4Sn_4$	4.56700	3.99413	3.99413	3.88304	4.56700
$Nd_3Cu_4Sn_4$	4.54500	3.98943	3.98943	3.87268	4.54500
$Sm_3Cu_4Sn_4$	4.52000	3.97916	3.97916	3.84473	4.52000
$Gd_3Cu_4Sn_4$	4.47360	3.95941	3.95941	3.81549	4.47360
$Tb_3Cu_4Sn_4$	4.44700	3.94548	3.94548	3.79530	4.44700
$Dy_3Cu_4Sn_4$	4.43120	3.93898	3.93898	3.78159	4.43120
$Ho_3Cu_4Sn_4$	4.41870	3.93408	3.93408	3.77175	4.41870
$Er_3Cu_4Sn_4$	4.40500	3.92829	3.92829	3.76114	4.40500

Table A.3: Calculated interatomic distances between the rare earth 2d site and its rare earth neighbours, and the rare earth 4e site and its rare earth neighbours for the $R_3Cu_4Sn_4$ compounds.

Compound	2d-2d (Å)	2d-4e (Å)	4e-2d (Å)	4e-4e1 (Å)	4e-4e2 (Å)
$Ce_3Ag_4Sn_4$	4.67900	4.19488	4.19488	4.02356	4.67900
$Pr_3Ag_4Sn_4$	4.65400	4.18323	4.18323	3.99872	4.65400
$Nd_3Ag_4Sn_4$	4.63200	4.17593	4.17593	3.98656	4.63200
$Sm_3Ag_4Sn_4$	4.59700	4.16292	4.16292	3.95964	4.59700
$Gd_3Ag_4Sn_4$	4.56500	4.15159	4.15159	3.93971	4.56500
$Tb_3Ag_4Sn_4$	4.55020	4.14514	4.14514	3.87486	4.55020
$Dy_3Ag_4Sn_4$	4.52960	4.13334	4.13334	3.91176	4.52960

Table A.4: Calculated interatomic distances between the rare earth 2d site and its rare earth neighbours, and the rare earth 4e site and its rare earth neighbours for the $R_3Ag_4Sn_4$ compounds.

Compound	4f-2d (Å)	4f-4e1 (above) (Å)	4f-4e2 (in the plane) (Å)	4h-2d (Å)	4h-4e (Å)
$Ce_3Cu_4Sn_4$	3.24456	3.28773	3.74079	3.15365	3.30563
$Pr_3Cu_4Sn_4$	3.22436	3.26678	3.71877	3.13409	3.28478
$Nd_3Cu_4Sn_4$	3.21576	3.25464	3.71525	3.12503	3.27368
$Sm_3Cu_4Sn_4$	3.19255	3.23387	3.70832	3.11426	3.25611
$Gd_3Cu_4Sn_4$	3.16827	3.20508	3.69139	3.09130	3.22909
$Tb_3Cu_4Sn_4$	3.15151	3.18710	3.67939	3.07729	3.21227
$Dy_3Cu_4Sn_4$	3.14012	3.17567	3.67441	3.07003	3.20216
$Ho_3Cu_4Sn_4$	3.13195	3.16708	3.67058	3.06428	3.19447
$Er_3Cu_4Sn_4$	3.12314	3.15772	3.66591	3.05777	3.18601

Table A.5: Calculated interatomic distances between the Sn-4f and its rare earth neighbours, and the Sn-4h site and its rare earth neighbours for $R_3Cu_4Sn_4$ compounds.

Compound	4f-2d (Å)	4f-4e1 (above) (Å)	4f-4e2 (in the plane) (Å)	4h-2d (Å)	4h-4e (Å)
$Ce_3Ag_4Sn_4$	3.34105	3.36644	3.91366	3.25548	3.39543
$Pr_3Ag_4Sn_4$	3.32042	3.34700	3.90476	3.24372	3.37842
$Nd_3Ag_4Sn_4$	3.31032	3.33410	3.89870	3.23369	3.36644
$Sm_3Ag_4Sn_4$	3.28797	3.31029	3.88864	3.21795	3.34522
$Gd_3Ag_4Sn_4$	3.27142	3.29056	3.87936	3.20330	3.32712
$Tb_3Ag_4Sn_4$	3.25745	3.27813	3.87486	3.19682	3.31661
$Dy_3Ag_4Sn_4$	3.24821	3.26617	3.86383	3.18500	3.30456

Table A.6: Calculated interatomic distances between the Sn-4f and its rare earth neighbours, and the Sn-4h site and its rare earth neighbours for $R_3Ag_4Sn_4$ compounds.

Appendix B

Temperature Dependence of Magnetization

The derivation of the expected temperature dependence of the magnetization in the Weiss model is done in two parts: first calculate the temperature dependence of the magnetization of a paramagnetic in an external field, then assume the field is not external but produced by neighbouring moments.

First we consider a quantum system with spin J which can take any integer or half-integer value between $\frac{1}{2}$ and ∞. The Hamiltonian for the system when a magnetic field B is applied is

$$H = -g_J \mu_B B \hat{J}_z \tag{B.1}$$

where g_J is the gyromagnetic factor, μ_B is the Bohr magneton, and $\hat{J}_z$ is the total spin operator. There are $2J+1$ energy levels each with an energy of $-g_J \mu_B B m_J$. At a temperature T, the partition function can be written as

$$Z = \sum_{m_J=-J}^{J} \exp\left[m_J g_J \mu_B B / k_B T\right] \tag{B.2}$$

writing $x = g_J \mu_B B / k_B T$, we can then compute the average m_J:

$$\langle m_J \rangle = \frac{\sum_{m_J=-J}^{J} m_J e^{m_J x}}{e^{m_J x}} = \frac{1}{Z}\frac{\partial Z}{\partial x}. \tag{B.3}$$

The magnetization with n spins is

$$M = ng_J\mu_B \langle m_J \rangle = \frac{ng_J\mu_B}{Z}\frac{\partial Z}{\partial B}\frac{\partial B}{\partial x} = nk_BT\frac{\partial lnZ}{\partial B} \tag{B.4}$$

The partition function is actually a geometric progression with initial term e^{-Jx} and common ratio e^x, and hence

$$Z = \frac{\sinh\left[(2J+1)\frac{x}{2}\right]}{\sinh\left[\frac{x}{2}\right]}. \tag{B.5}$$

Using the substitutions $y = Jx$ and $M_s = ng_J\mu_B J$, and calculating $\frac{\partial lnZ}{\partial B}$, we obtain

$$M = M_s\left[\frac{2J+1}{2J}\coth\left(\frac{2J+1}{2J}y\right) - \frac{1}{2J}\coth\frac{y}{2J}\right]. \tag{B.6}$$

The term in brackets is known as the Brillouin function.

Appendix C

Additional Peaks in AF Order

For simplicity, consider a monoatomic simple body centered cubic lattice ($a = b = c$). There are two atoms in the unit cell with coordinates $(0, 0, 0)$ and $\left(\frac{1}{2}, \frac{1}{2}, \frac{1}{2}\right)$. The structure factor for nuclear scattering is then

$$\begin{aligned}
\mathcal{F}_{nucl} &= \sum_n b_n \exp\left[2\pi i\left(h\frac{x_n}{a} + k\frac{y_n}{b} + l\frac{z_n}{c}\right)\right] && \text{(C.1)}\\
&= b\left(1 + \exp\left[2\pi i\left(h\frac{1}{2} + k\frac{1}{2} + l\frac{1}{2}\right)\right]\right) && \text{(C.2)}\\
&= b(1 + (-1)^{h+k+l}) && \text{(C.3)}\\
&= \begin{cases} 0 & if \quad h+k+l \quad uneven \\ 2b & if \quad h+k+l \quad even \end{cases} && \text{(C.4)}
\end{aligned}$$

The structure factor for magnetic scattering has the important difference of taking into account the direction of the moment. In our example, since the order is antiferromagnetic, the body centered moment is antiparallel to the corner moment, hence

$$\begin{aligned}
\mathcal{F}_{nucl} &= \sum_n pq_n \exp\left[2\pi i\left(h\frac{x_n}{a} + k\frac{y_n}{b} + l\frac{z_n}{c}\right)\right] && \text{(C.5)}\\
&= pq\left(1 - \exp\left[2\pi i\left(h\frac{1}{2} + k\frac{1}{2} + l\frac{1}{2}\right)\right]\right) && \text{(C.6)}\\
&= pq(1 - (-1)^{h+k+l}) && \text{(C.7)}\\
&= \begin{cases} 2pq & if \quad h+k+l \quad uneven \\ 0 & if \quad h+k+l \quad even \end{cases} && \text{(C.8)}
\end{aligned}$$

Thus, the magnetic peaks occur at positions not allowed by nuclear scattering.

Appendix D

The *Immm* space group

A crystal structure is a complete description of the location of all atoms in a crystal. The crystal structure is described by specifying three properties:

- the adopted space group
- the lattice parameters
- the location of a minimal subset of atomic locations, which, when combined with the space group, yield all atomic positions within the unit cell

First, the adopted space group is the set symmetry operations which leave the crystal unchanged. In the case of the $Gd_3Cu_4Ge_4$-type structure, the space group adopted is $Immm$ which implies that the crystallographic axes are orthogonal, and that the lattice parameters are not equal. The symmetry operations of the $Immm$ space group are: When the symmetry operations are applied to an atom with general coordinates x, y, z, 15 additional atoms are generated in the unit cell. The symmetry operations, with the corresponding generated site are listed in Table D.1. Often, it is considered sufficient (and perhaps more useful) to describe the generated site rather than the symmetry operation.

The coordinates are quoted as the fraction along each crystallographic axis. Hence, if the coordinates of an atom are $\frac{1}{2}, \frac{1}{2}, \frac{1}{2}$, this indicates that the actual atom location

Site Generated	Symmetry Operation
x,y,z	1
x,-y,-z	2 x,0,0
-x,y,-z	2 0,y,0
-x,-y,z	2 0,0,z
-x,-y,-z	-1 0,0,0
-x,y,z	m 0,y,z
x,-y,z	m x,0,z
x,y,-z	m x,y,0
x+1/2,y+1/2,z+1/2	t (1/2,1/2,1/2)
x+1/2,-y+1/2,-z+1/2	2 (1/2,0,0) x,1/4,1/4
-x+1/2,y+1/2,-z+1/2	2 (0,1/2,0) 1/4,y,1/4
-x+1/2,-y+1/2,z+1/2	2 (0,0,1/2) 1/4,1/4,z
-x+1/2,-y+1/2,-z+1/2	-1 1/4,1/4,1/4
-x+1/2,y+1/2,z+1/2	n (0,1/2,1/2) 1/4,y,z
x+1/2,-y+1/2,z+1/2	n (1/2,0,1/2) x,1/4,z
x+1/2,y+1/2,-z+1/2	n (1/2,1/2,0) x,y,1/4

Table D.1: Symmetry operations and generated sites for the *Immm* space group.

is $\frac{a}{2}, \frac{b}{2}, \frac{c}{2}$.

There are some coordinates that yield fewer than 16 distinct atoms. For example when the symmetry operations of the $Immm$ space group are applied to the $\frac{1}{2}, 0, \frac{1}{2}$ atom, only one other distinct atom is present, at $0, \frac{1}{2}, 0$, and all other symmetries either map the atom onto itself, or its one counterpart.

A complete list of these special positions can be computed, and arranged from highest to lowest symmetry. Each set is referred to as a crystallographic site, or Wyckoff position. The sites are labeled by a number followed by a letter. The number indicates how many atoms are in the unit cell (site multiplicity). The sites are then labeled alphabetically from highest to lowest symmetry. The number-letter combination is then used to identify each site.

Wyckoff Position	Atomic Positions		
16 o	x, y, z	$x, -y, -z$	$-x, y, -z$
	$-x, -y, z$	$-x, -y, -z$	$-x, y, z$
	$-x, y, z$	$x, -y, z$	$x, y, -z$
	$x+\frac{1}{2}, y+\frac{1}{2}, z+\frac{1}{2}$	$x+\frac{1}{2}, -y+\frac{1}{2}, -z+\frac{1}{2}$	$-x+\frac{1}{2}, y+\frac{1}{2}, -z+\frac{1}{2}$
	$-x+\frac{1}{2}, -y+\frac{1}{2}, z+\frac{1}{2}$	$-x+\frac{1}{2}, -y+\frac{1}{2}, -z+\frac{1}{2}$	$-x+\frac{1}{2}, y+\frac{1}{2}, z+\frac{1}{2}$
	$x+\frac{1}{2}, -y+\frac{1}{2}, z+\frac{1}{2}$	$x+\frac{1}{2}, y+\frac{1}{2}, -z+\frac{1}{2}$	
8n	$x, y, 0$	$x, -y, 0$	$-x, y, 0$
	$-x, -y, 0$	$x+\frac{1}{2}, y+\frac{1}{2}, \frac{1}{2}$	$x+\frac{1}{2}, -y+\frac{1}{2}, \frac{1}{2}$
	$-x+\frac{1}{2}, y+\frac{1}{2}, \frac{1}{2}$	$-x+\frac{1}{2}, -y+\frac{1}{2}, \frac{1}{2}$	
8m	$x, 0, z$	$x, 0, -z$	$-x, 0, -z$
	$-x, 0, z$	$x+\frac{1}{2}, \frac{1}{2}, z+\frac{1}{2}$	$x+\frac{1}{2}, \frac{1}{2}, -z+\frac{1}{2}$
	$-x+\frac{1}{2}, \frac{1}{2}, -z+\frac{1}{2}$	$-x+\frac{1}{2}, \frac{1}{2}, z+\frac{1}{2}$	
8l	$0, y, z$	$0, -y, -z$	$0, y, -z$
	$0, -y, z$	$\frac{1}{2}, y+\frac{1}{2}, z+\frac{1}{2}$	$\frac{1}{2}, -y+\frac{1}{2}, -z+\frac{1}{2}$
	$\frac{1}{2}, -y+\frac{1}{2}, z+\frac{1}{2}$		
8k	$\frac{1}{4}, \frac{1}{4}, \frac{1}{4}$	$\frac{1}{4}, \frac{3}{4}, \frac{3}{4}$	$\frac{3}{4}, \frac{1}{4}, \frac{3}{4}$
	$\frac{3}{4}, \frac{3}{4}, \frac{1}{4}$	$\frac{3}{4}, \frac{3}{4}, \frac{3}{4}$	$\frac{3}{4}, \frac{1}{4}, \frac{1}{4}$
	$\frac{1}{4}, \frac{3}{4}, \frac{1}{4}$	$\frac{1}{4}, \frac{1}{4}, \frac{3}{4}$	

Table D.2: Wyckoff positions for the $Immm$ space group.

Wyckoff Position	Atomic Positions		
4j	$\frac{1}{2}, 0, z$	$\frac{1}{2}, 0, -z$	$0, \frac{1}{2}, z + \frac{1}{2}$
	$0, \frac{1}{2}, -z + \frac{1}{2}$		
4i	$0, 0, z$	$0, 0, -z$	$\frac{1}{2}, \frac{1}{2}, z + \frac{1}{2}$
	$\frac{1}{2}, \frac{1}{2}, -z + \frac{1}{2}$		
4h	$0, y, \frac{1}{2}$	$0, -y, \frac{1}{2}$	$\frac{1}{2}, y + \frac{1}{2}, 0$
	$\frac{1}{2}, -y + \frac{1}{2}, 0$		
4g	$0, y, 0$	$0, -y, 0$	$\frac{1}{2}, y + \frac{1}{2}, \frac{1}{2}$
	$\frac{1}{2}, -y + \frac{1}{2}, \frac{1}{2}$		
4f	$x, \frac{1}{2}, 0$	$-x, \frac{1}{2}, 0$	$x + \frac{1}{2}, 0, \frac{1}{2}$
	$-x + \frac{1}{2}, 0, \frac{1}{2}$		
4e	$x, 0, 0$	$-x, 0, 0$	$x + \frac{1}{2}, \frac{1}{2}, \frac{1}{2}$
	$-x + \frac{1}{2}, \frac{1}{2}, \frac{1}{2}$		
2d	$\frac{1}{2}, 0, \frac{1}{2}$	$0, \frac{1}{2}, 0$	
2c	$\frac{1}{2}, \frac{1}{2}, 0$	$0, 0, \frac{1}{2}$	
2b	$0, \frac{1}{2}, \frac{1}{2}$	$\frac{1}{2}, 0, 0$	
2a	$0, 0, 0$	$\frac{1}{2}, \frac{1}{2}, \frac{1}{2}$	

Table D.3: Wyckoff positions for the *Immm* space group.

Bibliography

[1] C. Kittel, *Introduction To Solid State Physics*, 7th ed. (John Wiley & Sons, New York, 1996), p. 421.

[2] A. Szytuła and J. Leciejewicz, *Handbook of Crystal Structures and Magnetic Properties of Rare-Earth Intermetallics*, 1st ed. (CRC Press, Boca Raton, 1994), p. 68.

[3] S. Blundell, *Magnetism in Condensed Matter*, 1st ed. (Oxford University Press, London, 2001), p. 49.

[4] D. H. Ryan, J. M. Cadogan, R. Gagnon, and I. P. Swainson, J. Phys.: Cond. Matt. **16**, 3183 (2004).

[5] J. M. Cadogan, D. H. Ryan, and L. M. D. Cranswick, J. Phys.: Conf. Ser. **200**, 032009 (2010).

[6] L. K. Perry *et al.*, J. Appl. Phys. **99**, 08J502 (2006).

[7] A. Szytuła *et al.*, J. Alloys and Compds **367**, 224 (2004).

[8] E. Wawrzyńska *et al.*, J. Phys.: Cond. Matt. **16**, 7535 (2004).

[9] S. Blundell, *Magnetism in Condensed Matter*, 1st ed. (Oxford University Press, London, 2001), p. 74.

[10] M. A. Ruderman and C. Kittel, Phys. Rev. **96**, 99 (1954).

[11] T. Kasuya, Progress of Theoretical Physics **16**, 45 (1956).

[12] K. Yosida, Phys. Rev. **106**, 893 (1957).

[13] S. Blundell, *Magnetism in Condensed Matter*, 1st ed. (Oxford University Press, London, 2001), p. 79.

[14] E. Wawrzyńska and A. Szytuła, Materials Science (0137-1339) **24**, 543 (2006).

[15] C. Kittel, *Introduction To Solid State Physics*, 7th ed. (John Wiley & Sons, New York, 1996), p. 421.

[16] S. Blundell, *Magnetism in Condensed Matter*, 1st ed. (Oxford University Press, London, 2001), p. 24.

[17] S. Blundell, *Magnetism in Condensed Matter*, 1st ed. (Oxford University Press, London, 2001), p. 88.

[18] S. Blundell, *Magnetism in Condensed Matter*, 1st ed. (Oxford University Press, London, 2001), p. 92.

[19] A. Szytuła and J. Leciejewicz, *Handbook of Crystal Structures and Magnetic Properties of Rare-Earth Intermetallics*, 1st ed. (CRC Press, Boca Raton, 1994), p. 174.

[20] B. K. Cho, P. C. Canfield, and D. C. Johnston, Phys. Rev. B **52**, R3844 (1995).

[21] K. A. Gschneidner Jr., in *The Rare Earths*, 1st ed., edited by F. H. Spedding and A. H. Daane (Wiley & Sons, Inc., New York, 1961), p. 209.

[22] W. Rieger, Monatsch. Chem. **101**, 449 (1970).

[23] S. J. Joshua, *Symmetry Principles and Magnetic Symmetry in Solid State Physics*, 1st ed. (Adam Hilger, Bristol, 1991).

[24] R. Ballou and B. Ouladdiaf, in *Neutron Scattering from Magnetic Materials*, 1st ed., edited by T. Chatterji (Elsevier B.V., Amsterdam, 2006), p. 93.

[25] A. S. Wills, Physica B: Condensed Matter **276-278**, 680 (2000).

[26] L. D. Landau and E. M. Lifshitz, *Statistical Physics*, 3^{rd} ed. (Pergamon Press, London, 1980), p. 460.

[27] L. D. Landau and E. M. Lifshitz, *Statistical Physics*, 3^{rd} ed. (Pergamon Press, London, 1980).

[28] E. Wawrzyńska, J. Hernández-Velasco, B. Penc, and A. Szytuła, J. Phys.: Cond. Matt. **16**, 45 (2004).

[29] S. Singh, S. K. Dhar, P. Manfrinetti, and A. Palenzona, J. Magn. Magn. Mater. **250**, 190 (2002).

[30] E. Wawrzyńska *et al.*, J. Phys.: Cond. Matt. **15**, 5279 (2003).

[31] P. Boulet *et al.*, Intermetallics **7**, 931 (1999).

[32] A. Szytuła *et al.*, Intermetallics **14**, 702 (2006).

[33] D. Mazzone, P. Riani, M. Napoletano, and F. Canepa, J. Alloys and Compds **387**, 15 (2005).

[34] S. Singh, S. K. Dhar, P. Manfrinetti, and A. Palenzona, Journal of Alloys and Compounds **298**, 68 (2000).

[35] O. Zaharko, L. Keller, and C. Ritter, J. Magn. Magn. Mater. **253**, 130 (2002).

[36] Ł. Gondek *et al.*, Intermetallics **15**, 583 (2007).

[37] A. Szytuła *et al.*, J. Alloys and Compds **367**, 224 (2004).

[38] L. K. Perry *et al.*, J. Phys.: Cond. Matt. **18**, 5783 (2006).

[39] E. Wawrzyńska *et al.*, J. Magn. Magn. Mater. **264**, 192 (2003).

[40] S. K. Dhar *et al.*, Physica B: Condensed Matter **312-313**, 846 (2002).

[41] B. Penc *et al.*, Intermetallics **15**, 1489 (2007).

[42] Andrzej Szytuła *et al.*, phys. stat. sol. (b) **243**, 299 (2006).

[43] H. Oesterreicher, phys. stat. sol. (a) **39**, K75 (1977).

[44] T. C. Gibb and N. N. Greenwood, *Mössbauer Spectroscopy*, 1st ed. (Chapman and Hall Ltd, London, 1971), p. 9.

[45] T. C. Gibb and N. N. Greenwood, *Mössbauer Spectroscopy*, 1st ed. (Chapman and Hall Ltd, London, 1971), p. 10.

[46] T. C. Gibb and N. N. Greenwood, *Mössbauer Spectroscopy*, 1st ed. (Chapman and Hall Ltd, London, 1971), p. 11.

[47] W. Henning, G. Baehre, and P. Kienle, Physics Letters B **31**, 203 (1970).

[48] T. C. Gibb and N. N. Greenwood, *Mössbauer Spectroscopy*, 1st ed. (Chapman and Hall Ltd, London, 1971), p. 18.

[49] T. C. Gibb and N. N. Greenwood, *Mössbauer Spectroscopy*, 1st ed. (Chapman and Hall Ltd, London, 1971), p. 46.

[50] T. C. Gibb and N. N. Greenwood, *Mössbauer Spectroscopy*, 1st ed. (Chapman and Hall Ltd, London, 1971), p. 60.

[51] W. Kündig, Nucl. Instr. and Meth. **48**, 219 (1967).

[52] M. Blume and J. A. Tjon, Phys. Rev. **165**, 446 (1968).

[53] D. H. Ryan, J. M. Cadogan, and A. V. Edge, J. Phys.: Condens. Matter **16**, 6129 (2004).

[54] T. C. Gibb and N. N. Greenwood, *Mössbauer Spectroscopy*, 1st ed. (Chapman and Hall Ltd, London, 1971), p. 608.

[55] J. P. Biscar, W. Kündig, H. Bömmel, and R. S. Hargrove, Nucl. Instr. and Meth. **75**, 165 (1969).

[56] P. Raghavan, Atomic Data and Nuclear Data Tables **42**, 189 (1989).

[57] J. M. Cadogan, D. H. Ryan, and J. D. Cashion, Journal of Physics: Condensed Matter **19**, 216204 (2007).

[58] J. D. Cashion, D. B. Prowse, and A. Vas, J. Phys. C: Solid State Phys. **6**, 2611 (1973).

[59] T. C. Gibb and N. N. Greenwood, *Mössbauer Spectroscopy*, 1st ed. (Chapman and Hall Ltd, London, 1971), p. 372.

[60] T. Mazet, J. Tobola, G. Venturini, and B. Malaman, Phys. Rev. B **65**, 104406 (2002).

[61] L. K. Perry, D. H. Ryan, and G. Venturini, Phys. Rev. B **75**, 144417 (2007).

[62] G. Le Cäer, B. Malaman, G. Venturini, and I. B. Kim, Phys. Rev. B **26**, 5085 (1982).

[63] T. Chatterji, in *Neutron Scattering from Magnetic Materials*, 1st ed., edited by T. Chatterji (Elsevier B.V., Amsterdam, 2006), p. 3.

[64] G. E. Bacon, *Neutron Diffraction*, 3rd ed. (Oxford University Press, London, 1975), p. 35.

[65] G. E. Bacon, *Neutron Diffraction*, 3rd ed. (Oxford University Press, London, 1975), p. 36.

[66] V. Sears, Neutron News **3**, 26 (1992).

[67] G. E. Bacon, *Neutron Diffraction*, 3rd ed. (Oxford University Press, London, 1975), p. 206.

[68] G. E. Bacon, *Neutron Diffraction*, 3rd ed. (Oxford University Press, London, 1975), p. 205.

[69] G. E. Bacon, *Neutron Diffraction*, 3rd ed. (Oxford University Press, London, 1975), p. 203.

[70] G. E. Bacon, *Neutron Diffraction*, 3rd ed. (Oxford University Press, London, 1975), p. 225.

[71] B. M. Powell, Neutron News **1**, 16 (1990).

[72] G. E. Bacon, *Neutron Diffraction*, 3rd ed. (Oxford University Press, London, 1975), p. 130.

[73] J. W. Cable and E. O. Wollan, Phys. Rev. **165**, 733 (1968).

[74] Y. Ishikawa, N. Watanabe, K. Tajima, and H. Sekine, Physics Letters A **48**, 159 (1974).

[75] D. H. Ryan and L. M. D. Cranswick, Journal of Applied Crystallography **41**, 198 (2008).

[76] A. C. Larson and R. B. von Dreele, Technical report, Los Alamos National Laboratory (unpublished).

[77] B. H. Toby, J. Appl. Crystallogr. **34**, 210 (2001).

[78] C. J. Voyer, D. H. Ryan, and J. M. Cadogan, J. Appl. Phys. **105**, 07D508 (2009).

[79] D. H. Ryan *et al.*, Modern Physics Letters B **24**, 1 (2010).

[80] E. Wawrzynska, J. Hernndez-Velasco, B. Penc, and A. Szytuła, Physica B: Condensed Matter **350**, E127 (2004).

[81] A. Szytuła *et al.*, Physica B: Condensed Matter **327**, 167 (2003).

[82] C. J. Voyer *et al.*, J. Phys.: Cond. Matt. **19**, 436205 (2007).

[83] H. W. de Wijn, A. M. V. Diepen, and K. H. J. Buschow, phys. stat. sol. (b) **76**, 11 (1976).

[84] A. Szytuła and J. Leciejewicz, *Handbook of Crystal Structures and Magnetic Properties of Rare-Earth Intermetallics*, 1st ed. (CRC Press, Boca Raton, 1994), p. 69.

[85] H. Adachi, H. Ino, and H. Miwa, Phys. Rev. B **56**, 349 (1997).

[86] D. R. Noakes and G. K. Shenoy, Physics Letters A **91**, 35 (1982).

[87] C. J. Voyer, D. H. Ryan, M. Napoletano, and P. Riani, J. Phys.: Cond. Matt. **19**, 156209 (2007).

[88] J. M. Cadogan *et al.*, Journal of Physics: Condensed Matter **21**, 124201 (2009).

[89] D. H. Ryan *et al.*, Phys. Rev. Lett. **90**, 117202 (2003).

[90] K. Łatka, A. W. Pacyna, R. Pöttgen, and F. M. Schappacher, Acta Physica Polonica A **114**, 1501 (2008).

[91] C. P. Sebastian, S. Rayaprol, and R. Pttgen, Solid State Communications **140**, 276 (2006).

[92] K. Łatka *et al.*, Journal of Alloys and Compounds **390**, 9 (2005).

[93] K. Łatka *et al.*, Journal of Alloys and Compounds **385**, 64 (2004).

[94] K. Łatka, R. Kmiec, and J. Gurgul, Journal of Alloys and Compounds **319**, 43 (2001).

[95] K. Łatka, W. Chajec, and R. Kmiec, Journal of Alloys and Compounds **383**, 269 (2004).

[96] D. Bialic, R. Kruk, R. Kmiec, and K. Tomala, Journal of Alloys and Compounds **257**, 49 (1997).

[97] N. N. Delyagin and V. I. Krylov, Solid State Communications **126**, 401 (2003).

[98] L. K. Perry, D. H. Ryan, and G. Venturini, Journal of Applied Physics **101**, 09K504 (2007).

[99] L. Perry, D. Ryan, and G. Venturini, Hyperfine Interactions **170**, 105 (2006), 10.1007/s10751-006-9468-1.

[100] J. P. Sanchez *et al.*, Journal of Physics C: Solid State Physics **9**, 2207 (1976).

[101] R. Gladyhevskii, O. Sologub, and E. Parthé, Journal of Alloys and Compounds **176**, 329 (1991).

[102] B. Y. Kotur and M. Sikirica, Acta Crystallographica Section B **38**, 917 (1982).

[103] D. Niepmann, Y. M. Prots', R. Pttgen, and W. Jeitschko, Journal of Solid State Chemistry **154**, 329 (2000).

[104] G. Bocelli, O. Sologub, and P. Salamakha, Journal of Alloys and Compounds **360**, L3 (2003).

[105] A Szytuła, B. Penc, and A. Zarzycki, Journal of Physics: Conference Series **200**, 032072 (2010).

[106] L. Gondek *et al.*, Journal of Physics: Condensed Matter **20**, 295205 (2008).

[107] A. Szytuła *et al.*, Journal of Magnetism and Magnetic Materials **272-276**, 618 (2004), proceedings of the International Conference on Magnetism (ICM 2003).

[108] F. Thirion, J. Steinmetz, and B. Malaman, Materials Research Bulletin **18**, 1537 (1983).

[109] J. M. Cadogan, private communication .

[110] L. Gelato, Journal of Applied Crystallography **14**, 151 (1981).